



HAL
open science

Mn₄N thin films for spintronics applications based on current-induced domain wall motion

Toshiki Gushi

► **To cite this version:**

Toshiki Gushi. Mn₄N thin films for spintronics applications based on current-induced domain wall motion. Materials Science [cond-mat.mtrl-sci]. Université Grenoble Alpes; Université de Tsukuba, 2019. English. NNT: 2019GREAY007 . tel-02280481

HAL Id: tel-02280481

<https://theses.hal.science/tel-02280481>

Submitted on 6 Sep 2019

HAL is a multi-disciplinary open access archive for the deposit and dissemination of scientific research documents, whether they are published or not. The documents may come from teaching and research institutions in France or abroad, or from public or private research centers.

L'archive ouverte pluridisciplinaire **HAL**, est destinée au dépôt et à la diffusion de documents scientifiques de niveau recherche, publiés ou non, émanant des établissements d'enseignement et de recherche français ou étrangers, des laboratoires publics ou privés.

THÈSE

Pour obtenir le grade de
**DOCTEUR DE LA COMMUNAUTE UNIVERSITE
GRENOBLE ALPES**
préparée dans le cadre d'une cotutelle entre
*l'Université Grenoble Alpes et
the University of Tsukuba*

Spécialité : Physique
Arrêté ministériel : le 6 janvier 2005 – 25 mai 2016

Présentée par
Toshiki GUSHI

Thèse codirigée par **Takashi SUEMASU** et **Olivier FRUCHART**
Et co-encadrée par **Jean-Philippe ATTANÉ** et **Laurent VILA**

préparée au sein des laboratoires Spintec, CEA-Grenoble et
Environmentally Friendly Materials in the Next Generations,
University of Tsukuba
dans les Écoles Doctorales de Physique et Pure and Applied
Sciences

dans les Écoles Doctorales ...

Mn₄N thin films for spintronics applications based on current-induced domain wall motion

Thèse soutenue publiquement le **14 février 2019**,
devant le jury composé de :

Japan, Yoshichika OTANI
Professeur, University of Tokyo & Riken, Rapporteur

France, André THIAVILLE
Directeur de Recherche, Laboratoire de Physique des Solides, Université Paris
Sud, Rapporteur

Japan, Hideto YANAGIHARA
Professeur, University of Tsukuba, Examineur

Japan, Yuzo OHNO
Professeur, University of Tsukuba, Examineur

Japan, Seiji MITANI
Professeur, University of Tsukuba & National Institute for Material Science,
Examineur

France, Agnès BARTHELEMY
Professeur, Unité Mixte de physique, CNRS/Thales, Examineur

France, Nora DEMPSEY (President of the Jury)
Directeur de Recherche, Institut Néel / CNRS, Examineur



Outline

Extended Abstract.....	1
Introduction.....	1
Magnetic domain structure in Mn ₄ N thin films	1
Spin transfer torque measurement in Mn ₄ N microstrips.....	3
Tailoring the magnetic properties by Ni-substitution into Mn ₄ N	4
Summary.....	5
Chapter 1 Introduction.....	7
Chapter 2 State of the art	10
2.1. History of spintronics.....	10
2.2. Magnetic domain wall (DW) and dynamics	11
2.2.1. Energies in ferromagnets	11
2.2.2. Formation of magnetic domains	13
2.2.3. Magnetization dynamics	13
2.2.4. Spin-transfer torque (STT).....	14
2.2.5. Current-induced domain wall motion	15
2.2.6. Spin-transfer torque in ferrimagnetic materials	17
2.3. Experimental reports of CIDWM	20
2.4. Anti-perovskite 3d-metal nitrides	22
2.4.1. Mn ₄ N.....	22
2.4.2. Substrates.....	24
Chapter 3 Magnetic domain structure in Mn ₄ N thin films.....	26
3.1. Growth and structure	26
3.1.1. MBE growth of Mn ₄ N thin films	26
3.1.2. Crystallinity of the Mn ₄ N film.....	28
3.2. Magnetic and electric properties.....	31
3.2.1. Fundamental magnetic properties	31
3.2.2. Magneto-transport properties.....	34
3.3. Magnetic domain structure	38
3.3.1. Magneto-optical Kerr effect (MOKE) imaging	38
3.3.2. Magnetic force microscopy (MFM).....	39
3.3.3. Equilibrium domain size	40
3.4. The influence of substrates	41
3.5. Summary.....	42
Chapter 4 Spin-transfer torque using direct current.....	43
4.1. Nanofabrication process	43
4.1.1. Electron-beam (EB) lithography.....	43

Outline

4.1.2. Ion beam etching.....	43
4.1.3. Detailed steps for nanofabrication	44
4.2. Equivalency between current and magnetic field	45
4.3. Pinning of the DW on the notch	48
4.4. CIDWM without external field assistance	49
4.5. Summary	50
Chapter 5 Evaluation of DW speed and spin-transfer efficiency.....	51
5.1. Device fabrication.....	51
5.2. Speed of DWs driven by current pulses.....	54
5.2.1. DW speed measurement	54
5.2.2. Current dependence of DW speed	55
5.2.3. Field driven Domain wall motion	57
5.3. Origin of the high DW mobility in Mn ₄ N.....	58
5.4. Estimation of the spin-polarization.....	59
5.5. Influence of the non-adiabatic torque and of the damping parameter on CIDWM	60
5.6. Damping and non-adiabatic torque: the particular case for which $\alpha = \beta$	61
5.7. Summary	62
Chapter 6 Mn substitution by Ni in Mn ₄ N thin films.....	64
6.1. Growth and crystallinities	64
6.1.1. MBE growth of Mn _{4-x} Ni _x N.....	64
6.1.2. Crystalline quality of the Mn _{4-x} Ni _x N films	65
6.2. Magnetic and electric properties	65
6.2.1. VSM characterization	65
6.2.2. Magneto-transport properties.....	67
6.2.3. MOKE observation of the domain structure and sign of the MOKE signal	70
6.3. Temperature dependence of the magnetic and magneto-transport properties	71
6.3.1. Magnetization at low temperature	71
6.3.2. Magneto-transport properties at low temperature.....	74
6.4. Hypothesis of compensation by Ni atoms.....	76
Chapter 7 Total summary and prospects.....	78
Acknowledgement	80
Special thanks	82
Appendix	83
Cross-sectional TEM observation of Mn ₄ N/STO interface	83
Voltage control of magnetic anisotropy.....	84
List of publications	86
Reference	90

Extended Abstract

Introduction

In the last 20 years, current-induced domain wall motion (CIDWM) has been studied theoretically and experimentally, mostly with the aim of discovering new ways to develop spintronic devices based on domain wall (DW) motion, such as the racetrack memory and the DW-motion MRAM. During one decade, the spin-transfer torque (STT), resulting from the transfer of angular momentum carried by the spin polarized current within the magnetic material, was the only physical effect known to allow current-induced domain wall motion. The discovery of spin-orbit torques (SOT) in multilayer systems brought more versatility and greater efficiency to CIDWM, and largely shifted the focus of the community towards spin orbitronics.

Simulations and experiments show that in perpendicularly magnetized ferrimagnets the critical current densities required to induce domain-wall motion by STT or by SOT is greatly reduced, because of the low value of the magnetization. Minimizing the operating currents allows obtaining a lower energy consumption. Thus, the combination of both STT/SOT and ferrimagnets is a very attracting pathway for creating spintronic devices based on DW motion or on nanomagnet switching.

Until now, most perpendicular ferrimagnetic materials used for DW motion experiments are rare-earth based, with a risk about material criticality in the context of the rising demand for these elements. Anti-perovskite-type nitrides with 3d transition metals are rare-earth free and could thus be interesting candidates for the replacement of the rare-earth based systems. Among them, Mn_4N thin films have a high Néel temperature T_N of 745 K, a small spontaneous magnetization M_S (100 kA/m) due to ferrimagnetic ordering between two inequivalent sites, and a strong perpendicular magnetic anisotropy (PMA), with $\mu_0 H_K$ values over 2.5 T. For the last five years, Mn_4N thin films with PMA have been successfully grown on MgO and SrTiO_3 (STO) substrates by sputtering, molecular beam epitaxy (MBE), and pulse laser deposition. In this work, we have been interested in evaluating the magnetic and magneto-transport properties of Mn_4N grown on STO by MBE, for the application to spintronic devices based on CIDWM. Specifically, the fundamental properties of blanket layers, such as the magnetic anisotropy, the anomalous Hall effect, and the magnetic domain structures are studied in chapter 3, the magnitude and efficiency of STTs in Mn_4N microstrips are detailed in chapters 4 and 5, and the modification of the magnetic properties by substitution of Mn atoms by Ni is presented in chapter 6.

Magnetic domain structure in Mn_4N thin films

We have studied 10-nm-thick Mn_4N epitaxial thin films grown on MgO(001) and STO(001) substrates by MBE. Using structural characterizations, magneto-transport measurements, vibrating sample magnetometry (VSM) and magnetic imaging techniques, we studied the influence of the substrate on the magnetic properties.

SiO_2 (3 nm)/ Mn_4N (10 nm) layers have been deposited on MgO(001) and STO(001) substrates at 450 °C, using a MBE system. The crystalline quality of the Mn_4N layer has been characterized by reflection high-energy electron diffraction and X-ray diffraction, resulting in features common to both systems: streaky RHEED patterns, and XRD peaks of *c*-axis-oriented Mn_4N . The full widths at half maximum (FWHM) of ω -scan rocking curves are however very different, indicating that Mn_4N films are much better textured when deposited on STO.

From the hysteresis curves measured by VSM, we found the M_S of $\text{Mn}_4\text{N}/\text{MgO}$ and $\text{Mn}_4\text{N}/\text{STO}$ to be

118 and 105 kA/m, respectively, in agreement with previous reports. The resistivity is 187 $\mu\Omega\cdot\text{cm}$ for the $\text{Mn}_4\text{N}/\text{MgO}$ sample, and 181 $\mu\Omega\cdot\text{cm}$ for the $\text{Mn}_4\text{N}/\text{STO}$ sample. The Anomalous Hall Effect (AHE) has been measured by the Van der Pauw method for Mn_4N blanket layers at room temperature. The AHE angle ρ_{xy}/ρ_{xx} is high (-2%), in line with previous reports on Mn_4N .

While the $\text{Mn}_4\text{N}/\text{MgO}$ sample shows a smooth hysteresis loop, the magnetization of the $\text{Mn}_4\text{N}/\text{STO}$ sample switches very sharply, with a full remanence at zero field. Despite these differences, it is striking that the transport of the two systems are very similar, indicating that the materials are intrinsically alike. The structural characterizations suggest however that the structural disorders due to the crystalline defects are different, and thus that the increased disorder is responsible for the higher coercivity and slanted loop of $\text{Mn}_4\text{N}/\text{MgO}$ samples. In-plane hysteresis curves obtained by in-plane AHE measurement shows that, while the magnetization of Mn_4N on MgO rises with relatively small fields, indicating a weak anisotropy, that on STO linearly increases much smoothly with the field, the anisotropy field being $H_K = 4.5$ T. The magnetic anisotropy energy K_u , calculated from the integration of the area enclosed between the in-plane and out-of-plane magnetization curves, and taking into account the demagnetization energy, is 0.12 MJ/m³ for MgO and 0.20 MJ/m³ for STO, respectively.

The theoretical equilibrium domain size results from the balance between the demagnetization energy and the DW energy $\sqrt{AK_u}$, where A is an exchange stiffness. A theoretical calculation assuming a periodic stripe domain structure concluded that the equilibrium domain size for this Mn_4N film is theoretically 1.3×10^{10} m. This indicates that in this system the demagnetizing energy is negligible with respect to the DW energy, because of the small M_S and high K_u , and that in practice the domain size and shape will be rather determined by DW pinning on extrinsic defects.

After a partial reversal process, done by applying an external field close to coercive field, to reverse half of the magnetization, the magnetic domains have been observed by magnetic force microscopy (MFM) for $\text{Mn}_4\text{N}/\text{MgO}$ and by Kerr microscopy for $\text{Mn}_4\text{N}/\text{STO}$. The sample on MgO shows sub- μm domains, much smaller than what would be expected at equilibrium. In contrast, the sample on STO has millimeter-sized domains, a value never reported in single crystalline perpendicularly magnetized thin films (to our knowledge). MOKE images show the presence of very few nucleation centers, which means that the magnetization switching occurs by a nucleation followed by an easy propagation. This observation is consistent with the fact that the hysteresis loop is squared.

The differences between the two systems are striking, concerning both their hysteresis loops, and their domain shapes and sizes. The XRD data and the magnetic properties suggest that these differences arise from the crystalline quality of the samples, which is higher for the $\text{Mn}_4\text{N}/\text{STO}$ samples. The physical origin could arise from the difference in the strain relaxation process: there is a large lattice misfit $f = (a_{\text{film}} - a_{\text{sub}})/a_{\text{sub}}$ at the $\text{Mn}_4\text{N}/\text{MgO}$ interface (-7.6%), whereas the misfit at the $\text{Mn}_4\text{N}/\text{STO}$ interface is only -0.4% . While the existence of misfit dislocations at the $\text{Mn}_4\text{N}/\text{MgO}$ interface has already been observed by transmission electron microscopy, other strain-relaxation process through the creation of dislocations or micro-grain boundaries are also expected to play a major role in the magnetic behavior. This underlines that the selection of a well-matching substrate is crucial to improve the magnetic properties of Mn_4N layers, and notably its suitability for current-induced DW propagation.

Spin transfer torque measurement in Mn₄N microstrips

The magnitude of the STT is inversely proportional to the magnetization. Thus, Mn₄N thin films should have a large STT efficiency, thanks to their small M_S (~100 kA/m). However, there are only few reports about magneto-transport properties in Mn₄N, and no study of spin-transfer torques. Therefore, we aim to give light on the potential of Mn₄N thin films by evaluating the efficiency of the STT, for instance by measuring threshold currents or DW velocities. We have used current pulses coupled to MOKE microscopy observations, and we demonstrate the potential of Mn₄N as a candidate for CIDWM application by showing that standard STT can lead to very high DW speeds in this material.

A Mn₄N film grown on STO has been processed to create the 1 or 2- μ m-wide multi-microstrips device. This device consists of 2 electric contacts connecting 20 strips in parallel. The current flowing through the strips can possibly induce DW motion. Under perpendicularly applied fields, the reversed domains nucleate firstly in the pad, probably because nucleation is extrinsic, and because the odds of finding a defect with a low nucleation field are bigger in a large area. Both electric contacts are covered by Ti/Au/Ti electrodes, obtained using a lift-off process. This allows wire-bonding the sample and applying the equal voltage to all the strips, and thus injecting the same current density.

The multi-strip device has been connected to the pulse generator and a 50- Ω resistor in series, in order to monitor the shape of the pulse using an oscilloscope. A coil under the sample stage allows applying magnetic field pulses. The magnetic state of the device is being monitored by Kerr microscopy in differential mode. The magnitude and length of field pulses have been optimized in order to stop DWs in the middle of the strips. The direction of DW motion is opposite to the current, indicating a positive spin-polarization of the conduction electrons in Mn₄N. The displacement of the DWs Δx is obtained by measuring the full width at half maximum of the MOKE profile along the wire and by varying the pulse width.

The threshold current density for 1-ns-long pulse is 3.0×10^{11} A/m². Above 8.5×10^{11} A/m² in 1- μ m-wide strips, the trend of the v_{DW}/j curve becomes linear. In the studied range of current densities, the DW reached a maximal velocity of 900 m/s, for a current density of 1.3×10^{12} A/m² in both 1- μ m and 2- μ m-wide strips. This value is the highest in all materials and structures whose DW was driven by only pure STT, and the second highest value when looking at SOT-driven systems. Nonetheless here at room temperature.

Another figure of merit of the STT efficiency is the DW mobility $\eta = \frac{dv_{\text{DW}}}{dj}$, that can be derived from the v_{DW}/j curve, and is equal to 7.1×10^{-10} m³/C. This mobility is also the highest value in all STT-driven systems, and it is superior to most SOT-driven records. Using the material parameters measured experimentally for the Mn₄N film ($M_S = 71$ kA/m, $K_u = 0.16$ MJ/m³), and assuming $A = 10$ pJ/m and $P = 0.7$, the critical current density in our samples is expected to be $j_c \sim 1 \times 10^{10}$ A/m². This is much lower than that of a typical permalloy strip with in-plane magnetization ($j_c \sim 3 \times 10^{12}$ A/m²), for which the non-adiabatic torque has been invoked to explain the DW motion experimentally observed below j_c .

When $j \gg j_c$, the DW moves in the precessional regime at a velocity given by, $\mathbf{v}_{\text{DW}} \approx \frac{1}{1+\alpha^2} |\mathbf{u}|$, where $\mathbf{u} = \frac{g\mu_B}{2eM_S} P\mathbf{j}$ is the spin-drift velocity, parallel to the electrons flow. Experimentally, a linear regime indeed appears in the $v_{\text{DW}} - j$ curve above the steady regime. The conjunction of the small M_S and high P is responsible

for the observed large DW velocities, as the mobility dv_{DW}/dj is expected to be proportional to P/M_S .

To confirm this interpretation, micromagnetic simulations have been performed. The results of the micromagnetic simulations have given an overall agreement with the 1D model and the experimental results in the high current densities regime. On the other hand, the trend of the DW speed in the low current regime is completely different from the experiment showing a relatively large critical current density of 3.0×10^{11} A/m². This is due to the pinning of the DWs by defects in the actual devices while the system is supposed to be perfect without any disorder in the simulation. If the sample were perfect, we could move DW starting at J_c .

The DW velocity v_{DW} is expected to vary linearly with the current density j , which is proportional to the spin-drift velocity u . The spin polarization of Mn₄N can be derived from the data in the high current regime, which provide the DW mobility η . Indeed, the spin polarization P is given in the 1D model by, $P = \eta \frac{2eM_S}{g\mu_B} \sim 0.75$, where $e = 1.60 \times 10^{-19}$ C, $g = 2.0$, $\mu_B = 9.27 \times 10^{-24}$ Am², $M_S = 66.1$ kA/m (measured before nanofabrication) and $\eta = 7.1 \times 10^{-10}$ C/m³. Note that such a high spin polarization could be of interest not only to develop CIDWM devices, but also for magneto-resistive applications such as GMR or TMR devices.

Tailoring the magnetic properties by Ni-substitution into Mn₄N

Rare-earth based ferrimagnetic materials with PMA such as TbFeCo and GdFeCo are attracting attention because their magnetization is controllable by tuning the composition. Especially, at the angular momentum compensation point, an extremely fast DW motion driven by SOTs and magnetic fields has been reported.

In this context, Mn₄N is also appealing. The ferrimagnetism of Mn₄N is due to the existence of a crystallographic sublattice for Mn, *i.e.* of large magnetic moment at the corner sites (I-site: μ_I) and of small moment at the face-centered sites (II-site: μ_{II}), in contrast to rare-earth ferrimagnets where the moment of rare-earth atoms is antiparallel to that of Fe and Co. Therefore, Mn₄N can only be compensated by tuning the composition through substitution. For the past 5 years, we have been investigating some Mn₄N alloys in which Mn was substituted by 3d metals such as Co, Fe and Ni to tune their magnetic properties. This can result in the reduction of M_S in Mn_{4-x}Co_xN and Mn_{4-x}Ni_xN, while keeping a perpendicular magnetization. Here, we focus on Mn_{4-x}Ni_xN films grown on STO, evaluating their magnetic and magneto-transport properties, and showing that it is possible to obtain the compensation by Ni substitution.

Mn_{4-x}Ni_xN thin films were grown on MgO and STO substrates by molecular beam epitaxy. The nominal content of Ni, x , has been determined from the deposition rates -measured before the growth- to be 0, 0.1, 0.25, and 0.5. Magnetization hysteresis loops have been measured by VSM, showing that Ni introduction induces a reduction of M_S while conserving the perpendicular magnetization. The samples grown on STO possess a larger M_S and a more important PMA, resulting in a sharp magnetization switching. We attributed this variation of M_S and of the hysteresis loops to the difference of the crystalline qualities due to the lattice mismatch, like it has been observed for pure Mn₄N films. The AHE loops of Mn_{4-x}Ni_xN films possess different of remanences and magnetization reversal sharpness depending on whether they are deposited on MgO or STO.

The sign of anomalous Hall coefficients is reversed between $x = 0.1$ and 0.25. This sudden reversal of sign, whereas the amplitude remains high in absolute value, could be due to the crossing of the ferrimagnetic

compensation point, because the direction of the magnetic moment of 3d atoms in each sublattice changes with respect to the magnetic field. Therefore, this sign reversal is commonly used to confirm the compensation in rare-earth ferrimagnets.

We thus performed several measurements to evidence this crossing of the compensation point. The Kerr contrast has been characterized and the inversion of the Kerr contrast from $x = 0.1$ to $x = 0.25$ might also be the evidence of compensation in $\text{Mn}_{3.75}\text{Ni}_{0.25}\text{N}$.

Magnetization measurements at low temperatures have also been performed. The measurement has been performed under a magnetic field of 0.1 T. The M - T trends of $x = 0$ and 0.1 samples are the same, *i.e.*, M_S increases at low temperatures, while it decreases for $x = 0.25$. Such a behavior has already been reported more than a half century ago, in $\text{Mn}_{4-x}(\text{In or Sn})_x\text{N}$ systems and attributed to the ferrimagnetic compensation.

On the assumption that the magnetic moment at the I-site (μ_I) rises more sharply at low temperatures than that at the II-site (μ_{II}), there is a state below compensation where μ_I dominates the total magnetization ($\mu_I > \mu_{II}$), and M_S monotonically increases as the temperature decreases. On the other hand, above the compensation composition, μ_{II} dominates the total magnetization, and the M - T curve is bended to a complex shape, with a reduction at low temperatures. Thus, the shape of the M - T curve of $\text{Mn}_{3.75}\text{Ni}_{0.25}\text{N}$ reflects the fact that the compensation composition has been crossed.

In this thesis, we propose a model assuming a mechanism of compensation in $\text{Mn}_{4-x}\text{Ni}_x\text{N}$, where Mn atoms at I-site are substituted by Ni atoms with smaller magnetic moment. As a result, μ_{Ni} has been estimated to be $-0.7\mu_B$ by the fitting of composition dependence of magnetization. Such a negative value means that the magnetic moment of Ni atoms is parallel to that of Mn atoms at II-sites, and anti-parallel to those at I-sites. The compensation composition x_c has also been estimated as around $x = 0.18$.

Summary

The magnetic and magneto-transport properties of Mn_4N thin films have been evaluated. A dramatic improvement of these properties is obtained by replacing conventional MgO substrates by STO substrates. The $\text{Mn}_4\text{N}/\text{STO}$ system exhibits astonishing properties: a millimeter-sized domain structure, full remanence, and a sharp magnetization switching corresponding to the nucleation of reversed domain from scarce nucleation centers and a smooth DW propagation.

The efficiency of the STT in Mn_4N thin films has been evaluated by measuring the speed of DWs driven by current pulses. The DW velocity reaches record values of 900 m/s for a current density of 1.3×10^{12} A/m², moreover at room temperature. This value is the highest in all STT-driven systems, and is comparable to the highest speeds obtained using SOTs. The DW mobility η derived from the slope of the $v_{\text{DW}}-j$ curve is also very large (7.1×10^{-10} m³/C), the highest in all STT-based systems too. Fits of our data using a 1D analytical model allows extracting a spin polarization of the conduction electrons of 0.7, suggesting that Mn_4N could be suitable to obtain large magnetoresistances.

The reduction of M_S by Ni-introduction has been demonstrated, while keeping the perpendicular magnetization and the full remanence, indicating the possibility of reaching the compensation point. This possibility is evidenced by the reversal of the anomalous Hall coefficient and of the Kerr contrast, and by the

Extended Abstract

temperature dependence of magnetization. The composition of the compensation point x_c has been estimated to be around 0.18. We suggest that the compensation can be understood using a simple model.

The amazing results on CIDWM have been achieved without using any rare earth element, without complex stack structures, external assistance such as magnetic/electric field, nor mechanical stress. They thus obviously reveal the potential of Mn_4N thin films as a new spintronic material, consisting of only cheap elements, and might be a milestone to replace rare earth-based spintronic materials such as TbFeCo, GdFeCo.

Chapter 1 Introduction

Electronics had drastically been developed since the discovery of the point-contact transistor in 1947, by Bardeen and Brattain¹, and of the p-n junction bipolar transistor in 1948 by Shockley². Semiconductor devices solved problems posed by older devices such as vacuum tubes, such as the difficulty of the miniaturization, the high power consumption and short life time. Kilby and Noyce soon invented the integrated circuit (IC), which allows transistor miniaturization^{3,4}. The number of transistors on one chip has increased roughly according to the Moore's law since then: the device density has increased exponentially, twice per 18 months to 24 months⁵. Additionally, device miniaturization provided not only a higher density, but also lower power consumption, faster operation and a better yield of chips per wafer⁶.

This result ensured a fast development of electronics and of the associated nanofabrication technologies. Computer dimensions shrank, as well as their power consumptions, their sizes and their prices, resulting in the worldwide spread of silicon-based semiconductor technology, both for home use and for industrial applications.

However, around the end of 20th century the miniaturization process began to be slow down, because of several quantum effects or technological problems, such as the leakage of the gate charge by tunneling, which leads to an increase in power consumption, or the difficulty of nanofabrication when approaching the atomic limit, which induces a cost increase.

Severe options are envisioned to overcome these limits⁷:

1. More Moore: continuing miniaturization using new technologies such as extreme-ultraviolet lithography, or 3D integrations for processing and storage devices.
2. More than Moore: diversifying the functions and application of chips such as power management, interact, MEMS, sensing, etc.
3. Beyond CMOS: Employing new techniques or materials in replacement or complement of the ubiquitous silicon-based CMOS technology.

Electronics relies on control and detection of the electrons. For example, MOSFETs (Metal-oxide-Semiconductor Field Effect Transistors) enable to switch in-between two states of low and high resistance, corresponding to "0" and "1"^{8,9}. The operation is based on the voltage control at the gate terminal of the current through the channel. The information is stored as a charge on the gate electrodes, which acts as a capacitor. However, this information is volatile, i.e., it is lost when the power is turned off. To make matters worse, the smaller the devices, the bigger the power consumption due to the charge leakage is. Therefore, the creation of non-volatile memories, which can retain the information without power supply, is desired to reduce the static power consumption, and to obtain a normally-off computing¹⁰.

Spin electronics or Spintronics is an electronic based on the electron spin manipulation, which in its 30 years of existence has allowed developing and commercializing several applications, and which is currently amongst the more promising beyond CMOS approaches¹¹. It is naturally non-volatile, as it is based on the magnetization direction of ferromagnetic materials, and it has already been applied to develop several data storage

techniques such as magnetic tapes, magneto-optical disks and hard disk drives, key element of the rising age of the Big Data. In addition, the discovery of giant magnetoresistance (GMR)^{12,13}, tunneling magnetoresistance (TMR)^{14,15} and spin-transfer torque (STT)^{16,17} realized the fundamental spintronics concept, that is, detecting and controlling the direction of magnetization electrically, *i.e.*, without requirement of a magnetic field. Thus, Magnetoresistive Random Access Memories (MRAMs) a new generation of devices driven by electric currents, have been attracting attentions as embedded memories. Although MRAMs are already commercialized, they still have to compete with conventional DRAM and Flash memories, and many research projects concerning the creation of magnetic memories are in progress, from rather fundamental science to advanced technologies.

For the past two decades, current induced domain wall motion (CIDWM) devices have also been attracting attention from the spintronics communities. CIDWM is one of the phenomena caused by the STT: magnetic domain walls (DWs) move in opposite direction to the injected current, with typical speeds of 10^0 – 10^2 m/s. This phenomenon is expected to be used to develop memory devices such as racetrack memories¹⁸ and DW-motion MRAM¹⁹.

After lots of efforts on soft in-plane magnetic materials such as NiFe^{20,21,22,23,24}, the community focused on the use of non-centrosymmetric stacks including spin-orbit materials, with Dzyaloshinskii-Moriya interaction (DMI) and perpendicular magnetization. The idea was that the spin-orbit torques (SOT), discovered in 2010^{25,26,27} could allow obtaining small critical currents and high DW velocities.

Another way to enhance the efficiency of the current induced torque emerged more recently^{28,29}. SOTs are basically due to the transfer of an angular momentum, created by the Rashba-Edelstein or the spin Hall effects, to the ferromagnet magnetization. If the spontaneous magnetization is small, the ability of this angular momentum transfer to rotate the magnetization direction is expected to be high. For STT, one also aims at a perpendicular magnetization to reduce the operation current density. Therefore, rare-earth based ferrimagnetic materials with PMA such as TbFeCo or GdFeCo have been recently actively studied for CIDWM, especially close to the compensation point to minimize the spontaneous magnetization. However, the rare-earth elements have problems concerning material criticality, such as supply risk and sustainability³⁰. Therefore, replacement of them by cheap and abundant materials such as 3d metals is highly desirable.

In this manuscript, we will focus on a new kind of ferrimagnet thin films: anti-perovskite ferromagnetic nitrides, which are rare-earth free candidates for spintronic applications. Among them, Mn₄N thin films possess small spontaneous magnetization, around 100 kA/m, a relatively high perpendicular magnetic anisotropy, with an anisotropy field of 4 T and a perpendicular magnetization³¹. Such features are exciting to develop CIDWM devices. However, there has been only few reports of the magneto-transport properties of this material, and nothing about CIDWM. The aim of my PhD was thus to explore the potential of Mn₄N thin films for spintronics application and was the aim of this joint PhD between Tsukuba and Grenoble Universities.

The manuscript is organized within 7 chapters, including this introduction. Chapter 2 provides the theoretical and experimental background concerning CIDWM and ferromagnetic nitrides. Chapter 3 gives the experimental results of measurements of the magnetic properties of Mn₄N thin films, focusing on the comparison

of the growth on two different substrates, MgO and SrTiO₃. Chapter 4 presents the experimental results of CIDWM by STT under DC, measuring electrically the variation of magnetization switching fields with the applied current into microstrips devices. Chapter 5 is devoted to the measurement of DW speeds by MOKE microscopy and using current pulses. Chapter 6 introduces the magnetic properties of Mn_{4-x}Ni_xN alloys grown on SrTiO₃ substrates. We proposed a simple model to explain drastic variations of the magnetic properties, caused by Ni introduction, showing that we can determine the compensation concentration of Mn_{4-x}Ni_xN systems. Finally, in chapter 7, we summarize the contents of this thesis.

Chapter 2 State of the art

2.1. History of spintronics

During the last 30 years, the development of spintronics, which has led to the discovery of several new phenomena, has largely benefited from the progresses in nanotechnology. Table 2-1 summarizes the chronology of spintronics research in metallic and semiconductor materials from the discovery of GMR to the middle of 2000's, by giving a few milestones³².

In metallic systems, the discovery of magnetoresistances such as GMR and TMR were quickly used to develop read-heads for hard disk drives. The discovery, at the beginning of the century, that it is possible to control the magnetization electrically by spin-transfer torque attracted a large attention, and allowed to realize field-free operation of MRAMs. In parallel, semiconductor-based spintronics was born by doping III-V semiconductor such as InAs and GaAs by magnetic elements like Mn.

Table 2-1: Chronology of spintronics research from the discovery of GMR to the middle of 2000's³². Important findings, research, and events related to spintronics studies are summarized by classifying them into those related to metals (left column) and to semiconductors (right column).

Year	<Metal field>			Year	<Semiconductor field>
1988	Discovery of the GMR (Fe/Cr superlattice) ^{12,13}	Spin-dependent conduction	Current-induced magnetism	1990	Proposal of the Spin FET ³³
1995	TMR at room temperature ^{14,15}			1992	Development of (In, Mn)As ³⁴
1996	Theoretical predictions of STT ^{16,17}			1999	TMR of magnetic semiconductors ^{35,36}
1998	Practical application of GMR (reading head)				Optical detection of the spin injection ³⁷
2001	Non-local spin injection in nanodevices ³⁸			Control of magnetization	Spin-injection phenomena
2003	Microwave oscillation by current ⁴⁰	2002	Magnetization induced by light ⁴¹		
2004	Practical application of TMR (reading head)	2004	Magnetization reversal by spin injection ⁴²		
	Current-induced DW motion ²⁰		Current-induced DW motion ⁴³		
	Giant TMR in MgO tunnel junction ^{44,45,46}		Spin Hall effect ^{47,48}		
2006	Practical application of MRAM	2005	Electrical control of the spin precession ⁴⁹		
	First experiments on the Spin Hall effect ^{50,51,52}	2007	Electrical detection of the spin injection ⁵³		
2007	Practical application of MgO-TMR head		Spin injection and detection in Si ^{54,55}		

Table 2-2 presents the chronology of spintronics in the last 10 years⁵⁶. In the last 10 years, the interest towards pure spin currents and spin-orbit effects increased in both metallic and semiconductor materials, replacing the focus on classical STT by spin polarized currents. Thus, the attention of the community has been directed not only towards ferromagnets and ferromagnetic semiconductor, but also towards heavy metals with strong spin-orbit interactions (such as Pt, W or Ta), topological insulators, and two-dimension electrons gas at Rashba interfaces. One of the main concepts of such a post spintronics research is spin-charge conversion: generation of pure spin current by charge current and its reverse process. Spin Hall effect (SHE) and the Rashba-Edelstein effect have realized the conversion from conventional charge current to transverse pure spin current and vice versa. In spin caloritronics, the combination of SHE and spin Seebeck effect realizes the novel thermo-electric device:

conversion from thermal flow to spin current (spin Seebeck effect) and from spin current to charge current (inverse SHE). Spin orbitronics includes lots of phenomena caused by spin-charge conversion⁵⁷, for instance, generation and detection of spin current, spin accumulations, producing SOT to switch magnetization and move DWs, and magnonic charge pumping.

Table 2-2: Chronology of spintronics research in the last decade⁵⁶, concerning metallic systems.

Bold words mean the new subfields of spintronics.

2007	Electric field effect on metallic magnet (Electrolytic cell) ⁵⁸
	Giant spin Hall effect at RT ⁵⁹
2008	Magnetization control by pure spin current ⁶⁰
	Discovery of the Spin Seebeck effect ⁶¹ → Spin caloritronics
2009	Electric field effect on metallic magnet (Solid stack structure) ⁶²
	CoFeB/MgO MTJ with PMA ⁶³
2010	Discovery of spin current in ferromagnetic insulator ⁶⁴
2011	SOT-driven DW motion ^{25,26,27} → Spin orbitronics
2012	The role of DMI for SOT-induced DW motion ⁶⁵
	Development of Skyrmion by DMI ⁶⁶
2013	Discovery of spin peltier effect ⁶⁷
2016	Mechanical production of spin current ⁶⁸ → Spin mechanics

2.2. Magnetic domain wall (DW) and dynamics

This work focuses on current-induced DW motion (CIDWM) in a ferrimagnetic material. Let us introduce in this section the theoretical basics of DW statics and dynamics, the torque acting on magnetic moments, and some representative reports concerning CIDWM research.

2.2.1. Energies in ferromagnets

In a magnetic system, the spatial orientation of the magnetization is determined by the balance of several magnetic energies. Let us list up the energies leading to configurations possessing magnetic domains and DWs. The contributions to the total energy are hereafter presented as energy densities. Note that in this thesis, bold letters are vectors, and the middle dot “ \cdot ” corresponds to the scalar product. All formulae are in SI units.

The Zeeman energy E_z corresponds to the interaction between the magnetic field \mathbf{H} and the magnetization \mathbf{M} ,

$$E_z = -\mu_0 \mathbf{M} \cdot \mathbf{H} \quad (2-1)$$

where μ_0 is the vacuum permeability $4\pi \times 10^{-7}$ N/A². Needless to say, the system is more stable when \mathbf{M} and \mathbf{H} are parallel.

The magnetic anisotropy can be of different origins: crystalline anisotropy, shape anisotropy, or interfacial anisotropy. The shape anisotropy will be discussed later, as it actually arises from the demagnetizing field (or dipolar) energy. The magnetocrystalline anisotropy energy density E_c is determined by the relative angle between certain crystalline axis and magnetization. Here, we focus on a system possessing a uniaxial anisotropy. By defining the relative angle θ between the main axis and the magnetization, the anisotropic energy density is

given by

$$E_c = K_u \sin^2 \theta = \frac{K_u}{2} (1 - \cos 2\theta) \quad (2-2)$$

where K_u is the uniaxial anisotropy constant.

In this context, the interfacial anisotropy density E_I , in J/m^3 , is given by,

$$E_I = \frac{K_I}{t} \sin^2 \theta = \frac{K_I}{2t} (1 - \cos 2\theta) \quad (2-3)$$

where K_I is the interfacial anisotropy constant, in J/m^2 , and t is the thickness of the magnetic thin films. As shown in eq. (2-3), the volumic anisotropy density is inversely proportional to the thickness. Therefore, it is necessary to fabricate films as thin as possible to obtain large uniaxial anisotropies. For examples, Co/Pt and CoFeB/MgO systems possess relatively large interfacial anisotropies and are widely investigated for applications^{69,70}. But requires nanometer thick layers.

The exchange interaction between neighboring magnetic moments is a quantum effect, at the origin of ferromagnetism, ferrimagnetism, and antiferromagnetism. The energy of the exchange interaction for two neighboring spins \mathbf{S}_i and \mathbf{S}_j is given by,

$$\epsilon_{\text{ex}} = -J \mathbf{S}_i \cdot \mathbf{S}_j \quad (2-4)$$

where J is the exchange integral. Note that this quantity is not the density per volume unit. A positive (negative) value of J leads to ferromagnetism (respectively to ferrimagnetism or antiferromagnetism). To extend this expression to continuous systems, one can note that,

$$\begin{aligned} \epsilon_{\text{ex}} &= -J \mathbf{S}_i \cdot \mathbf{S}_j \\ &= -JS^2 \cos(d\theta) \\ &\approx -JS^2 \left[1 - \frac{(d\theta)^2}{2} \right] \\ &\approx \text{Constant} - \frac{JS^2 a^2 (d\theta)^2}{2 a^2} \\ &\approx \text{Constant} - \frac{JS^2 a^2}{2} \left(\frac{d\theta}{dx} \right)^2 \end{aligned} \quad (2-5)$$

where $d\theta$ and a are the relative angle and the distance between neighboring moments. After normalization of the energy by the lattice volume a^3 and expansion to 3D, the exchange energy density is given in a continuous model by

$$E_{\text{ex}} = A(\nabla \mathbf{m})^2, A = \frac{JS^2}{2a} \quad (2-6)$$

where A is the exchange stiffness constant.

The magnetic dipolar energy E_d arises from the long-distance dipolar interactions between all the magnetic moments of the system. When the magnetization is homogeneous, and when the shape of the system is an ellipsoid (note that cylinders, spheres and thin films are ellipsoids), a simple expression of E_d can be derived, in which a dipolar field H_d acts on the magnetization through a Zeeman-like energy,

$$E_d = -\frac{\mu_0}{2} \mathbf{M} \cdot \mathbf{H}_d, \mathbf{H}_d = -\bar{\mathbf{N}} \mathbf{M} \quad (2-7)$$

where $\bar{\mathbf{N}}$ is the demagnetizing tensor, which depends on the shape of the system. Note that the role of the dividing factor 2 is to cancel double-counting the work to move the magnetic charge against H_d caused by the charge itself. Mathematically, E_d can be also derived by,

$$\begin{aligned}
E_d &= - \int_0^M \mathbf{H}_d \cdot d\mathbf{m} \\
&= \int_0^M \bar{N} \mathbf{m} \cdot d\mathbf{m} \\
&= \frac{\mu_0}{2} \mathbf{M} \cdot \mathbf{H}_d
\end{aligned}$$

where \mathbf{m} is the assumed elementary magnetization.

In ferromagnetic thin films, the demagnetization tensor is diagonal with only one non-zero demagnetizing factor, along z , and equal to 1. It can be shown that in thin films, the demagnetizing field energy density can be written

$$E_d = \frac{\mu_0}{2} M_S^2 \sin^2 \theta = K_d \sin^2 \theta \quad (2-8)$$

where K_d is called the shape anisotropy or dipolar constant, θ is the angle between the z axis and the magnetization, and M_S the spontaneous magnetization. The perpendicularly magnetized state has a higher energy and is a priori unstable. Therefore, in absence of anisotropy energy and of any field, the magnetization in thin film tends to lie in-plane. This interaction is thus called shape anisotropy. Note that the expression of the shape anisotropy and of the uniaxial anisotropy (eq. 2-2) are very similar. To obtain perpendicularly magnetized thin film, the uniaxial anisotropy K_u must overcome K_d , the difference between those constants being called the effective uniaxial anisotropy K_u^{eff} . If it is positive, the magnetization is out-of-plane.

2.2.2. Formation of magnetic domains

In a real thin film, the magnetization is not homogeneous, and the dipolar energy can be reduced by forming closed loop of stray field. Several areas, called magnetic domain, possess different directions of magnetization. From the viewpoint of minimizing the dipolar energy, the smaller the domains, the more stable the system is. However, the boundary of domains, called domain walls (DWs), have a cost in magnetic anisotropy energy and exchange energy. In a system with uniaxial anisotropy, the width of the DWs is determined by the balance between E_{ex} and E_c , resulting in a width of $\Delta = \sqrt{A/K_u}$ (a prefactor sometimes appear in this formula: as the magnetization rotates continuously). The energy increment per surface unit due to a DW is $\sigma_{\text{DW}} = 4\sqrt{AK_u}$. Therefore, the spatial period of domains is determined by the balance among E_d , E_{ex} , and E_c . A quantitative analysis of the domain period is discussed in ref. [71] and mentioned in the chapter 3 of this thesis.

2.2.3. Magnetization dynamics

The magnetization dynamics is described in absence of spin transfer torque by the Landau-Lifshitz-Gilbert (LLG) equation^{72,73}, given by

$$\frac{d\mathbf{m}}{dt} = \gamma_0 \mathbf{H}_{\text{eff}} \times \mathbf{m} + \alpha \mathbf{m} \times \frac{d\mathbf{m}}{dt} \quad (2-9)$$

where \mathbf{m} is the unit magnetization vector (\mathbf{M}/M_S), γ_0 is the gyromagnetic ratio, and α is the phenomenological damping constant. H_{eff} is the effective field, *i.e.*, the sum of the external fields and of any other effect acting on magnetization such as the magnetic anisotropy. This is generally calculated by considering how the total energy varies with \mathbf{m} ,

$$\mathbf{H}_{\text{eff}} = -\frac{1}{\mu_0 M_S} \frac{dE}{d\mathbf{m}} \quad (2-10)$$

where E is the total energy. The first term of the LLG equation corresponds to the Larmor precession of the magnetic moment around the effective field. The second term, added by Gilbert, is the damping term, which corresponds to the relaxation of the magnetic moment. Figure 2-1 shows the schematic of the torques acting on the magnetization.

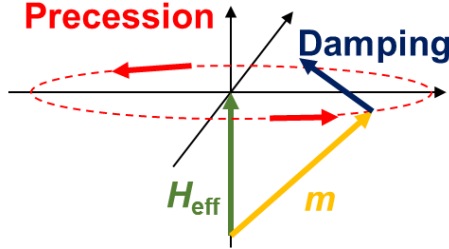


Figure 2-1: Geometrical relationship between the magnetization, the effective field and the precession and damping torques.

2.2.4. Spin-transfer torque (STT)

In 1996, the torque caused by spin polarized current, termed spin-transfer torque (STT), has been theoretically proposed^{16,17}. In a zone where the magnetization is rotating, such as a DW, the spin transfer can be taken into account by adding two terms to the LLG equation^{74,75}. For magnetic DWs,

$$\frac{d\mathbf{m}}{dt} = \gamma_0 \mathbf{H}_{\text{eff}} \times \mathbf{m} + \alpha \mathbf{m} \times \frac{d\mathbf{m}}{dt} - (\mathbf{u} \cdot \nabla) \mathbf{m} + \beta \mathbf{m} \times [(\mathbf{u} \cdot \nabla) \mathbf{m}] \quad (2-11)$$

$$\mathbf{u} = \frac{g\mu_B P}{2eM_S} \mathbf{J} \quad (2-12)$$

where \mathbf{u} is the spin-drift velocity, g is the g -factor, μ_B is the Bohr magneton, P is the spin polarization of the current, e is the elementary charge, and \mathbf{J} is the current density vector along the direction of electrons.

The third term is the damping-like or adiabatic torque, it tends to align \mathbf{m} with the spins of the incoming electrons. The fourth one is the field-like or non-adiabatic torque, whose direction is the same as the first term and thus assist the precession of magnetization.

Figure 2-2 presents the geometry of these four torques⁷⁶. When the conduction electrons go through the DW and enter the next domain, their spin moments rotate by 180° to be aligned with the magnetization of surrounding localized electrons. This is associated to a transfer of angular momentum to the magnetization of localized electrons, thus acting as a torque.

The existence of the STT was experimentally confirmed a few years after its prediction by current-induced magnetization switching^{77,78}, and spin wave excitations⁷⁹. This phenomenon is the key to manipulate magnetization without magnetic field and miniaturize spintronic devices.

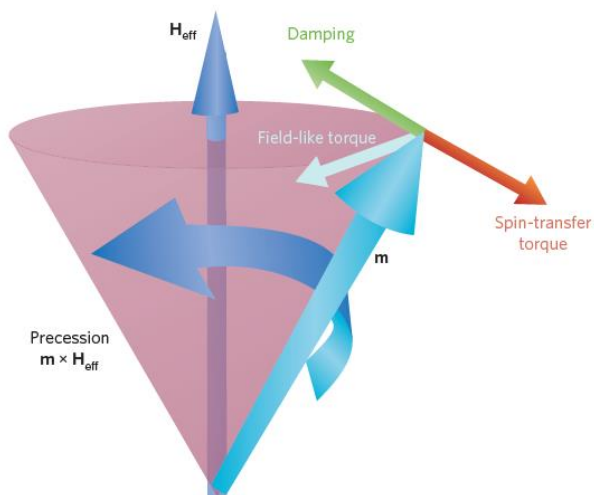
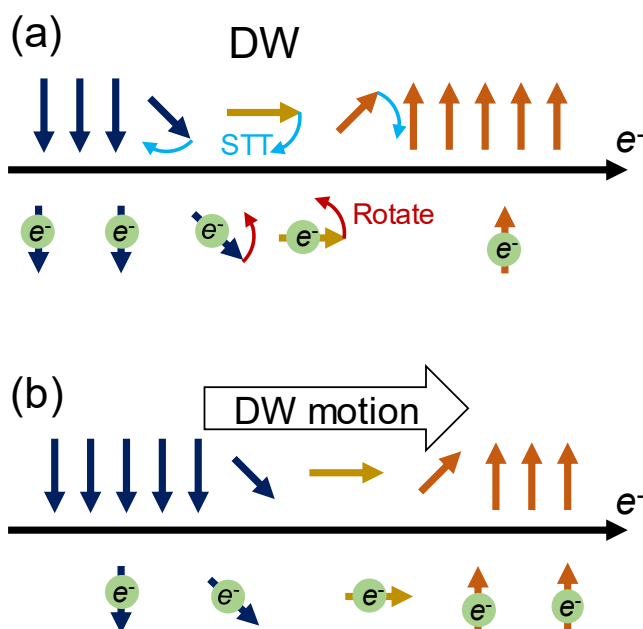


Figure 2-2: Schematic illustrations of STT⁷⁶ and of the different torques acting on a magnetic moment.

2.2.5. Current-induced domain wall motion

Let us now focus on current induced domain wall motion (CIDWM) in magnetic strips, which is one of the main topics of this work. CIDWM is one of the forms of STT-driven magnetization reversal⁸⁰. Let us consider a flow of electron through the DW. Figures 2-3 are schematic illustrations of a simplified CIDWM mechanism, considering only the damping-like STT. In practical systems, magnetic moments are also submitted to the precession torque, the damping torque and the field-like STT, leading to a more complex dynamics combining DW motion and magnetization precession within the DW⁸¹.



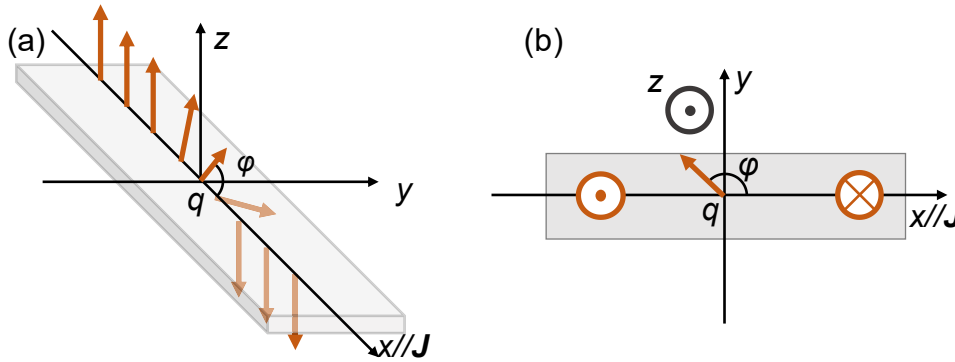
Figures 2-3: Schematic illustrations of CIDWM. Arrows denote magnetic moments. Electrons flows from left side to right side. (a) When electrons go through the DW, the spins rotate to be aligned along the localized magnetic moments. As a reaction, a STT acts on the localized moments. (b) As the STT acts on localized moments, the DW moves in the same direction as the electrons flow.

Let us review the DW dynamics features under applied magnetic field and spin-polarized current using the 1D model proposed by Malozemoff and Slonczewski⁸². Figures 2-4 present the schematic of the perpendicularly magnetized 1D model, where we assume the distribution of magnetization along y and z axis to be uniform, *i.e.* $\frac{\partial \mathbf{m}}{\partial y} = \frac{\partial \mathbf{m}}{\partial z} = 0$. To describe the DW motion in the 1D model, two collective coordinates are chosen: the DW position q , and the azimuth of the magnetization in DW, φ . The DW profile is described in spherical coordinates by the following ansatz:

$$\theta(x, t) = 2 \arctan \exp\left(\frac{x - q(t)}{\Delta}\right), \phi(x, t) = \varphi(t) \quad (2-13)$$

where $\mathbf{m} = (\sin \theta \cos \phi, \sin \theta \sin \phi, \cos \theta)$. Using a Lagrangian approach⁸³ one can find the equations of motion under a current (applied along $+x$) and a magnetic field applied along the easy-axis z :

$$\frac{1}{\Delta} \dot{q} - \alpha \dot{\varphi} = \frac{u}{\Delta} + \frac{\mu_0 \gamma H_K}{2} \sin 2\varphi, \dot{\varphi} + \frac{\alpha}{\Delta} \dot{q} = \beta \frac{u}{\Delta} + \mu_0 \gamma H_{\text{app}} \quad (2-14)$$



Figures 2-4: 1D model in magnetic strip. (a) Distribution of the magnetization in the vicinity of the DW. The orange arrows represent local magnetic moments. (b) Top view of (a). q and φ are the position of DW and the azimuth of magnetic moment in DW.

Here, $\Delta(\varphi) = \sqrt{\frac{A}{K_u + K_D(\varphi)}}$ is the DW width, where A is the exchange stiffness, K_u the uniaxial anisotropy, $K_D = \frac{\mu_0 M_s^2}{2} (N_x \sin^2 \varphi + N_y \cos^2 \varphi - N_z)$ (N_i being the demagnetizing coefficients), and $H_K = \frac{2K_D}{\mu_0 M_s}$ is the DW demagnetizing field [75].

When a DW is driven by a magnetic field, the DW moves in the steady regime with a constant value of φ up to a field called the Walker field (H_w). Above H_w , the DW moves by transforming continuously, *i.e.*, $\dot{\varphi} \neq 0$ (from transverse to vortex DW for in-plane systems and from Bloch to Néel DW in out-of-plane systems). This continuous transformation results in a drop of the velocity until it reaches a second linear v - H regime, with reduced mobility.

When the DW is driven by a spin polarized current, in the adiabatic limit ($\beta = 0$) the DW moves continuously only when it can start precessing and align with the incoming spin polarization. This occurs above a

critical current density J_c given by,

$$J_c = \frac{\mu_0 e}{\hbar P} \Delta(\varphi) M_s H_K \quad (2-15)$$

The last expression shows that J_c depends on the magnetization direction. In systems with in-plane magnetization, the transverse anisotropy constant is given by $K_D = |K_z - K_y| \approx |K_z| = \frac{1}{2} \mu_0 M_s^2 - K_u$. Introducing typical values, we obtain a transverse anisotropy constant of the order of 10^6 J/m². On the other hand, in thin films with perpendicular magnetization, the transverse anisotropy constant, which is related to the energy difference between a Bloch and a Néel DW, is small. In this case $K_D = |K_x - K_y|$. For a thin strip of thickness t and width w , the DW can be modeled as an ellipse and the demagnetizing factors can be approximated as $K_x \approx \frac{1}{2} \mu_0 M_s^2 \left(\frac{t}{t+\pi\Delta} \right)$, $K_y \approx \frac{1}{2} \mu_0 M_s^2 \left(\frac{t}{t+w} \right)$ [84]. Therefore, considering parameters of typical perpendicular ferrimagnetic nanostrips, we obtain a transverse anisotropy constant in the order of some 10^4 J/m³. This implies that the critical current density is much lower for these systems compared to systems with in-plane magnetization [85].

In the adiabatic limit, for current densities above J_c , the DW starts precessing and moves at a velocity given by,

$$\mathbf{v}_{\text{precession}} = \frac{1}{1 + \alpha^2} \sqrt{\mathbf{u}^2 - \mathbf{u}_c^2} \quad (2-16)$$

where u_c is the spin-drift velocity at the critical current density. When the critical current density is very small (as it is the case for systems with PMA), the latter expression can be approximated:

$$\mathbf{v}_{\text{precession}} \approx \frac{1}{1 + \alpha^2} |\mathbf{u}| = \frac{1}{1 + \alpha^2} \frac{g \mu_B}{2e M_s} P \mathbf{J} \quad (2-17)$$

This expression then shows that the DW mobility, v_{DW}/J , in the precessional regime is proportional to the ratio between the spin polarisation and the spontaneous magnetization. In conclusion, perpendicularly magnetized material with small M_s and large P are the best candidates for CIDWM devices.

2.2.6. Spin-transfer torque in ferrimagnetic materials

As mentioned in the introduction, ferrimagnetic materials have been actively investigated for CIDWM applications. In ferrimagnet, the LLG equation must be modified with consideration of multiple magnetic moments in sublattices. Several modifications of conventional (*i.e.* considering only precession and damping) LLG equation have already been reported in refs. [86, 87, 88]. In ferrimagnetic material possessing two antiparallel magnetic moments and in each sublattice, we can express individual LLG equations for these sublattices,

$$\dot{\mathbf{m}}_1 = \gamma_1 (\mathbf{H}_1 + H_0 \mathbf{m}_2) \times \mathbf{m}_1 + \alpha_1 \mathbf{m}_1 \times \dot{\mathbf{m}}_1 \quad (2-18)$$

$$\dot{\mathbf{m}}_2 = \gamma_2 (\mathbf{H}_2 + H_0 \mathbf{m}_1) \times \mathbf{m}_2 + \alpha_2 \mathbf{m}_2 \times \dot{\mathbf{m}}_2 \quad (2-19)$$

where \mathbf{m}_i , γ_i , \mathbf{H}_i , and α_i are a unit vector along magnetic moment, gyromagnetic ratio, effective field, and damping coefficient for sublattice i , respectively. H_0 denotes effective field caused by exchange interaction between each sublattice. Under a hypothesis that \mathbf{m}_1 and \mathbf{m}_2 remain in antiparallel state (*i.e.* H_0 is sufficiently large), $\mathbf{m}_1 \times \mathbf{m}_2$ is always zero, and we can derive a modified formula of total magnetization dynamics by combining eq. (2-18)

and (2-19) to be,

$$\dot{\mathbf{m}} = \gamma_{\text{eff}} \mathbf{H}_{\text{eff}} \times \mathbf{m} + \alpha_{\text{eff}} \mathbf{m} \times \dot{\mathbf{m}} \quad (2-20)$$

where $\mathbf{m} = \mathbf{m}_1 = -\mathbf{m}_2$ is the unit vector along total magnetization, γ_{eff} , \mathbf{H}_{eff} , α_{eff} are the effective parameters defined by,

$$\gamma_{\text{eff}} \equiv \frac{M_1 - M_2}{\frac{M_1}{\gamma_1} - \frac{M_2}{\gamma_2}} = \frac{M_S}{A_{\text{tot}}} \quad (2-21)$$

$$\mathbf{H}_{\text{eff}} \equiv \frac{M_1 \mathbf{H}_1 - M_2 \mathbf{H}_2}{M_1 - M_2} = \frac{M_1 \mathbf{H}_1 - M_2 \mathbf{H}_2}{M_S} \quad (2-22)$$

$$\alpha_{\text{eff}} \equiv \frac{\alpha_1 \frac{M_1}{\gamma_1} + \alpha_2 \frac{M_2}{\gamma_2}}{\frac{M_1}{\gamma_1} - \frac{M_2}{\gamma_2}} = \frac{\alpha_1 A_1 + \alpha_2 A_2}{A_{\text{tot}}} \quad (2-23)$$

where M_i and $A_i = M_i/\gamma_i$ are a spontaneous magnetization and an angular momentum at sublattice i , and M_S , A_{tot} are a total spontaneous magnetization and a total angular momentum, respectively. These results indicate the existence of two singularities at compensation points of angular momentum ($A_{\text{tot}}=0$) and magnetization ($M_S=0$). At compensation point of angular momentum where $A_1=A_2$, both γ_{eff} and α_{eff} diverge, resulting in instantaneous alignment of magnetization to the local effective field⁸⁷. This divergence of α_{eff} has been experimentally confirmed by ferromagnetic resonance measurement in all-optical pump and probe technique⁸⁸. At the compensation point of magnetization where $M_1=M_2$, γ_{eff} goes to zero and H_{eff} diverges. However, in eq. (2-20), H_{eff} is multiplied by γ_{eff} , canceling M_S term and keeping the product finite.

A. Canizo-Cabrera *et al.* suggested a new modification including adiabatic STT term in CPP-GMR stack in ref. [89]. Figure 2-5 illustrates the schematic diagram of the assumed geometry. Positive current means that electrons flow from free layer 1 to pinned layer 2. They formulized the STT acting to magnetic moment at i sublattice in the layer 1 as,

$$\mathbf{\Gamma}_i = \pm \frac{\gamma_i \hbar I_{e,i} g_i^\pm}{eV M_i} \mathbf{M}_i \times (\mathbf{m}_i \times \mathbf{m}_3) \quad (2-24)$$

where V is the volume of the layer 1, $I_{e,i}$ is the electric current flowing to the sublattice i , g_i^\pm is the coefficients for sublattice i depending on the spin polarization. The combination of this torque for each sublattice introduce the effective LLG equation by,

$$\dot{\mathbf{m}} = \gamma_{\text{eff}} \mathbf{H}_{\text{eff}} \times \mathbf{m} + \alpha_{\text{eff}} \mathbf{m} \times \dot{\mathbf{m}} \pm a_{\text{eff}}^\pm \mathbf{m} \times (\mathbf{m} \times \mathbf{m}_3) \quad (2-25)$$

where $a_{\text{eff}}^\pm = \frac{\hbar I_{e,1} g_1^\pm + I_{e,2} g_2^\pm}{eV A_{\text{tot}}}$ which corresponds to the spin-drift velocity. We can say that the amplitude of STT term diverges at the compensation point of angular momentum.

However, the authors of this report⁸⁹ optimized the expression for CPP-GMR stacks and thus the vector of STT is aligned to $\mathbf{m} \times (\mathbf{m} \times \mathbf{m}_3)$, not to $(\mathbf{V} \cdot \mathbf{u})\mathbf{m}$. Therefore, we derive the expression of STT in ferrimagnetic continuous wire in the context of semiclassical adiabatic description²⁰ from the balance between supplied and accepted angular momentum transition.

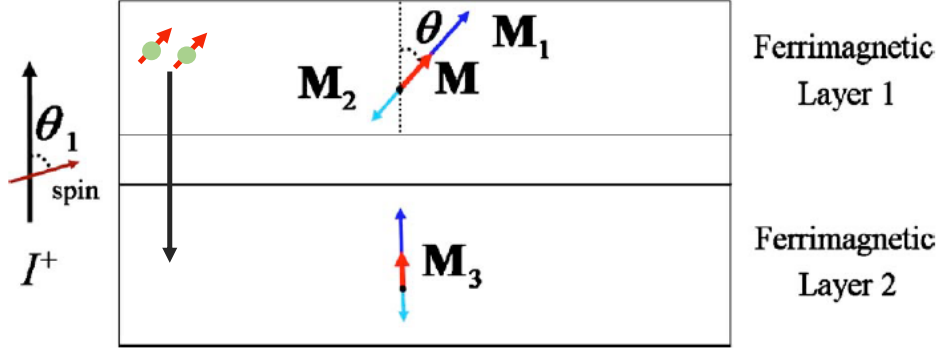


Figure 2-5: Schematic of assumed CPP-GMR stack consisting of two ferrimagnetic layers. Positive bias generates electrons flow from layer 1 to 2.⁸⁹

Figure 2-6 presents the schematic illustration of 1D model discussed here. We focus on the unit cell whose length is dx , cross-section is S , and unit vector of magnetization is $\mathbf{m}(x)$. Supplied angular momentum per unit time is calculated as the product of spin angular momentum $\hbar/2$, the number of flowing electrons I/e , the spin polarization of current P , and relative vector of magnetizations as given by,

$$(\text{Supplied}) = \frac{\hbar I}{2e} P \times [\mathbf{m}(x - dx) - \mathbf{m}(x)] = \frac{\hbar I}{2e} P \times \left(-\frac{\partial \mathbf{m}}{\partial x} dx \right) \quad (2-26)$$

On the other hand, accepted angular momentum per unit time dt can be given by,

$$(\text{Accepted}) = \left(\frac{M_1}{\gamma_1} - \frac{M_2}{\gamma_2} \right) S dx \frac{\mathbf{m}(t + dt) - \mathbf{m}(t)}{dt} = A_{\text{tot}} S dx \frac{\partial \mathbf{m}}{\partial t} \quad (2-27)$$

STT is derived as the time derivative of magnetization vector,

$$\frac{\partial \mathbf{m}}{\partial t} = \frac{\hbar P j}{2e A_{\text{tot}}} \left(-\frac{\partial \mathbf{m}}{\partial x} \right) = -u_{\text{eff}} \frac{\partial \mathbf{m}}{\partial x} \quad (2-28)$$

$$u_{\text{eff}} \equiv \frac{\hbar P j}{2e A_{\text{tot}}} = \frac{\hbar \gamma_{\text{eff}} P j}{2e M_S} = \frac{g_{\text{eff}} \mu_B P j}{2e M_S}, \left(g_{\text{eff}} = \frac{\hbar \gamma_{\text{eff}}}{\mu_B} \right) \quad (2-29)$$

Thus, the spin-drift velocity in a ferrimagnet u_{eff} has been derived. This corresponds to replacing the g -factor in the conventional u by an effective one. In conclusion, the spin-drift velocity in ferrimagnetic materials u_{eff} is diverging at the compensation point of not magnetization but angular momentum and then extremely efficient STT can be expected.

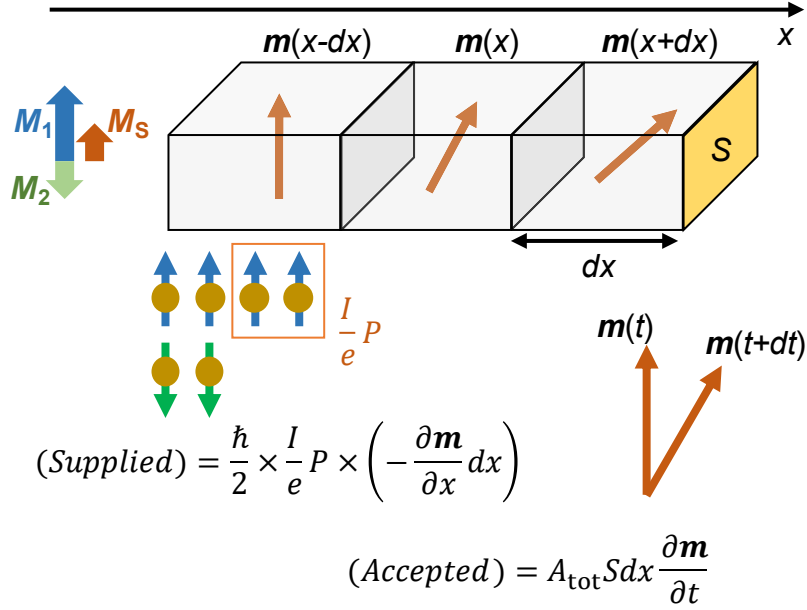


Figure 2-6: Schematic illustration of supposed 1D model.

Very recent report introduced SOT terms into ferrimagnet-LLG equations, resulting in ultrafast CIDWM at compensation temperature of angular momentum T_A at 260 K²⁸. The DW velocities in ferromagnet (v_{FM}) and ferrimagnet (v_{FiM}) are obtained by replacing γ and α by γ_{eff} and α_{eff} ,

$$v_{FM} = \frac{\gamma \pi}{M_S} \frac{D j_{HM}}{2 \sqrt{j_{HM}^2 - \alpha j_0^2}}, \left(j_0 = \frac{2etD}{\hbar \theta_{SH}^{eff} \Delta} \right) \quad (2-30)$$

$$v_{FiM} = \frac{\pi}{2} \frac{D j_{HM}}{\sqrt{(A_{tot}(T) j_{HM})^2 - (A_0 j_0)^2}}, (A_0 = \alpha_1 A_1 + \alpha_2 A_2) \quad (2-31)$$

where D , j_{HM} , t , θ_{SH}^{eff} , and Δ are the DMI parameter, the current density through the heavy metal layer, the magnetic layer thickness, effective spin Hall angle, and DW width, respectively. Thus, v_{FiM} increase with current density linearly at the compensation point of angular momentum while v_{FM} saturates toward $\gamma \pi D / 2 M_S$. In conclusion, ferrimagnetic materials whose angular momentum is compensated possess singularities of γ , α , and spin-drift velocity u and also result in high DW velocity driven by SOT.

2.3. Experimental reports of CIDWM

CIDWM has been reported since 2004. Yamaguchi *et al.* moved a DW in a 240-nm-wide permalloy nanostrip by current pulses²⁰. The DW positions were detected by magnetic force microscopy. After this report, some groups successfully achieved CIDWM in permalloy strips^{90,91}. However, as mentioned above, the threshold current density in in-plane magnetized strips ($\sim 10^{12}$ A/m²) is much higher than what is expected in out-of-plane magnetized systems ($\sim 10^{11}$ A/m²). Therefore, ferromagnetic materials with PMA have soon after attracted interest of researchers. Table 2-3 lists several examples of STT-driven CIDWM in PMA materials showing relatively high speeds, where j_C is a critical current density, v_{max} is the maximum DW velocity, and j_{max} is the current density injected to give v_{max} . η is the DW mobility, given by the ratio v_{max}/j_{max} . If one assumes that the DW velocity in the high current regime is proportional to the current density, η corresponds to $\frac{v_{DW}}{j} \sim \frac{g \mu_B}{2e M_S} P$.

Among these results, ref. [92] presents quite high DW speeds for high current densities, even though the material possesses high spontaneous magnetization of 600 kA/m. The ref. [93] is also surprising, exhibiting a relatively high speed for a small current density and a high mobility. This mobility exceeds the upper limit of the spin-drift velocity with the assumption of $P = 1$ with M_s in this system of 560 kA/m. The authors expect that CIDWM in this system results from field-like STT and of the small Gilbert damping constant of CoB layers, accelerating the DW below the precession regime. TbFeCo possess an extremely small j_c in ref. [94]. This may be due to the fact that it is fabricated on polycarbonate substrate by nanoimprinting technique, which leads to a defect-free edge of the microstrips. However, the maximal DW speed is smaller than others by one order of magnitude.

Table 2-3: The list of DW speeds driven by STT in several material and systems.

Material	$j_c[10^{11} \text{ A/m}^2]$	$j_{\max}[10^{11} \text{ A/m}^2]$	$v_{\max}[\text{m/s}]$	$\eta [10^{-10} \text{ m}^3/\text{C}]$	Ref
Co/Ni/Co	3.0	32	350	1.1	92
CoB/Ni	1.1	2.63	197	7.5	93
TbFeCo	0.06	2.4	60	2.5	94

Recently, the use of heavy metal (Pt, Ta, W, etc.) to inject pure spin currents to the ferromagnetic layers has been attracting a lot of interest. The corresponding new torque acting on magnetic moments, caused by spin Hall or Rashba-Edelstein effects, are called spin-orbit torques (SOTs). SOTs have led to faster and more efficient DW motion and magnetization switching⁹⁵. Representative experimental reports with remarkable DW velocities are listed in Table 2-4. In ref. [96], the authors employed a Pt/Co(3 Å)/Ni(7)/Co(1.5)/Ru/Co(t_a)/Ni(7)/Co(t_b) multilayer structure, where the magnetization of the upper ferromagnetic layer couples anti-ferromagnetically with that of the lower layer through a RKKY interaction (synthetic antiferromagnetic structure). By tuning the thickness t_a , t_b and thus the total magnetization, they successfully maximized the DW speed up to 750 m/s.

In the latest report [97], the authors employed ferrimagnetic GdCo on a Pt underlayer. They changed the sample temperature and searched for the compensation points of the total magnetization and of the angular momentum, resulting in a maximum DW velocity up to 1300 m/s for $2 \times 10^{12} \text{ A/m}^2$ at 260 K. Even at room temperature, this system still has high DW velocity of 850 m/s, indicating the great potential of rare-earth based ferrimagnetic materials for applications to CIDWM devices.

Table 2-4: Examples of DW speeds driven by SOT in several material and systems.

Material	$j_c[10^{11} \text{ A/m}^2]$	$j_{\max}[10^{11} \text{ A/m}^2]$	$v_{\max}[\text{m/s}]$	$\eta [10^{-10} \text{ m}^3/\text{C}]$	Ref
Pt/Co/AlOx	10	33	380	1.15	95
CoNiCo/Pt	5.0	33	750	2.27	96
GdCo/Pt(260 K)	4.4	20	1300	6.50	97
GdCo/Pt(300 K)	3.5	20	850	4.25	97

2.4. Anti-perovskite 3d-metal nitrides

In our group in Tsukuba, we have been focusing on ferromagnetic nitrides of 3d-metals such as $\text{Fe}_4\text{N}^{98,99}$, $\text{Co}_4\text{N}^{100,101}$, Mn_4N^{31} , $\text{Ni}_4\text{N}^{102}$, and their alloys^{103,104,105}, which possess an anti-perovskite structure. Figure 2-7 exhibits the crystalline structure of such alloys, consisting of a face-centered cubic (fcc) lattice of 3d metals surrounding a body-centered nitrogen atom. Two inequivalent sites are distinguished: the corner site is the I-site whereas the face-centered sites correspond to the II-site. In consideration of hybridization effects between $2p$ -orbitals of N and $3d$ -orbitals of the metal, the II-sites can still be decomposed in between IIA and IIB sites. They possess lattice parameters of around 3.7-3.9 Å, which is close to that of Si (100) ($a_{\text{Si}}/\sqrt{2}=3.84$ Å). Therefore, it is expected that they could be grown on commercially available Si (100)¹⁰⁶.

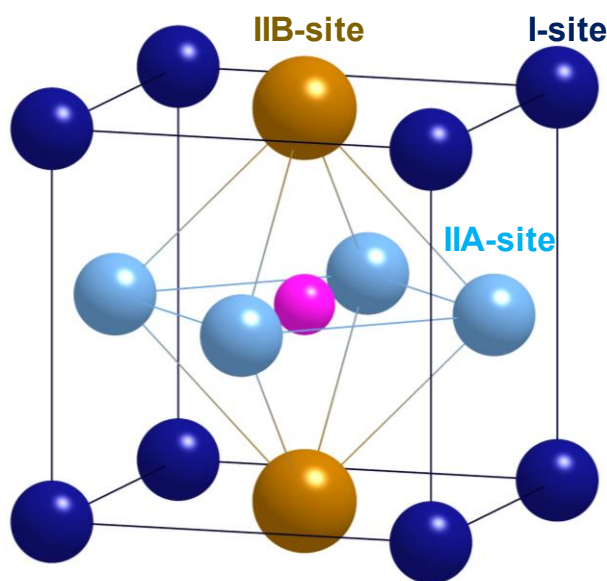


Figure 2-7: Crystalline structure of anti-perovskite nitrides.

2.4.1. Mn_4N

In this work, we focused on one of the 3d-metal nitrides, Mn_4N . The crystalline structure with magnetic moments is shown in Figure 2-8. Mn_4N showed to be ferrimagnetic by neutron diffraction on powder samples¹⁰⁷, with magnetic moments of $3.53\mu_B$ for the I-site and $-0.89\mu_B$ for the II-site at 300 K. The Néel temperature T_N was also measured in the same report to be 745 K, well above room temperature. In bulk form, the magnetization easy axis is oriented in the [111] direction, with non-collinear magnetization components at II-sites^{108,109}, tilted from the [111] direction by 16° as illustrated in Figures 2-9¹¹⁰. Bulk Mn_3AN (A=Zn, Ga, etc.) alloys are actively studied because of their large negative thermal expansion¹¹¹, caused by such non-collinear magnetic structure.

While bulk Mn_4N has been studied by more than half a century, thin film fabrication began more recently in 1994¹¹², on Si wafers, by sputtering. Table 2-5 summarizes several reports of Mn_4N thin films growth. The first Mn_4N thin films investigated already exhibited PMA, leading to a large out-of-plane remnant magnetization M_r and coercivity H_C than in-plane films, even though they possessed other phases like α -Mn with smaller M_s . In ref. [113], pure Mn_4N thin films, free from any secondary phase, have been deposited on

6H-SiC(0001) and GaN(0001) by reactive molecular beam epitaxy (MBE). The Mn_4N films were oriented along [111] axis, showed PMA, and a high T_N of 738 K, in agreement with the result obtained in bulk Mn_4N ¹⁰⁷.

In the last 5 years, (001)-oriented Mn_4N thin films with clearer PMA have been reported^{31,114,115,116}, grown on single crystalline oxide substrates such as MgO(001). These Mn_4N thin film have slightly distorted lattice of $c/a \sim 0.99$, where a and c are the out-of-plane and in-plane lattice constants, of 0.389 and 0.396, respectively. Several groups have reported a relatively strong perpendicular magnetic anisotropy ($K_u \sim 1-2 \times 10^5 \text{ J/m}^3$), and a small M_S of 100-200 kA/m. Magneto-transport properties have been also investigated^{114,116,117,118}, resulting in a relatively high and negative anomalous Hall angle $\theta_{\text{AH}} = \rho_{\text{AH}}/\rho$ of -2-3% at room temperature. However, there is still no report concerning its spin-polarization, nor STT experiment.

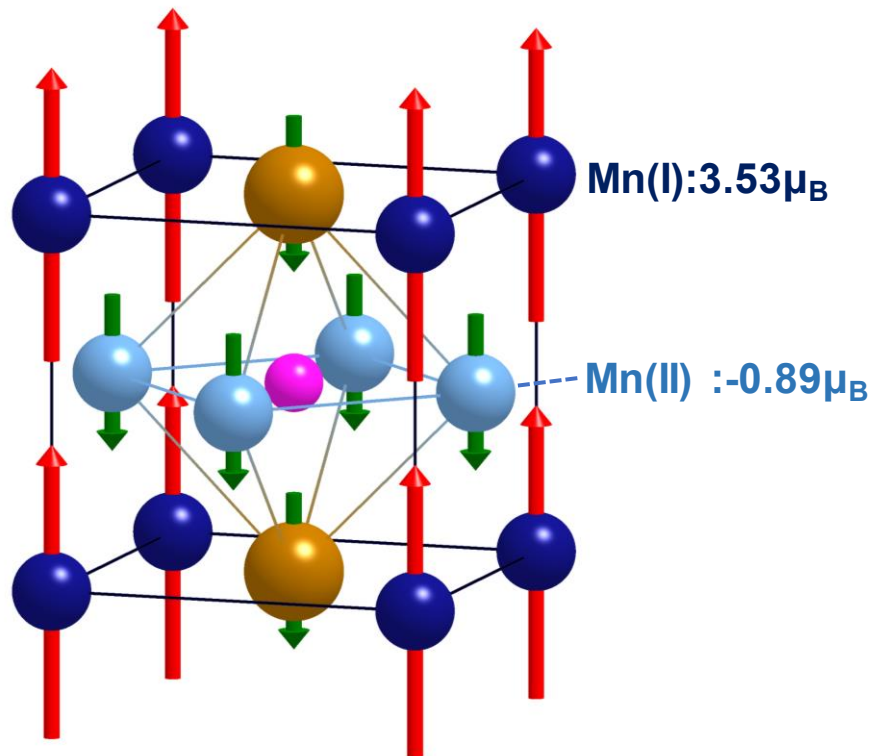
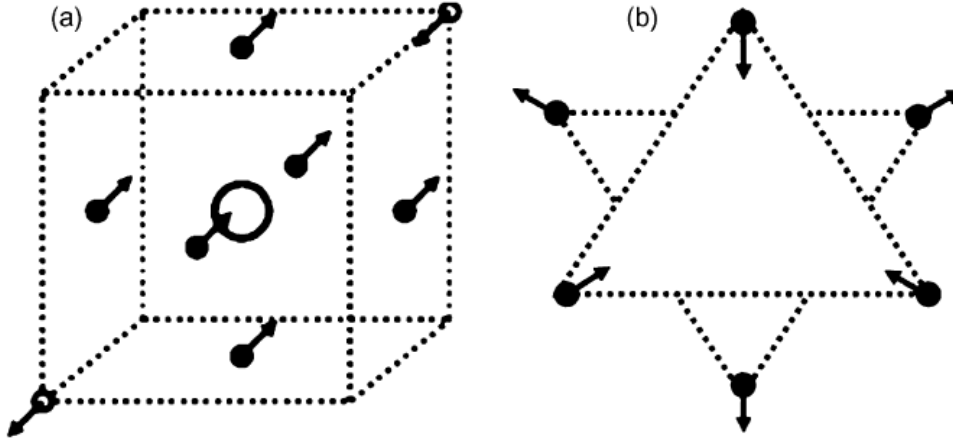


Figure 2-8: Crystalline structure and ferrimagnetic structure of Mn_4N .



Figures 2-9: (a) Magnetic structure of bulk Mn₄N and (b) its projection on (111) plane¹¹⁰.

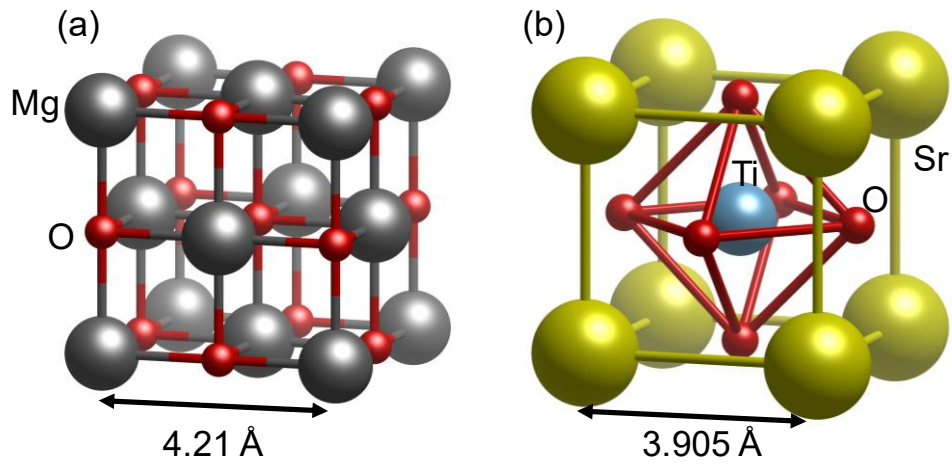
Table 2-5: Reports of Mn₄N growths on several substrates. † means qualitative PMA, confirmed from the out-of-plane hysteresis loops. The value of M_S is measured at 300 K.

Substrate	Method	K_u [MJ/m ³]	c/a	M_S [kA/m]	Orientation	Reference
Si(100)	Sputter	†	N/A	~49	(100) and (111)	K. M. Ching <i>et al.</i> , (1994). ¹¹⁹
Glass	Sputter			~49	(100)	K. M. Ching <i>et al.</i> , (1995). ¹²⁰
SiC, GaN	MBE			~80	(111)	S. Dhar <i>et al.</i> , (2005). ¹¹³
MgO, STO	MBE	0.22	0.99	145	(100)	Y. Yasutomi <i>et al.</i> , (2014). ³¹
MgO	PLD	0.16	0.99	157	(100)	X. Shen <i>et al.</i> , (2014). ¹¹⁴
MgO	Sputter	0.088	0.99	110	(100)	K. Kabara <i>et al.</i> , (2015). ¹¹⁵

2.4.2. Substrates

As mentioned in the last part, most researchers working on Mn₄N thin films have employed a MgO(001) single crystalline substrate, whose structure is shown in Figures 2-10 (a). However, the lattice mismatch $f = \frac{a_{\text{film}} - a_{\text{sub}}}{a_{\text{sub}}}$ between Mn₄N and MgO is large (-7.6 %), creating dislocations at the interface¹¹⁴. Our group has successfully grown Mn₄N thin films on SrTiO₃(STO)(001) substrates possessing a much better lattice matching of $f = -0.4$ % by plasma-assisted MBE³¹.

In the next chapter, we will attempt to characterize the difference between deposits made on MgO and STO substrates.



Figures 2-10: Crystalline structure of (a) MgO (NaCl cell) and (b) SrTiO₃ (Perovskite cell).

Chapter 3 Magnetic domain structure in Mn₄N thin films

As stated in chapter 2, rare-earth-based ferrimagnetic materials with PMA have recently attracted a large interest for spintronic applications. Indeed, their low magnetization value allows reducing the critical currents required to induce magnetization switching, using either spin-transfer-torques or spin-orbit torques. In this context, Mn₄N epitaxial thin films constitute an alternative material for current-induced DW motion without rare-earth.

In this chapter, we will present the magnetic properties of 2 Mn₄N layers grown by MBE on MgO and STO substrate. We will focus on the overall magnetic and transport properties, which are obviously of interest for the study of CIDWM, but also on the domain wall geometries, which can reveal features of the magnetization reversal, and in particular how strongly the DWs interacts with defects.

Although MgO is the substrate conventionally used to obtain epitaxial growth of Mn₄N thin films^{114,115}, we will show that Mn₄N/STO have more astonishing properties, with in particular a giant and previously unseen magnetic domain structure, at the millimeter length scale, with full remanence, scarce nucleation and a sharp magnetization switching¹²¹. We will demonstrate that these properties, associated to a very small magnetization and a large perpendicular magnetic anisotropy, underline the potential of Mn₄N/STO structure for spintronics applications.

In the first part, we introduce the detail of the growth conditions of Mn₄N films and the results of X-ray diffraction characterization performed on these films. In the second part, we will show the fundamental magnetic properties of these films, such as the *M-H* hysteresis curves, and the main magneto-transport properties (extraordinary Hall effect and magnon-magnetoresistance). In the third part, the magnetic domain texture is observed by magnetic force microscopy and magneto-optical Kerr effect microscopy, in the as-deposited state and in state partially reversed by magnetic fields. In the fourth and last part, we will compare the two type of deposits, and discuss the relationship between crystalline quality and DW properties.

3.1. Growth and structure

The magnetic films have been prepared by molecular beam epitaxy (MBE), as described in ref. [31,104], In this section, we will detail the crystal growth and the structure properties.

3.1.1. MBE growth of Mn₄N thin films

Figure 3-1 presents the schematic of our MBE system. It is equipped with ultra-high vacuum pumps (rotary pump, turbo molecular pump, ion pump), load-lock chamber, reflection high energy electron diffraction (RHEED) system, 3 Knudsen cells (K-Cells) for Mn and other metal source, a sputtering gun for capping material like SiO₂ or Ta, an RF-plasma gun with gas line for N₂ and Ar. The base pressure of the reaction chamber is in the order of 10⁻⁷ Pa, monitored by nude ion gauge and inverted magnetron gauge. The actual growth procedure of our film samples is shown below.

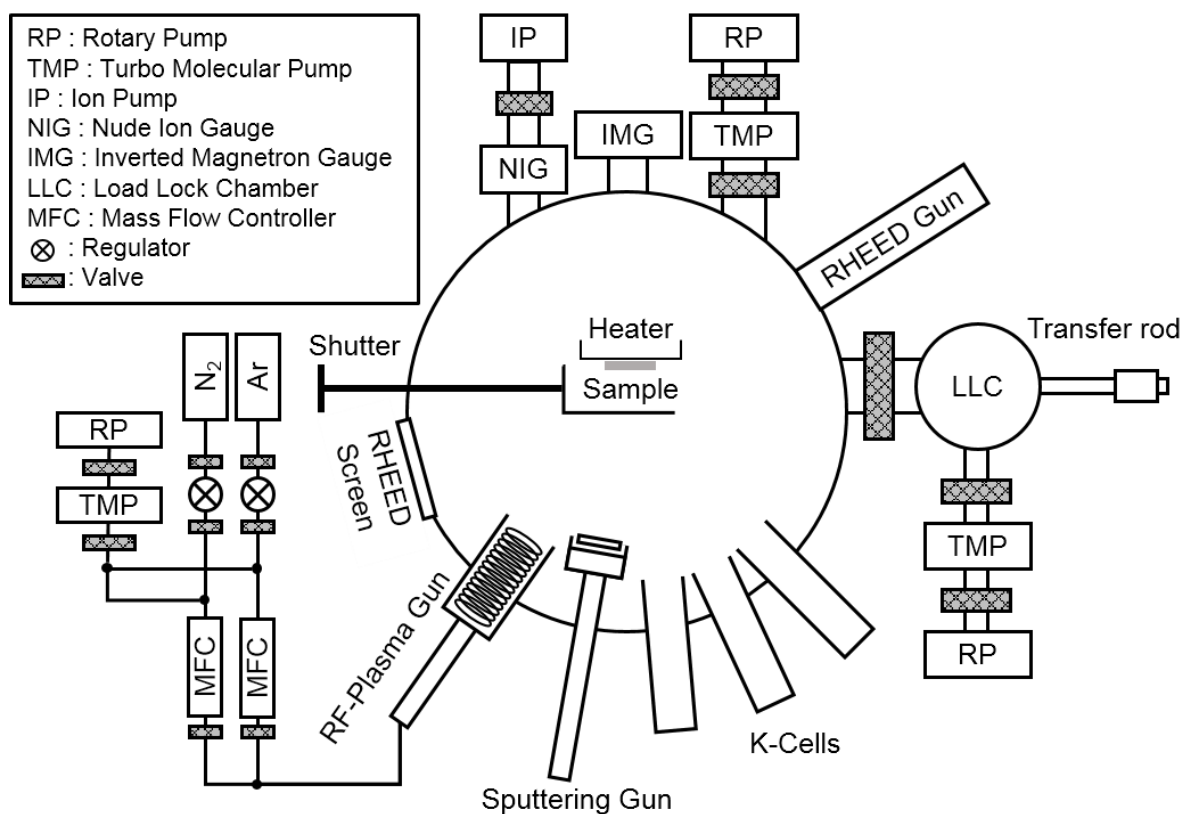


Figure 3-1: Schematic of the used MBE chamber

[1] Substrate preparation

2 kinds of 10×10×0.3-mm-sized substrate have been used, MgO(001) and STO(001). MgO wafers are washed with acetone and methanol in ultrasonic bath, but not in deionized water to avoid MgO dissolution. Before growth, the MgO wafer was annealed at 600 °C in the reaction chamber, in order to remove any organic contamination and to improve the surface state. STO wafer are etched in a buffered HF solution, whose composition is 5%-HF and 35%-NH₄F in weight ratio, to obtain Ti-O₂ terminated step surface³¹. To avoid generating oxygen vacancies, the STO was not annealed before growth.

[2] Deposition technique

Before deposition, 3 growth parameters are optimized: the nitrogen-supplying condition, the manganese deposition rate, and the substrate temperature T_s .

Concerning the gas condition control, the nitrogen is supplied as electrically neutral atoms through gas line and plasma gun exciting N-plasma. The pressure and flow rate are controlled by regulator and mass flow controller to 0.10 MPa and 1 sccm, respectively. Both cations and anions are removed by a 300 V ion trapper. The magnitude of the plasma excitation is monitored by the intensity of light emission in an optical spectrometer. Usually the input RF power, the gas pressure on the nude ion gauge and the intensity of the light emission at 336-nm wavelength are tuned at 105 W, 4.5 mPa and 2.3×10^3 counts per 3 ms, respectively.

The second parameter is the deposition rate, controlled through the temperature of the K-cells and of the

substrate. Metal atoms like Mn are evaporated using a K-cell. The rate at a given temperature is estimated by doing some deposition tests on Si wafers followed by thickness measurements by X-ray reflectometry. For Mn₄N growth, the Mn rate is kept around 1.3 nm/min, with a cell temperature of 835 °C. Mo is sputtered on the bottom of both substrates to let them absorb IR light and heat up more efficiently. During the growth, the substrate temperature is kept at 450 °C, in order to allow the diffusion of N atoms in Mn lattice, and the subsequent ordering of the crystal.

After the Mn₄N growth, the surface is capped by SiO₂ or Ta to prevent oxidation. During the SiO₂ or Ta deposition, Ar coming from a parallel gas line flows in the reactive chamber with a pressure of 0.1 Pa, which is monitored by an inverted magnetron gauge. The sputtering gun excites an Ar⁺ plasma, and sputters the target source to deposit SiO₂ or Ta on the substrate layer.

3.1.2. Crystallinity of the Mn₄N film

The crystalline quality of the films has been characterized by electron and X-ray diffraction method. Let us introduce briefly the principle of these techniques.

[1] Reflection high energy electron diffraction (RHEED)

Our MBE chamber has a RHEED system (cf. Figure 3-1: Schematic of the used MBE chamberFigure 3-1) to characterize the surface crystallinity in situ. A 10-100 keV electron beam is used to obtain ultrashort wavelengths and a high resolution. This electron beam is sent on a sample surface with grazing incident angle of 0.2-0.3° to obtain forward scattered diffraction patterns on the screen. Figure 3-2 shows the schematic diagram of a typical RHEED system¹²². By tuning the x-y direction of the electron beam, the focus and the brightness, the contrast of the diffraction pattern can be optimized. As shown in Figures 3-3, the RHEED pattern depends on the orientation of the crystal, on its crystalline quality, and on the surface flatness. In this work, the acceleration voltage is fixed at 20 kV and the electron beam is along the MgO or STO[100] direction.

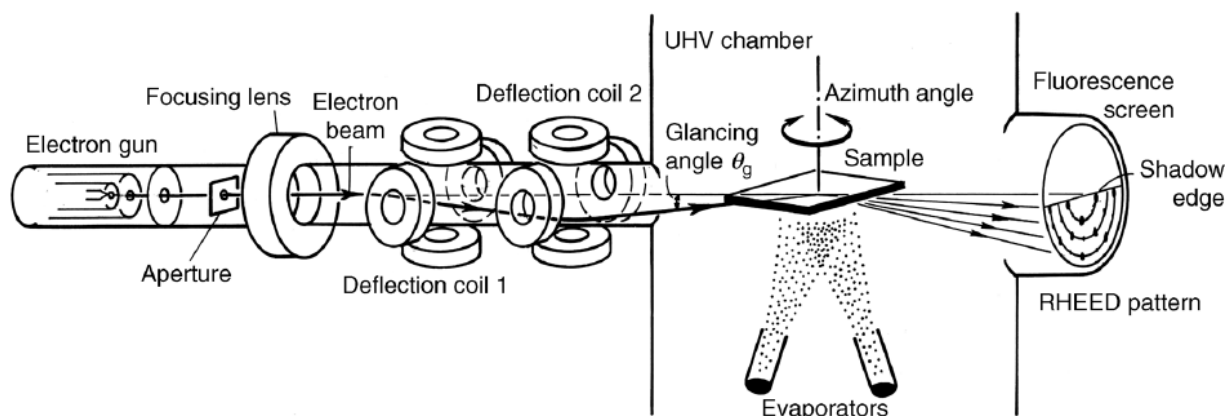
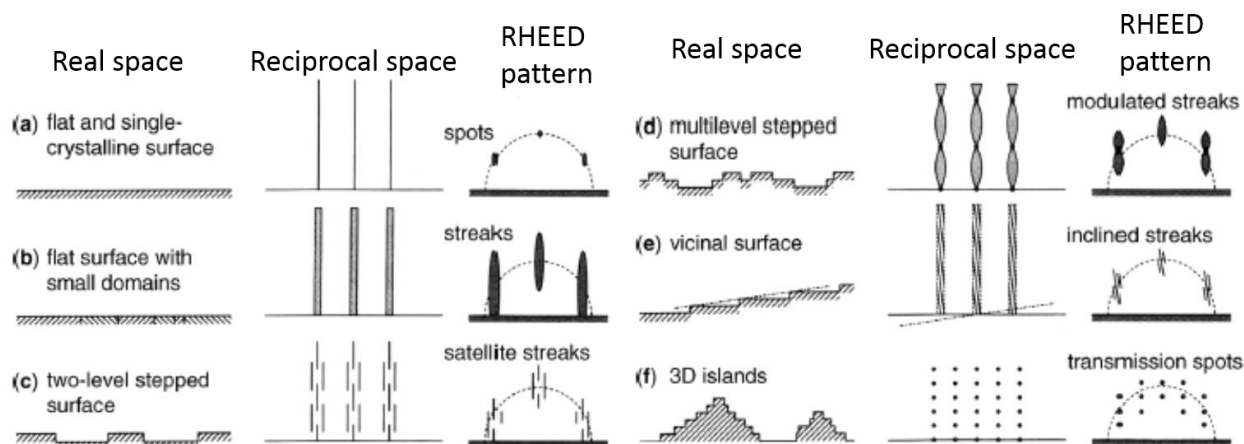
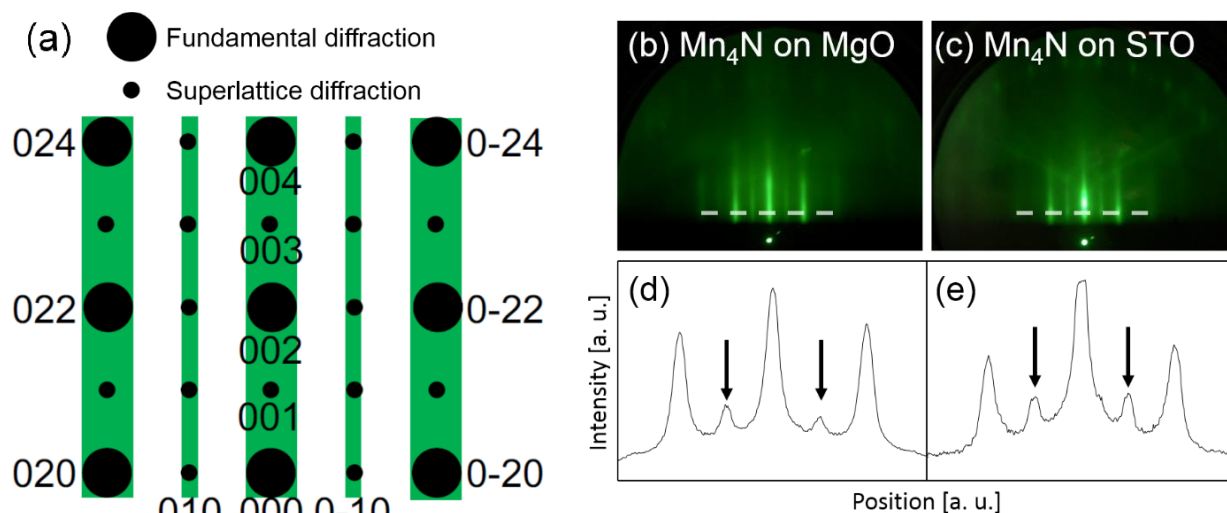


Figure 3-2: Schematic RHEED diagrams¹²²



Figures 3-3: Typical RHEED patterns for each surface state¹²²

Figures 3-4 (a) presents a simulated RHEED pattern of anti-perovskite nitrides¹⁰⁶. Note that the superlattice diffraction such as 010 is attributed to the long-range order of N atoms at the body center of fcc-Mn lattice and the degree of N-order can be evaluated qualitatively from this superlattice diffraction. Figures 3-4 (b) and (c) are the RHEED patterns of Mn₄N layers grown on MgO and STO, respectively. Both have streaky patterns, indicating a good crystalline quality, and the superlattice diffraction also appears in the spectra shown in (d) and (e), along the white dash lines.



Figures 3-4: (a) Simulated RHEED pattern of anti-perovskite nitrides¹⁰⁶. (b), (c) RHEED patterns of Mn₄N layers grown on MgO and STO. (d), (e) brightness profiles of RHEED images along the white broken lines in (c) and (d), respectively. The arrows indicate the superlattice diffractions.

[2] X-ray diffractometry (XRD)

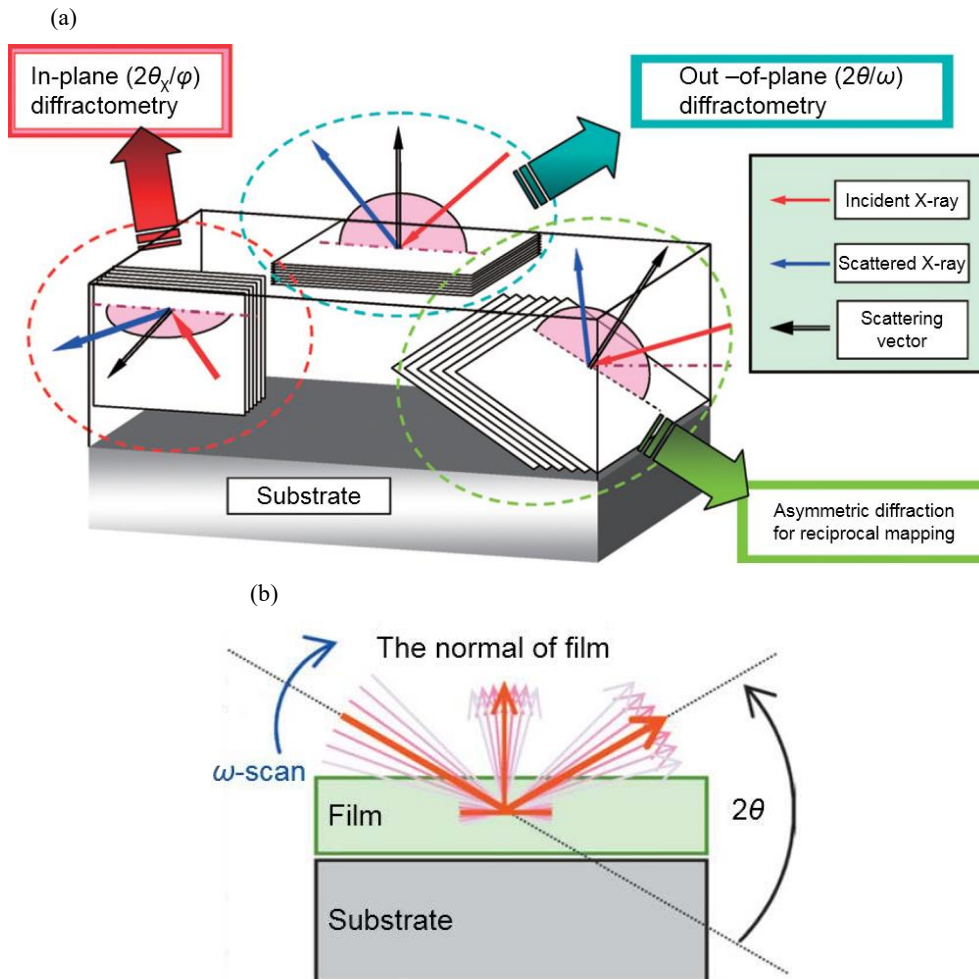
X-ray diffractometry techniques have been used to characterize our samples, using a Rigaku smart lab[®] set-up. Incident X-rays are diffracted in directions determined by Bragg's condition:

$$2d_{hkl}\sin\theta = n\lambda \tag{3-1}$$

where d_{hkl} is the distance between each (hkl) plane in the crystal, θ is the incident angle of X-ray, n is the diffraction order, and λ is the wavelength of X-ray. In this work, the n -th diffractions peak from the plane [Crystal] (hkl) is denoted [Crystal] $nh nk nl$, independently of the name of plane. For example, the second diffraction peak from the Mn₄N (001) plane is expressed as “Mn₄N 002”.

Figures 3-5 (a) shows the experimental geometry of the XRD set-up¹²³. By tuning the relative angle of the substrate with respect to the X-ray detector, we can choose an orientation axis to focus on, such as the perpendicular to plane ($2\theta/\omega$) and the in-plane ($2\theta_x/\phi$) axis. We usually chose the Mn₄N [001], [100], and [110] axis, as they are the fundamental crystalline orientations. From the series of diffraction peaks, we identify the crystal type and check the film quality.

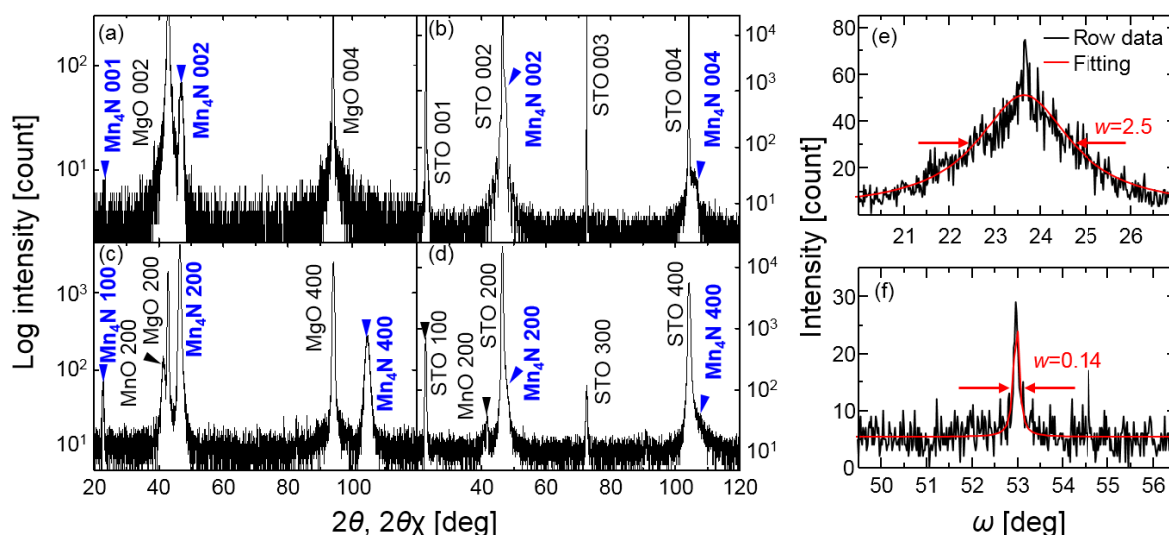
To evaluate the orientation quality of the epitaxial films, we also used ω -rocking curve measurements. Figures 3-5 (b) shows the principle of rocking curve measurement¹²⁴. By scanning the angle of sample tilting ω for a fixed diffraction angle 2θ (corresponding to a diffraction peak such as Mn₄N 002), we can qualitatively evaluate the mosaicity: distribution of the crystalline orientations.



Figures 3-5: (a) Geometry of the used X-ray diffraction techniques¹²³. (b) Principle of ω -rocking curve measurements¹²⁴.

We performed out-of-plane and in-plane diffractometry to identify the crystal species and qualify the ordering of the N atoms, ω -scan rocking curve to characterize the orientation quality perpendicularly to the layer

plane, and XRR to measure the layer thickness. Figures 3-6 presents the results of XRD for each Mn₄N/MgO and Mn₄N/STO sample. ω -scan rocking curves are shown in the same figure for (e) Mn₄N 002 on MgO, (f) Mn₄N 004 on STO. For Mn₄N/MgO, the XRD peaks of the film and of the substrate are well split, which allows extracting information on the magnetic layer. On the contrary, the diffraction peak of Mn₄N 002 is so close to STO 002 that we need to analyze the higher-order Mn₄N 004 rocking curves to separate each peak. These rocking curves have been fitted by a Lorentzian. These observations prove the epitaxial growth of the Mn₄N film. However, the widths of the rocking curves are obviously different, indicating that Mn₄N films are much better textured when deposited on STO rather than on MgO. This result is similar to what has been previously established for Fe₄N films¹⁰⁶. The superlattice reflections in the RHEED pattern, together with the 001 peak in the XRD pattern, indicate the good long-range ordering and the presence of the N atom at the body center of the fcc-Mn lattice. XRR measurements also provided the film thicknesses, of 8.8 nm for the Mn₄N/MgO sample and 9.4 nm for the Mn₄N/STO sample. Note that in-plane XRD patterns (Figures 3-6 (c) and (d)) include the peaks from oxidation phase MnO 200. We still do not know the origin of this phase, and thus have scheduled Transmission Electron Microscopy analysis to investigate the oxidized dead layers on the substrates or capping layers.



Figures 3-6: (a), (b) Out-of-plane XRD patterns. The blue marks indicate the peaks attributed to the (100)-oriented-Mn₄N. (c), (d) In-plane XRD patterns. The incidence angle is $\omega=0.4^\circ$, and the scattering vector is along [100]. (e), (f) ω -scan rocking curves for (e) Mn₄N 002 on MgO, and (f) Mn₄N 004 on STO. The black and red lines represent the raw data and the fit using a Lorentzian curve, respectively.

3.2. Magnetic and electric properties

Several magnetic and magneto-transport properties of these Mn₄N films have been measured.

3.2.1. Fundamental magnetic properties

The magnitude of the magnetization, *i.e.* the spontaneous magnetization, can be measured through the detection of the stray field emitted from the magnetic sample. We used two kinds of magnetometer, a VSM and a

SQUID. Both techniques measure the magnetic moment of the whole sample.

[1] Vibrating sample magnetometer (VSM)

VSM technique detects stray field by electromagnetic induction. Figure 3-7 presents a simple schematic of VSM¹²⁵. The sample is magnetized by a constant magnetic field coming from the magnetic poles of an electromagnet. According to Faraday’s law, the produced inductive voltage is proportional to the time-derivative of magnetic flux through a circuit. Therefore, the constant field produced by the magnetic poles does not generate any signal. To obtain a varying magnetic field, the sample vibrates at around 80 Hz. The pick-up coils surrounding the sample detect the oscillating inductive voltage due to the vibrating sample using lock-in techniques. In practice, the conversion factor from the magnetization to the voltage is calibrated with a standard sample, such as a piece of Ni.

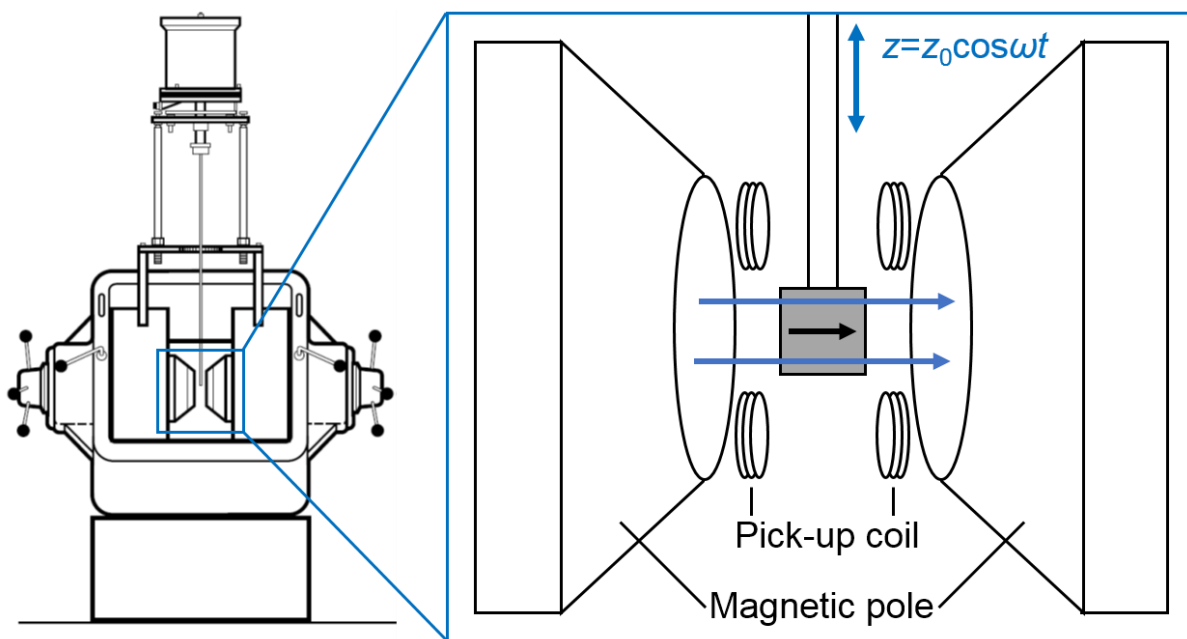


Figure 3-7: Schematic of the VSM.

[2] Superconducting quantum interference device (SQUID)

SQUID techniques utilize the Josephson effect in superconductors¹²⁶. This effect appears in superconductors /insulator/ superconductors junctions, called Josephson junctions. In 1962, Josephson predicted that not only electrons but also Cooper pairs can tunnel from one superconductor to another¹²⁷. These 2 superconductors are separated by an insulating barrier with “weak link.” For distances about 2 nm, shorter than the coherence length of the superconductors, and currents under a critical current I_c that depends on the weak link, the Cooper pairs can tunnel through the insulating barrier without any voltage drop. This current is called as Josephson current, and it is sensitive to the magnetic flux penetrating a circuit containing one or more Josephson junction. This ring device of Figure 3-8 with two Josephson junctions is called SQUID, and can be used to sense small magnetic fields. With bias current I_b slightly stronger than I_c , a voltage drop depending on the current in the loop I_{loop} can be detected. Then, if a magnetic field penetrates the SQUID ring, a screening current due to the

Meissner effect tries to cancel the magnetic flux, and $I_{loop} (= \Phi_{loop}/L_{loop})$ changes, enabling to measure the strength of the magnetic field. In contrast to VSM, SQUID can measure the magnetic flux itself, not its time-derivative, and does not need oscillating samples.

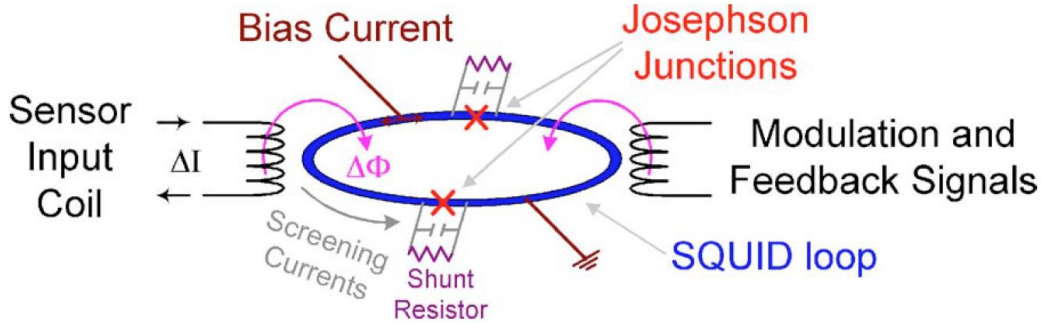


Figure 3-8: Josephson junction and SQUID principle.¹²⁶

During my Ph. D, we used a Quantum Design Magnetic Properties Measurement System (MPMS®) 3¹²⁸, equipped with SQUID and VSM options. The maximum magnetic field is 7 T, and the sensitivity to the magnetic flux is 8×10^{-11} A.m² for the VSM and 6×10^{-10} A.m² for the SQUID at 7 T. The samples have been cut into 4×4 mm² pieces, and inserted in straws to perform the measurement. The surface areas of samples are measured using an optical microscope.

Figure 3-9 presents the out-of-plane and in-plane magnetization curves, obtained by MPMS up to 4 and 6 T of the (a) Mn₄N/MgO and of the (b) Mn₄N/STO samples. From the out-of-plane hysteresis curves, the M_S of Mn₄N/MgO and Mn₄N/STO can be estimated to be 119 and 103 kA/m, respectively, in good agreement with previous results¹²⁹. From the in-plane loop of the Mn₄N/STO sample, its anisotropy field H_K can be estimated to be 4 T. The uniaxial anisotropy K_u was calculated to be 1.1×10^5 J/m³ for both samples, using the integration of the area enclosed between the in-plane and out-of-plane magnetization curves, and taking into account the demagnetization field energy.

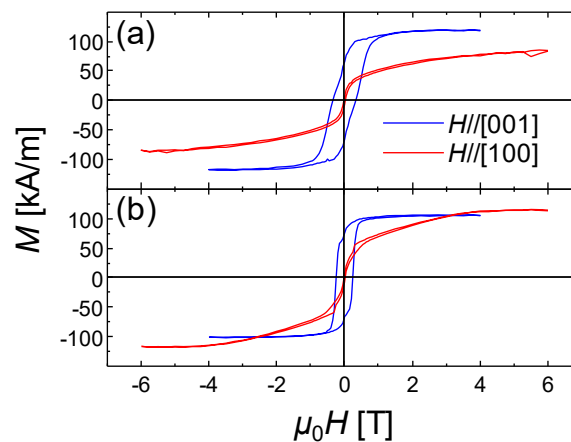
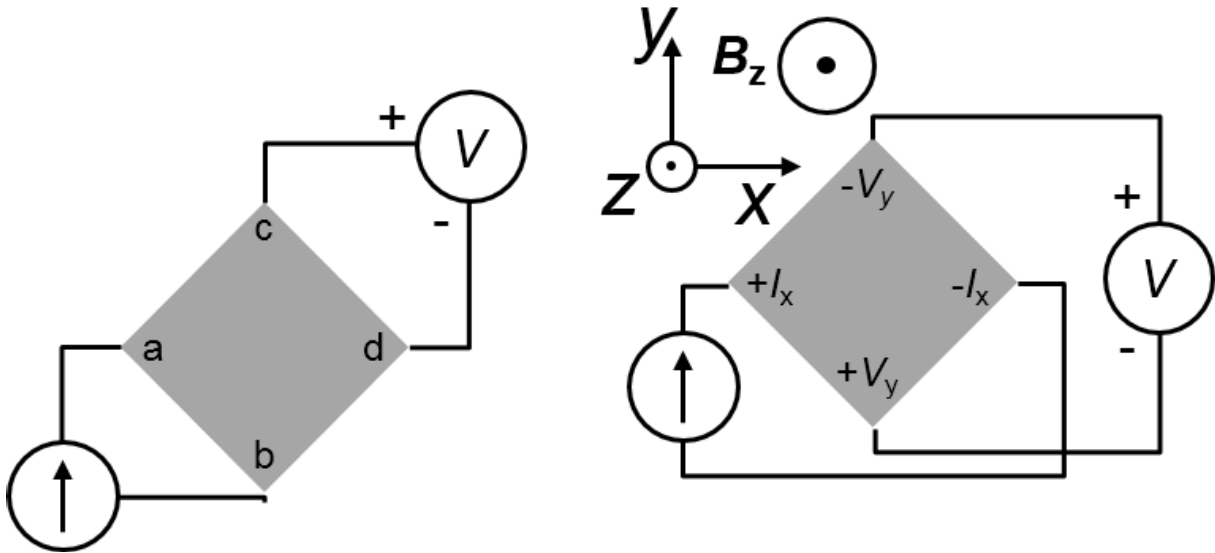


Figure 3-9: Magnetization curves the (a) Mn₄N/MgO and (b) Mn₄N/STO samples. The blue and red lines correspond to out-of-plane and in-plane magnetic field measurements by VSM-SQUID, respectively.

3.2.2. Magneto-transport properties

The magneto-transport properties of our sample, *i.e.*, their electric properties under external magnetic field, have been measured using both a helium-free cryostat equipped with electrical contacts, and placed in-between the poles of an electromagnet, and a Quantum Design Physical Properties Measurement System (PPMS[®]). The former set-up can apply magnetic fields up to 1.4 T and reach 10 K. Electric measurements can be done using DC or lock-in techniques, and the measurement set-up can be customized, for instance to realize pulses injection, gate voltage application, 2nd harmonic voltage detection. The latter set-up is a commercial one. The range of field is ± 9 T, enough to saturate the magnetization of our Mn₄N samples in-plane, with temperatures ranging from 0.4 to 350 K. It is also able to rotate samples in the chamber, to measure both the out-of-plane and in-plane magneto-transport properties, or angular dependences that can for instance be useful for AMR measurements¹³⁰.

In this work, we mainly focused on anomalous Hall effect (AHE) measurements to detect the magnetization switching more precisely than with the VSM. Both the resistivity and hall coefficients have been measured using a van der Pauw method^{131,132}. The 4 corners of the samples have been connected using wire bonding, as shown in Figures 3-10. It allows measuring the resistivity and Hall coefficients of a uniform and continuous layer without requiring the patterning into Hall bars.



Figures 3-10: Measurement circuit used in the van der Pauw method. The left one is used for resistivity measurements and the right one for Hall measurements. The chirality of I-V-B is defined like ordinary Hall measurement, so that positive carriers generate positive ordinary Hall voltage.

To obtain the resistivity, a current is injected from point **a** to **b** in Figures 3-10, while the voltage is measured between **c** and **d**. The ratio of the voltage V_{cd} and the current I_{ab} is defined as $R_{ab,cd} = V_{cd}/I_{ab}$. The other contacts combination $R_{ac,bd}$, is also measured, to take into account eventual asymmetries. The relationship between

$R_{ab,cd}$, $R_{ac,bd}$ and the resistivity ρ_{xx} is given by,

$$\exp\left(-\frac{\pi t}{\rho_{xx}} R_{ab,cd}\right) + \exp\left(-\frac{\pi t}{\rho_{xx}} R_{ac,bd}\right) = 1 \quad (3-2)$$

where t is the thickness of film. As it is usually impossible to solve this equation analytically, we computed the approximated root using the “Newton-Raphson method¹³³” in a Python program of our own making.

The circuit schematic for Hall measurements is shown in the right part of Figures 3-10. The transverse voltage V_y in ferromagnet (or a ferrimagnet) depends mainly on the Hall effect, the anomalous Hall effect and the Planar Hall effect. Under a magnetic field B_z , this transverse voltage can be given by^{134,135,136},

$$V_y = \left(R_0 + R_H \frac{B_z}{t} + \rho_{AH} \frac{\cos\theta}{t} + \frac{\rho_{//} - \rho_{\perp}}{t} \sin^2\theta \sin\phi \cos\phi \right) I_x \quad (3-3)$$

where R_0 , R_H , ρ_{AH} , $\rho_{//}$, ρ_{\perp} , θ and ϕ are a longitudinal resistive offset, the ordinary Hall coefficient, the anomalous Hall resistivity, the resistivity for a magnetization parallel and perpendicular to the current, and the elevation and azimuth angles of the magnetization (*cf.* Figure 3-11), respectively. As actual samples are not perfectly squared, V_y usually contains a resistive contribution (R_0), which can very slightly depend on the magnetic field (but which is even in field, whereas Hall effects are odds in field). The second term of the equation, proportional to the magnetic field, is the ordinary Hall component, but in metals such as Mn₄N, R_H should be very small because of the high carrier density. This component does not saturate at high fields, and can be subtracted from the signal using fits at high fields. The third contribution is the AHE voltage, it is proportional to magnetization, but not to the magnetic field. The fourth term corresponds to planar Hall effect, and has the same origin as the AMR effect, which is a dependence of the resistivity with the angle between the applied current and the magnetization. In this work, the AMR ratio of Mn₄N is smaller than 0.1% at room temperature¹¹⁷, so that this term can be neglected.

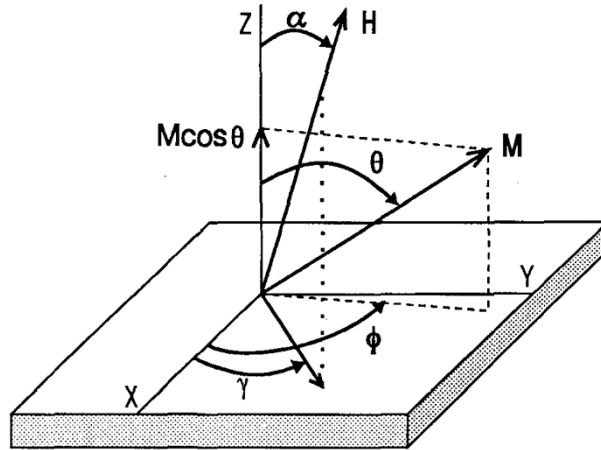


Figure 3-11: Cylindrical coordinates used to describe the magnetization direction¹³⁵

The origins of AHE are the same as those of SHE: skew-scattering^{137,138}, side-jump¹³⁹, and intrinsic deflection due to Berry’s phase curvature^{140,141}. Spins up and down are deflected in opposite directions. In a nonmagnetic metal such as Pt¹⁴², this generates a pure spin current perpendicular to both the applied current and the magnetization. In ferromagnets or ferrimagnets, the current is spin-polarized, and thus the same effect generates a spin polarized current, once again perpendicular to the applied current and magnetization.

The magnitude of the AHE is given by the anomalous Hall resistivity ρ_{AH} defined in eq. (3-3), the anomalous Hall angle θ_{AH} , and the anomalous Hall conductivity σ_{AH} are given by,

$$\theta_{AH} = \frac{\rho_{AH}}{\rho_{xx}}, \sigma_{AH} = \frac{\rho_{AH}}{\rho_{xx}^2 + \rho_{AH}^2} \quad (3-4)$$

θ_{AH} is useful to evaluate the conversion ratio from longitudinal voltage (current) into transverse voltage (current). On the other hand, σ_{AH} is valuable to classify the origin of the AHR in terms of theory by comparing that temperature dependence with one of longitudinal conductivity σ_{xx} ¹⁴³. For instance: (i) a high conductivity regime where skew scattering dominates AHE causing linear σ_{AH} to σ_{xx} , (ii) a scattering-independent or intrinsic regime where σ_{AH} is independent of σ_{xx} , (iii) a bad metal regime where σ_{AH} drops with σ_{xx} faster than linearly at high temperature.

Let us present now the experimental results of the transport measurements. The resistivities extracted from the van der Pauw measurements at room temperature are 187 $\mu\Omega\cdot\text{cm}$ for Mn₄N/MgO and 181 $\mu\Omega\cdot\text{cm}$ for Mn₄N/STO. Figure 3-12 shows the hysteresis loops measured by AHE. The AHE angle θ_{AH} is high and negative (-2%), in line with previous reports on Mn₄N^{114,117}. While the Mn₄N/MgO sample shows a smooth hysteresis loop, the magnetization of the Mn₄N/STO sample switches very sharply, with a full remanence at zero field. Despite these differences, it is striking that the spontaneous magnetization and all the transport quantities of the two systems are very similar, which indicates that the materials are intrinsically alike. The structural characterizations suggest however that the structural disorder, *i.e.*, the nature and density of crystalline defects, are different, and thus that the increased disorder is responsible for the higher coercivity and slanted loop of Mn₄N/MgO samples.

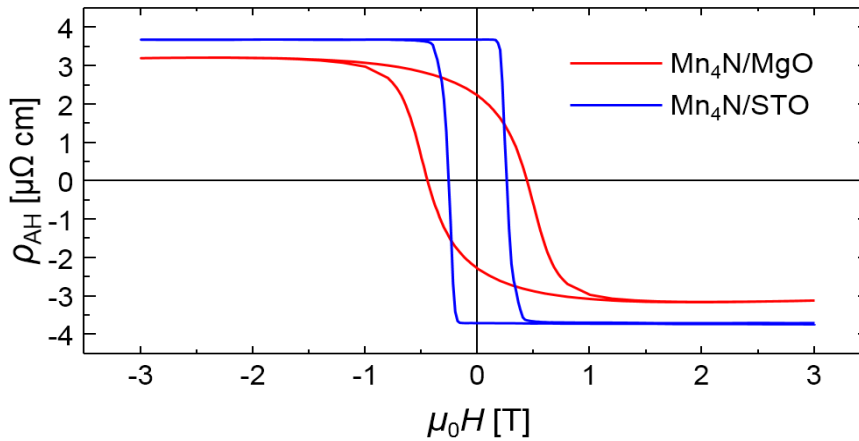


Figure 3-12: Anomalous Hall effect hysteresis loops of the (red) Mn₄N/MgO and (blue) Mn₄N/STO samples.

In-plane magnetization properties have also been evaluated by magneto-transport measurement by applying in-plane magnetic field (defined as y -axis)^{144,145,146}. Figure 3-13 is the illustration of the experimental geometry. Since the anomalous Hall voltage ΔV_y is proportional to the vertical component of magnetization ($M_z = M_S \cos\theta$), the in-plane component of magnetization (M_y) is derived as,

$$\frac{M_z(H)}{M_S} = \frac{\Delta V_y(H)}{\Delta V_{AH}} \quad (3-5)$$

$$M_y(H) = M_S \sqrt{1 - \left(\frac{M_z(H)}{M_S}\right)^2} \quad (3-6)$$

where ΔV_y is the transverse voltage to the current without the resistive offset for each H, ΔV_{AH} is the total amplitude of the anomalous Hall voltage. The magnetization is always kept perpendicular to the current (I_x) in order to eliminate an AMR contribution. From the area enclosed by out-of-plane and in-plane M - H loops, magnetic anisotropy constant K_u can be derived by,

$$K_u = \frac{\mu_0 M_S^2}{2} + \mu_0 \int_0^{M_S} (H_y dM_y - H_z dM_z) \quad (3-7)$$

where the first term is the demagnetizing energy, the second one is the effective anisotropy. This method is applicable for especially ultrathin films with small M_S , which is hard to detect through its stray field by VSM or SQUID measurements. Moreover, this in-plane AHE measurement technique does not include the contribution of substrate such as paramagnetism or diamagnetism and its signal is in inverse proportion to the thickness as given by eq. (3-3) for a constant current.

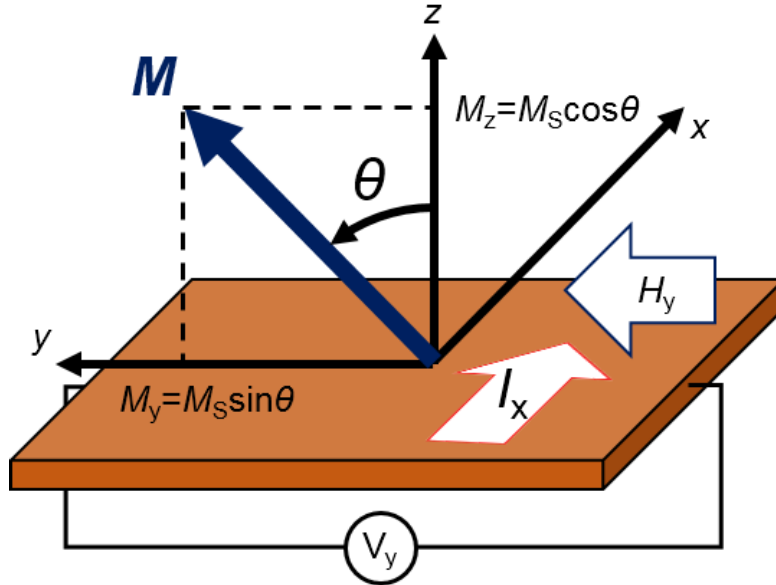
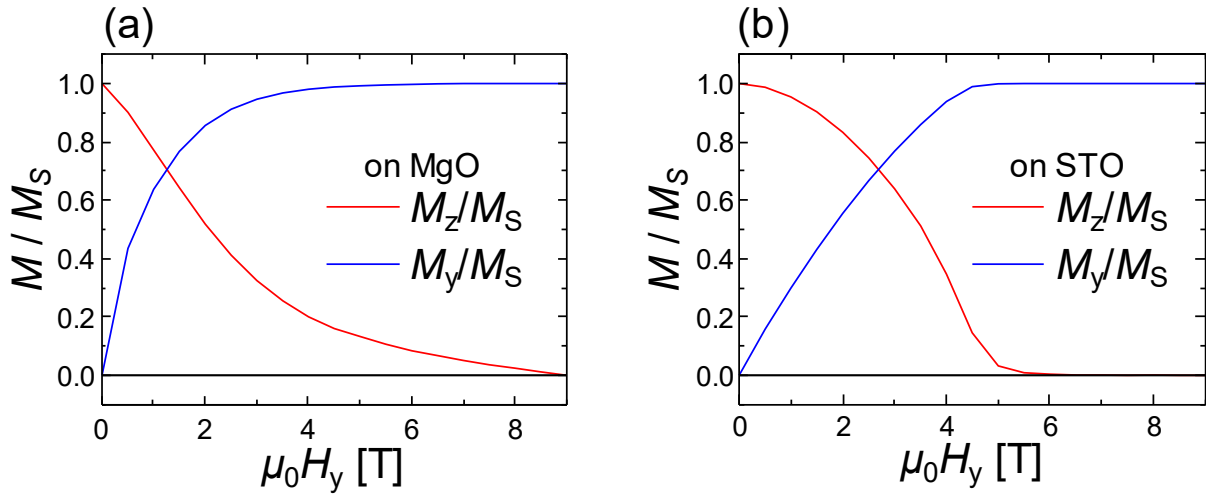


Figure 3-13: The geometry of the in-plane AHE measurement.

Figures 3-14 present hysteresis loops of Mn₄N films grown on MgO and STO. The red lines denote the out-of-plane component of magnetization ratio given by eq. (3-5), and the blue lines are the in-plane components derived from eq. (3-6). While M_y on MgO rises with relatively small field indicating weak anisotropy, that on STO linearly increases with the field resulting in anisotropic field $H_K = 4.5$ T. The magnetic anisotropy energy K_u has been calculated according to eq. (3-7), resulting in 0.12 MJ/m³ for MgO and 0.20 MJ/m³ for STO, respectively. While the results of magnetization measurement in MPMS gives similar results to each substrate, magneto-transport based analysis revealed obvious difference between two substrates from the viewpoint of magnetic anisotropy. This difference can be attributed to the different degree of orientation observed by ω -rocking curve measurements.



Figures 3-14: In-plane hysteresis loops of Mn₄N on (a) MgO and (b) STO substrates.

3.3. Magnetic domain structure

The magnetic domain structure can be observed using several methods. The most used are probably magneto-optical methods, based on the Faraday effect in transmission or on the Kerr effect in reflection, X-ray magnetic circular dichroism with photo-emission electron microscopy and transmission microscopy, Magnetic Force Microscopy (MFM), and electron microscopy method such as Lorentz microscopy or scanning electron microscopy with polarization analysis. In this work, we used both Kerr microscopy and MFM.

3.3.1. Magneto-optical Kerr effect (MOKE) imaging

The MOKE has been discovered by Kerr in 1877¹⁴⁷. The linearly polarized incident light reflected on a magnetic surface is transformed into an elliptically polarized light. The magnitude and sign of the Kerr rotation (*i.e.*, the rotation of the light polarization) depends on the magnetization direction of the film¹⁴⁸. This enables to detect changes of the magnetization direction, and thus the hysteresis loop or the 2D-domain configuration using optical microscopy techniques. Depending on the relative direction of the magnetization with respect to the incident light, we can distinguish 3 types of configuration, shown in Figure 3-15. The polar MOKE is usually used for PMA films, and longitudinal and transverse MOKE for films with in-plane magnetization. The resolution of this microscope is limited by the light wavelength (630 nm in our equipment) and has been estimated to be around 500 nm. Using different objectives, the field of view can be changed from several millimeters down to around 100 μm . It can then be used to observe large magnetic domains, but also to observe smaller structures like the strips that were used to measure domain wall speeds.

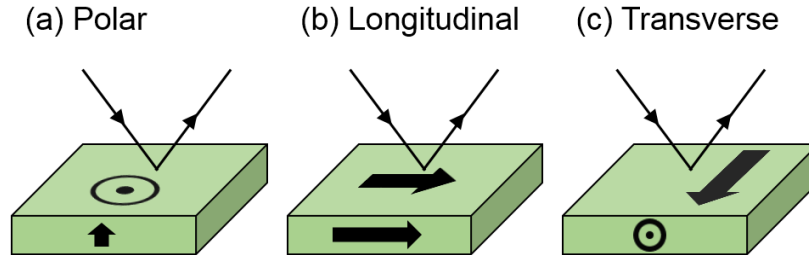


Figure 3-15: 3 types of MOKE configuration.

3.3.2. Magnetic force microscopy (MFM)

By using atomic force microscopy (AFM) tips coated by a magnetic thin film, we can detect magnetic signal from the surface of samples and obtain magnetic domain configuration with higher spatial resolution than MOKE microscopy. Figure 3-16 shows the operation principle of MFM¹⁴⁹. MFM is a kind of scanning probe microscope, which scan the sample surface by the probe and detect several signals. AFM works according to atomic force, which has quite short working range, giving the topographic image of the surface. In other words, atomic force modulates the harmonic frequency of cantilever monitored by laser reflection by a photodiode, tune the height with keeping constant frequency, and output the height data. The magnetic force has longer interaction length than atomic force. Thus, by lifting the tip up from the surface and keeping the height, we can reduce the AFM signal and extract the magnetic signal from the sample surface. Magnetic force also modulate the harmonic frequency of the tip and we can detect the phase change $\Delta\phi$ of oscillation, given by $\Delta\phi = \frac{Q}{k} \frac{\partial F_z}{\partial z}$, where k , Q , z and F_z are the spring constant, quality factor, height of the tip, and acting force. From the 2D-mapped phase change distribution, we can estimate the domain structure in magnetic layers. Actual MFM images are completely different between PMA and IMA film because the MFM tip detect the magnetic force caused by the stray field arising from the magnetitic configuration of the sample. Now I focus on perpendicularly magnetized films such as Mn₄N. Figure 3-17 presents the schematic of stray field from a perpendicularly magnetized thin film with simplified MFM signal. The film with PMA emits a stray field anywhere and enables to observe the magnetization orientation directly. In the MFM image, there are 2 kinds of magnetic signals called monopolar and bipolar contributions¹⁵⁰. Depending on the sign of magnetic charge in the domain, the MFM contrast varies from bright to dark, called monopolar contribution, due to the surface magnetic charges given by $H = \mathbf{M} \cdot \mathbf{n}$, where \mathbf{n} is a normal vector of the surface. However, perpendicularly magnetized infinite plane emits only uniform stray field without any spatial change in gradient $\frac{dH_z}{dz}$, which make only a coupled force to rotate magnetic moment. Therefore, much larger domains than an MFM tip give only a small magnetic signal in MFM images. On the other hand, at the vicinity of a DW, the stray field forms a flux loop to minimize magneto-static energy with large local change of the gradient of H_z providing a couple of bright and dark contrast, called dipolar contribution. The contrast of MFM images is determined by the combination of these contributions. However, in any case, it is much easier to estimate the domain structure in perpendicularly magnetized films than in-plane magnetized film because they have only 1 easy axis and we only must distinguish the sign of magnetic signal. On the other hand, in-plane magnetized films have 2-dimensional freedom of magnetization direction though MFM tells us only the information about out-of-plane component of the stray field. Therefore, it is necessary for in-plane magnetized

films to compare the MFM image with the result of micromagnetic simulation to estimate detailed in-plane domain structure. MFM has much higher spatial resolution than MOKE imaging thanks to the freedom from wavelength of light limitation. However, it takes much longer time to scan one area than MOKE microscopy, which responds immediately. Thus, for time-resolved or temporally-differential measurement such as DW motion, MOKE is more convenient.

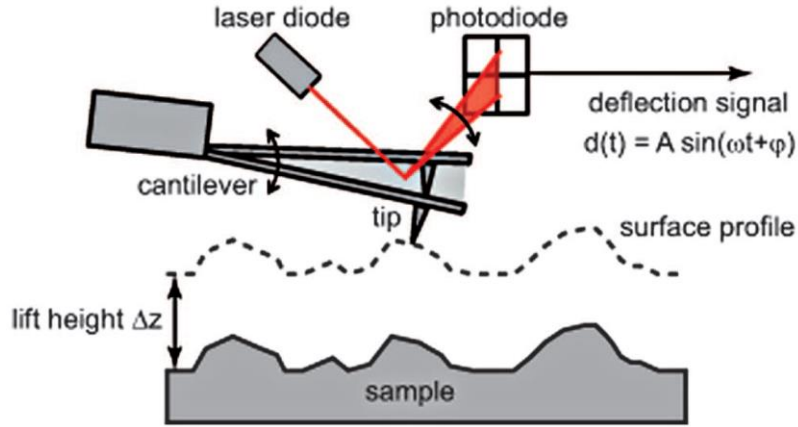


Figure 3-16: Schematic of the MFM set-up and operation principle.¹⁴⁹

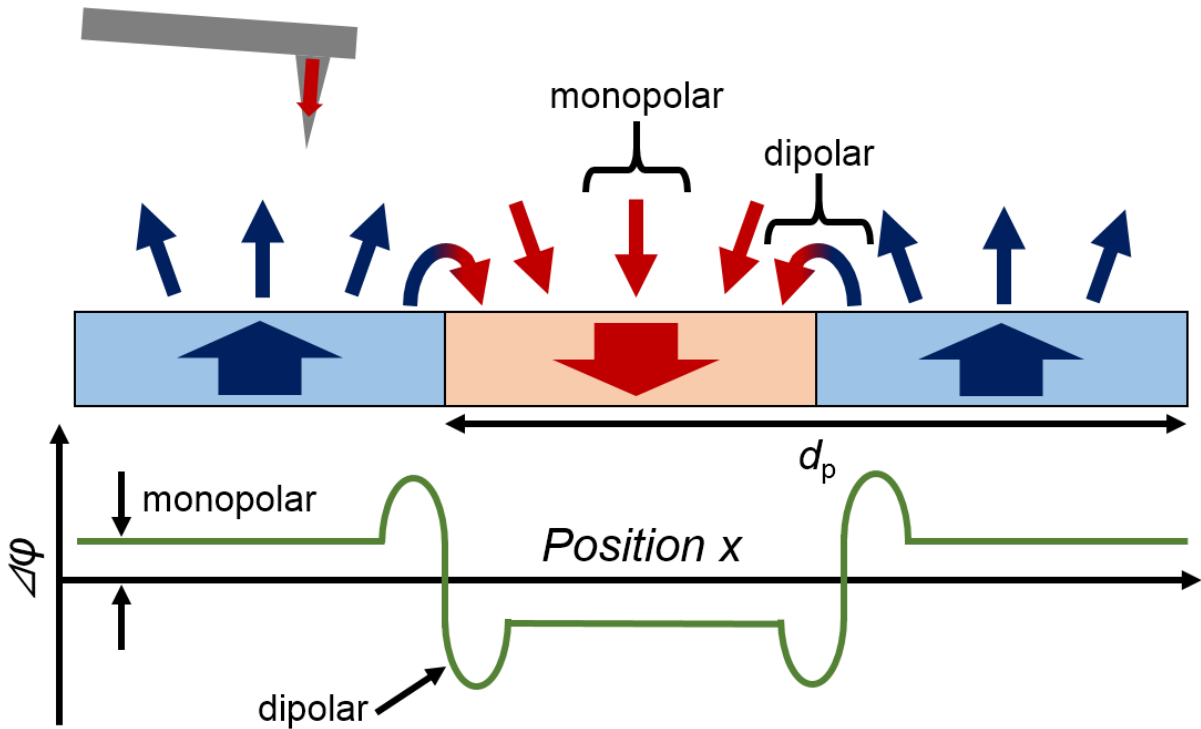


Figure 3-17: Stray field from PMA film and contribution to the MFM signal.

3.3.3. Equilibrium domain size

Let us discuss the equilibrium magnetic domain configuration in Mn₄N thin films. The theoretical equilibrium domain size results from the balance between the demagnetization energy and the DW energy $\sqrt{AK_u}$,

where A is an exchange stiffness. In ref. [71], a theoretical calculation assuming a periodic stripe domain structure concluded that the equilibrium domain size divided by the layer thickness D/t is given by,

$$\ln\left(\frac{D}{t}\right) \approx \frac{\pi D_0}{2t} + \ln(t) - 1 + \mu\left(\frac{1}{2} - \ln(2)\right), D_0 = \frac{2\sqrt{AK_u}}{\mu_0 M_S^2}, \mu = 1 + \frac{\mu_0 M_S^2}{2K_u} \quad (3-8)$$

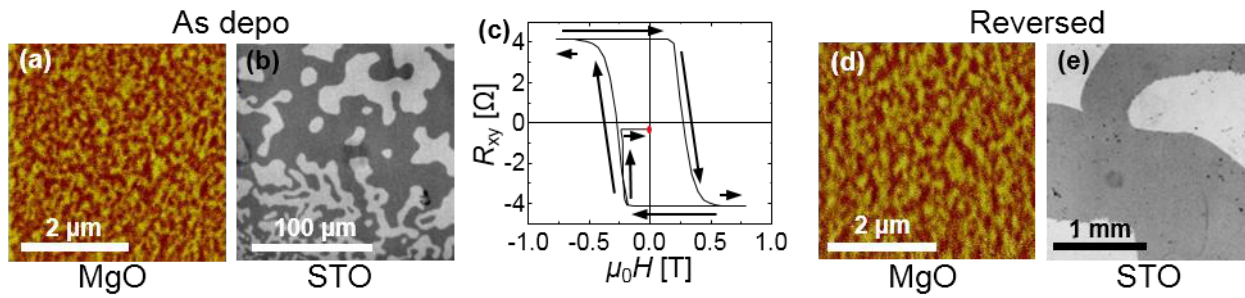
where D_0 is called the “dipolar length,” the ratio of the DW energy and of demagnetizing energy term $\frac{\mu_0}{2} M_S^2$, and μ denotes the ratio of this demagnetizing energy term and of the anisotropy energy.

Using the actual parameters of Mn₄N thin films ($M_S=105$ kA/m, $K_u=110$ kJ/m³, $t=9.4$ nm, and $A=15$ pJ/m using a rough estimation from the Curie temperature¹⁵⁰), we can calculate some fundamental parameters concerning domain structure. The DW width is $\pi\sqrt{\frac{A}{K_u}}=37$ nm, the DW energy is $\sqrt{AK_u}=1.3$ mJ/m², $D_0=0.19$ μm , and $\mu=1.06$. The resulting equilibrium domain size for this Mn₄N film is 2.5×10^5 m, much larger than the size of substrate. This indicates that the demagnetizing energy is negligible with respect to the DW energy, because of the small M_S and high K_u , and that in practice the domain size and shape should be rather determined by DW pinning on extrinsic defects¹⁵¹. Note that this domain size function is quite sensitive to the magnetization and to the thickness. For example, if we use $M_S=95$ kA/m instead of 105 or $t=8.4$ nm instead of 9.4, D varies to 2.4×10^8 m and 9.1×10^6 m, respectively. In any case, Mn₄N thin films are expected to have infinite-like giant domains, corresponding to full remanence magnetization at zero field in nature.

3.4. The influence of substrates

Figures 3-18 show the result of domain observations of (a) Mn₄N/MgO and (b) Mn₄N/STO as-deposited samples, before applying any magnetic field. This state is often considered to be relatively close to the equilibrium state. For each kind of sample, the magnetic domain configuration has been observed by MFM or MOKE microscopy, depending on the typical length scale found for the magnetic domains. The mean domain period d_p , shown in Figure 3-17, has been estimated using a 2D fast Fourier transformation method¹⁵². In Mn₄N/MgO samples, the magnetic domains are small ($d_p=0.28$ μm), far below the theoretical equilibrium width. The irregular shape of the DWs is probably characteristic of a strong disorder¹⁵¹, the DWs being pinned at the beginning of the growth. On the contrary, the magnetic domain size in the Mn₄N/STO sample is two orders of magnitude larger: although it remains smaller than the theoretical equilibrium domain width, d_p is as large as 20 μm , with smooth magnetic DWs. This seems to indicate that there is a much lower influence of the extrinsic disorder in the Mn₄N/STO sample. The domain width value is comparable with that of ultrathin CoFeB(1.1 nm)/MgO(1) and Pt(2.4)/Co(0.27) systems, with d_p values of respectively 14 and 6.5 μm obtained after thermal demagnetization^{152,153}.

Figures 3-18 (c) shows the Hall signal of a Mn₄N/STO sample during a typical partial reversal process. Figures 3-18 (d) and (e) present the domain configurations of both samples in such partially reversed states. In the case of Mn₄N/MgO, the structure of the domains is almost the same as in the as-deposited state, while the domain structure in Mn₄N/STO evolved from a micron-sized configuration to a millimeter-sized one, a value never reported, to our knowledge, in any perpendicularly magnetized thin films. MOKE images show the presence of very few nucleation centers, showing that the magnetization switching occurs by a nucleation followed by an easy propagation. Note that this observation is consistent with the fact that the hysteresis loop is square.



Figures 3-18: (a) MFM and (b) MOKE images of as-deposited Mn₄N layer grown on MgO and STO. (c) Hall resistance during partial reversal process for Mn₄N/STO used for (e). (d) MFM and (e) MOKE images after partial reversal process of Mn₄N on MgO and STO.

The differences between the two systems are striking, concerning both their hysteresis loops, and their domain shapes and sizes. The XRD data and the magnetic properties suggest that these differences arise from the crystalline quality of the samples, which is higher for the Mn₄N/STO samples. The physical origin could arise from the difference in the strain relaxation process: there is a large lattice misfit $f = (a_{\text{film}} - a_{\text{sub}})/a_{\text{sub}}$ at the Mn₄N/MgO interface (-7.6%), whereas the misfit at the Mn₄N/STO interface is only -0.4% . While the existence of misfit dislocations at Mn₄N/MgO interface has already been observed by transmission electron microscopy¹¹⁴, other strain-relaxation through-dislocations of micro-grain boundaries are also expected to play a major role in the magnetic behavior. This underlines that the selection of a well-matching substrate is crucial to improve the magnetic properties of Mn₄N layers, and notably its suitability for current-induced DW propagation.

3.5. Summary

In this chapter, I showed that the magnetic properties of Mn₄N thin films are drastically improved by replacing conventional MgO substrates by STO substrates. This Mn₄N/STO system exhibits astonishing properties: a giant magnetic domain structure, at the millimeter length scale, with full remanence, scarce nucleation and a sharp magnetization switching. Therefore, we will focus in the following only on the Mn₄N/STO system. These properties, associated to a very small M_s and a large PMA, is appealing for spintronic applications. The next chapter will present CIDWM experiments confirming this potential.

Chapter 4 Spin-transfer torque using direct current

As stated in chapter 2, the magnitude of the STT, is inversely proportional to the magnetization. Thus, Mn_4N thin films should have a large STT efficiency, thanks to their small M_S (~ 100 kA/m). However, there are only few reports about magneto-transport properties in Mn_4N ^{114,117,154}, without any study of spin-transfer properties. The aim of the next two chapters is to give light on the potential of Mn_4N thin films by evaluating the efficiency of STT-based phenomena. Two kind of STT experiments have been performed, to study the effect of STTs on DWs. In this chapter, we will focus on experiments using direct currents (DC), the next chapter focusing on the use of electric pulses. After describing the nanofabrication process, we will establish the field-current equivalency in this material. We will show CIDWM experiments by DC current without external fields

4.1. Nanofabrication process

To characterize CIDWM phenomena, it is necessary to fabricate micronic or sub-micronic devices, to restrict the number of domains in the system so that one can study a single DW. In this section, we will present the typical nanofabrication process of our magnetic thin films, used to pattern them into devices such as microstrips.

4.1.1. Electron-beam (EB) lithography

EB lithography is one of the most important nanofabrication techniques, providing micro or nanoscale masks. First, PMMA, a positive resist is coated on the sample, using spin-coating at 3000 rpm for 60 s at room temperature, followed by post baking at 100 °C for 1 minute. The EB insolation is done using a Jeol 6300FS e-beam nano-writer, working at acceleration voltage of 100 keV. A resist which becomes soluble (insoluble) after exposure is called positive (negative) resist. After development, the residual resist patterns can be used as masks during an etching process, or can be removed in a lift-off process to transcribe the patterns into a solid mask.

4.1.2. Ion beam etching

Contrarily to semiconductors such as Si, 3d transition metals have few volatile chemical products like chlorides, fluoride, etc. Therefore, it is quite difficult to use reactive-ion etching on magnetic films and often preferable to employ a physical etching process which is called ion beam etching (IBE) or ion milling. An excited Ar^+ plasma in the IBE chamber is accelerated by a bias voltage towards the sample, thus removing atoms from the surface. Though the IBE rate depends on the sample, most materials can be etched in principle. One of the weak points of IBE is the redeposition of sputtered materials. By contrast with chemical etching, the sputtered atoms are not volatile, and can be redeposited on the side wall of the device structure. They often form tall walls at the edge of the fabricated structure, after the removal of the etching mask, which prevent surface observation such as MFM measurements. Therefore, the used IBE machine is equipped with a mechanism to tilt and rotate the substrate during the etching, which enable to etch these walls. In addition, the IBE machine used in this work also has end point detector, a secondary ion mass spectrometry (SIMS) analyzer to detect the etched elements. This equipment allows avoiding overetching, which can cause side redeposition and substrate damage.

4.1.3. Detailed steps for nanofabrication

Figure 4-1 presents a flow chart of the nanofabrication process used in this work. Polymethyl methacrylate (PMMA) was coated on Mn_4N as EB-positive resist, followed by EB lithography process to draw microstrip patterns. After development, an Al layer was deposited on the sample and lifted-off to form mask patterns. Ar IBE was then performed with SIMS analysis and substrate rotation at 70° -incident angle of ion-beam. The end point of the etching process was detected using the appearance in the SIMS signal of the presence of Sr atoms, and checked by an *ex situ* sheet resistance measurement by multimeter. After the etching process, the Al mask was removed by wet etching in a tetramethylammonium hydroxide (TMAH) solution, which does not react with Mn_4N .

Figures 4-2 (a) presents the schematic design of the Hall bar pattern used in this chapter, (b) is a scanning electron microscopy (SEM) image of Al mask after lift-off and before IBE process, and (c) is the optical microscope image after all fabrication process. The Mn_4N film was processed into 0.5 or 1 μm wide microstrips, which have a domain nucleation pad to control the nucleation of a reversed domain, and thus the direction of the DW motion. Three Hall crosses are used to detect the magnetization state by AHE, and one notch (50% of the wire width) has been patterned to pin the DW.

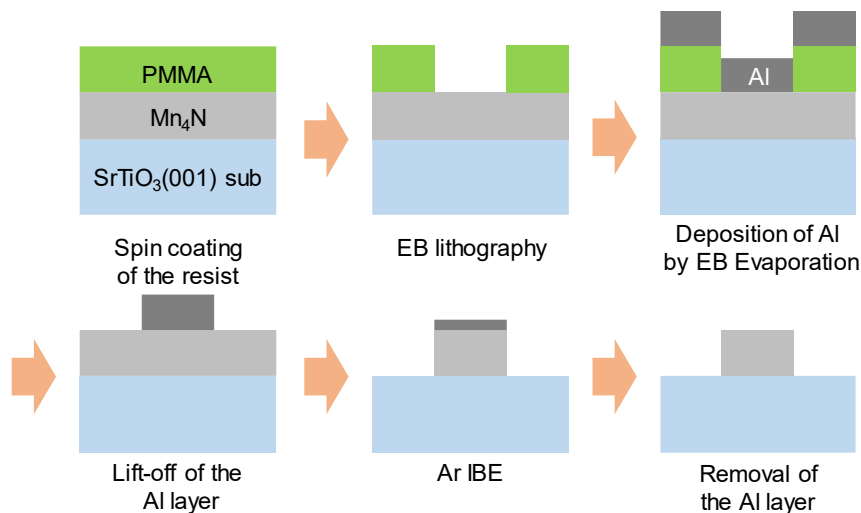
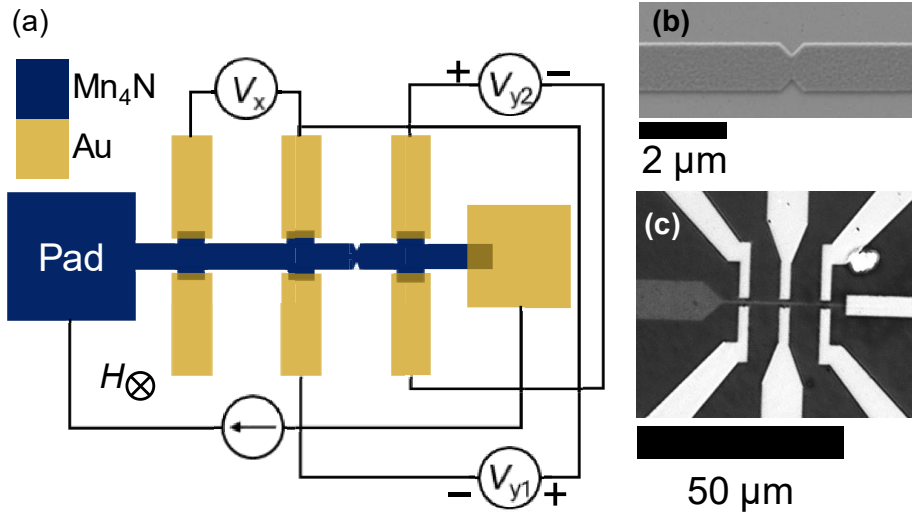


Figure 4-1: Fabrication process of Mn_4N into microstrips.



Figures 4-2: (a) Measurement geometry and Hall bar pattern consisting of a nucleation pad, 3 Hall crosses with Au electrodes and 1 notch to pin DW between 2 crosses. (b) SEM image of Al mask around the notch of 1- μm -wide strip after lift-off process. (c) Optical microscope image of the Hall bar.

4.2. Equivalency between current and magnetic field

The first attempt to observe STTs in Mn_4N samples has been done by measuring DW coercivity variations for various DCs. An oscillating current is added to the DC bias, so that the current injected in the microstrip can be expressed as $I = I_{\text{DC}} + I_{\text{AC}}\sin(\omega t)$. The AC current is a probing current, allowing to detect the AHE using lock-in techniques. Its amplitude (around 10 μA) is thus negligible with respect to the high DC used to create the STT. The left and central Hall crosses are used for 4-probe resistivity measurement. The central and right crosses are independently used for each Hall measurement, which are surrounding a notch to trap DW.

Figure 4-3 show the temperature dependence of the resistivity (a), and the dependence of the resistivity at room temperature with the applied current density j_{DC} (b). At 10 K, ρ reaches 15% of its value at RT, in agreement with previous reports on MgO substrate¹¹⁴. At temperatures higher than room temperature, the resistivity varies roughly linearly with T, with a slope of 0.34 $\mu\Omega\cdot\text{cm}/\text{K}$. The dependence of ρ with the current density shows an increase of the resistivity up to 220 $\mu\Omega\cdot\text{cm}$ for the highest current density (2×10^{11} A/m^2), which roughly corresponds to a temperature increase of 191 K. Note that the Néel temperature T_{N} is around 745 K¹⁰⁷. As far as j_{DC} is lower than 2×10^{11} A/m^2 , the device should thus be cooler than T_{N} and consequently ferrimagnetic.

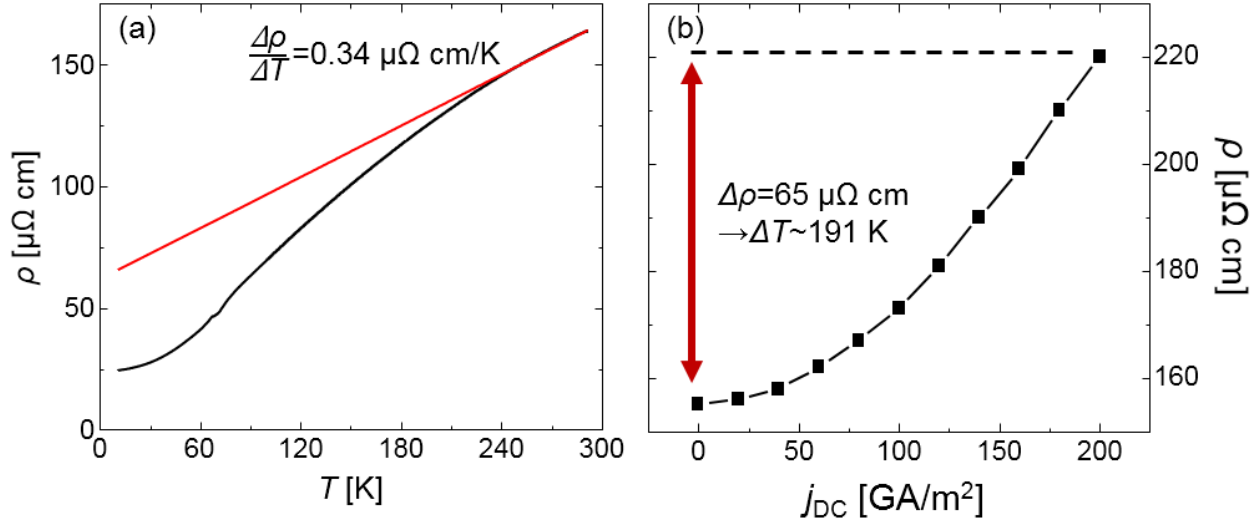


Figure 4-3: (a) Temperature dependence of ρ . (b) Current density dependence of ρ . Heating effect was estimated from $\Delta\rho$.

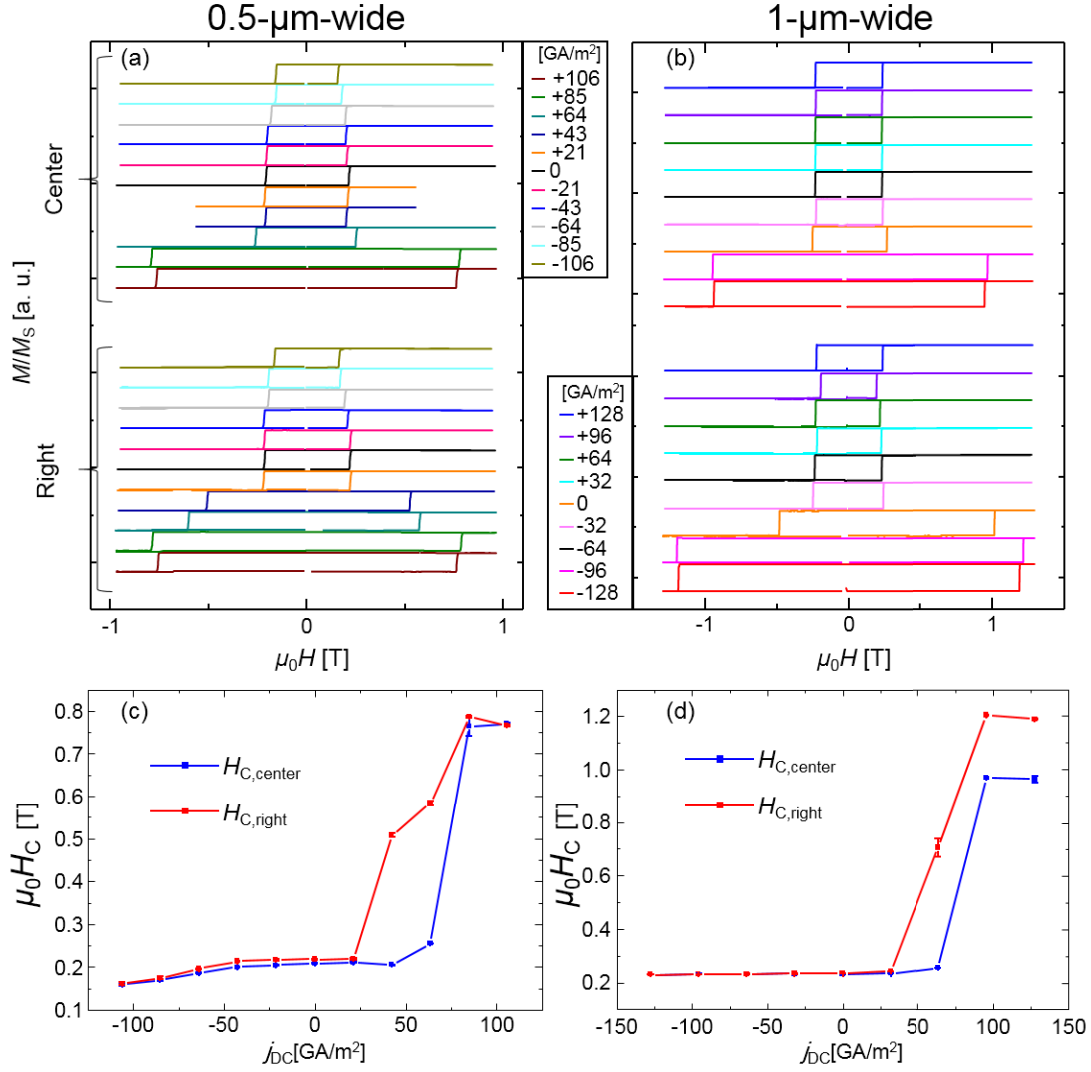
Hall measurements have been performed for 0.5 and 1- μm -wide strips to evaluate the coercivity at the central and right Hall crosses for different DC offsets. The results are shown in Figs. 4-4. Both the 0.5 and 1- μm -wide device showed similar behaviors on DC variation.

The negative current, supposed to assist DW motion, does not affect the switching field. This can be understood by considering that the coercivity is dominated by domain nucleation rather than by DW propagation. As soon as the nucleation occurs, the DW propagates and the Hall cross magnetization switches. The nucleation field H_n is larger than the DW propagation field H_p , but also larger than the DW depinning field H_d corresponding to the notch located between the central and right Hall crosses.

On the other hand, a positive bias, preventing DW motion, induces a drastic increment of coercivity ($\Delta H_C > 0.5 \text{ T}$). As seen in Figs. 4-4 (c) and (d), it is possible to find a regime in which the DW gets trapped in the notch, where a large current density opposes its motion. At larger fields, the DW is depinned from the notch and the magnetization of the right-side cross switches. Positive currents thus act as an additional negative magnetic field [155], preventing DW motion. A rough estimation of the equivalency between field and current can be given by,

$$\varepsilon_{\text{STT}} = \frac{\Delta H_C}{\Delta j_{\text{DC}}} = 6.5 \times 10^{-12} (0.5 \mu\text{m}), 7.7 \times 10^{-12} (1 \mu\text{m}) \text{ Tm}^2/\text{A} \quad (4-1)$$

This value is superior to most major materials for DW-based spintronics such as (Co/Ni) multilayers, Co/Pt, CoFeB, SrRuO₃ or FePt, and comparable with rare-earth ferrimagnet TbFeCo (*cf.* Table 4-1). Note that this value has to be interpreted cautiously: in Mn₄N, the effect of magnetic fields is limited by the small spontaneous magnetization, so that the relative efficiency of the STT appears to be very large.



Figs. 4-4: (a), (b) Magnetization hysteresis loops for different DC bias and (c), (d) switching field H_c variations with the current density for (a), (c) 1- μm -wide and (b), (d) 0.5- μm -wide strips. Only positive currents affect the magnetization reversal fields, by preventing DW motion in the devices. The switching field H_c of the right cross rises at smaller currents than that of the center cross, because of the presence of the notch between the two crosses.

Table 4-1: STT efficiency values of several magnetic materials. Most of them without any mark were obtained from DW depinning experiment at zero field. * and \dagger present the results obtained from CIDWM in the presence of field and coercivity tuning by bias current as in this work, respectively.

Material	(Co/Ni) _N	CoFeB	SrRuO ₃	FePt	TbFeCo	Mn ₄ N
ε [$10^{-14} \text{ Tm}^2/\text{A}$]	60	0.8	100	30*	920	770 \dagger
Reference	156	157	158	159	160	This work

4.3. Pinning of the DW on the notch

For current densities around 50 GA/m^2 , the coercivities of the central and right crosses are different, enabling to pin a DW at the notch. Figure 4-5 is a schematic diagram of the expected variations of the longitudinal voltage. In such a double Hall cross with perpendicular magnetization, there is an AHE contribution coming from the contacts to the longitudinal voltage¹⁶¹. In the saturated state, the Hall contributions to the transverse voltage are the same for each cross, and cancel out. However, when a DW is located in-between the Hall crosses, the magnetization directions are different in the two crosses, giving AHE contribution of the same sign. This leads to sharp variations of the longitudinal voltage when the crosses magnetizations switch. Additionally, the magnetization switching of the strip induces resistance variations due to the Magnon Magneto-Resistance^{162,163} and possibly to DW resistance^{161,164}.

Figures 4-6 (a) and (b) presents the experimental 4-probe resistance ΔR_{xx} between the central and right crosses for a (a) $0.5\text{-}\mu\text{m}$ and a (b) $1\text{-}\mu\text{m}$ -wide device. At the end of this partial reversal process, the voltage indicates that a DW is pinned on the notch. Figures 4-6 (c) and (d) shows the AFM and MFM images of the notch after this field process, for a $0.5\text{-}\mu\text{m}$ -wide strip. Although the MFM signal is weak, because of the small magnetization of Mn_4N , the phase profile along the strip presented in Figs. 4-6 (e) shows 2 levels of contrasts when crossing the notch. This is compatible with the presence of a DW at the notch.

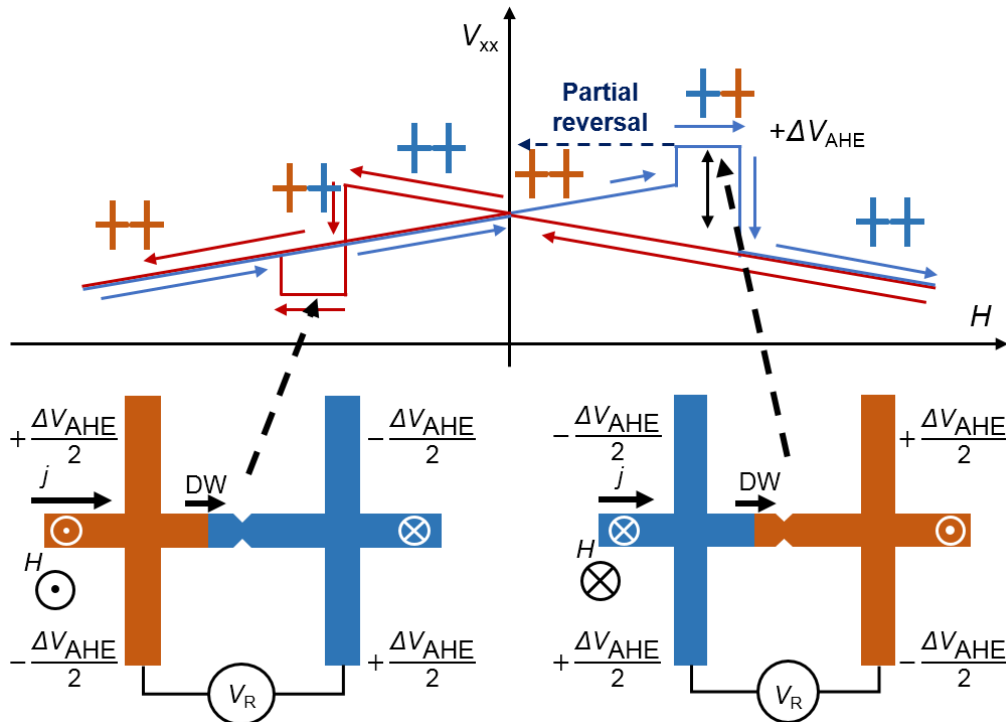
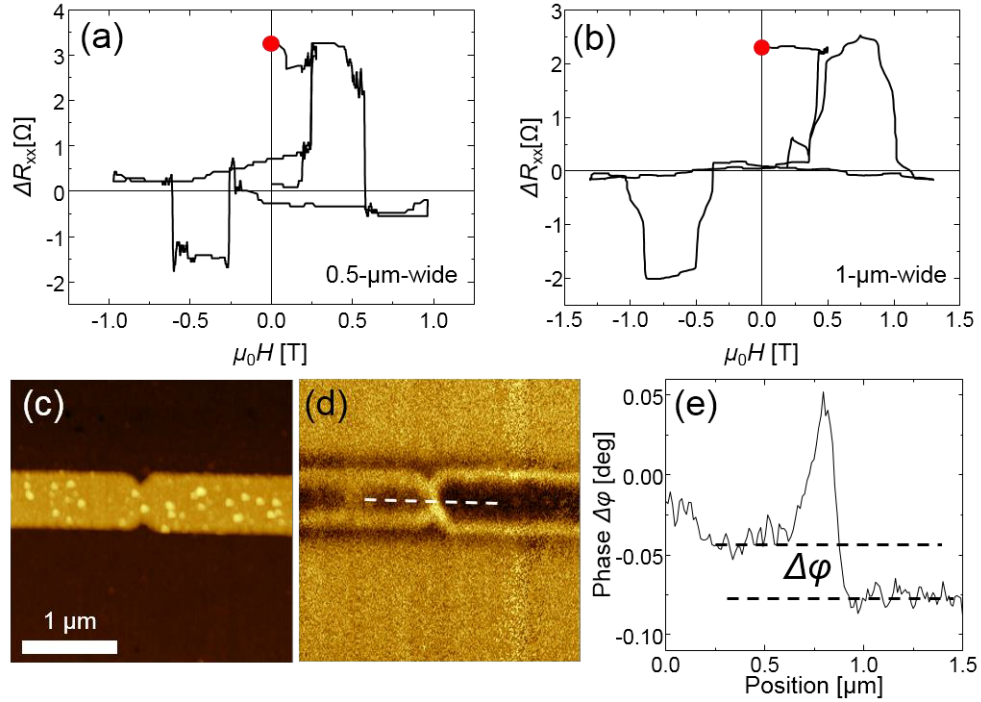


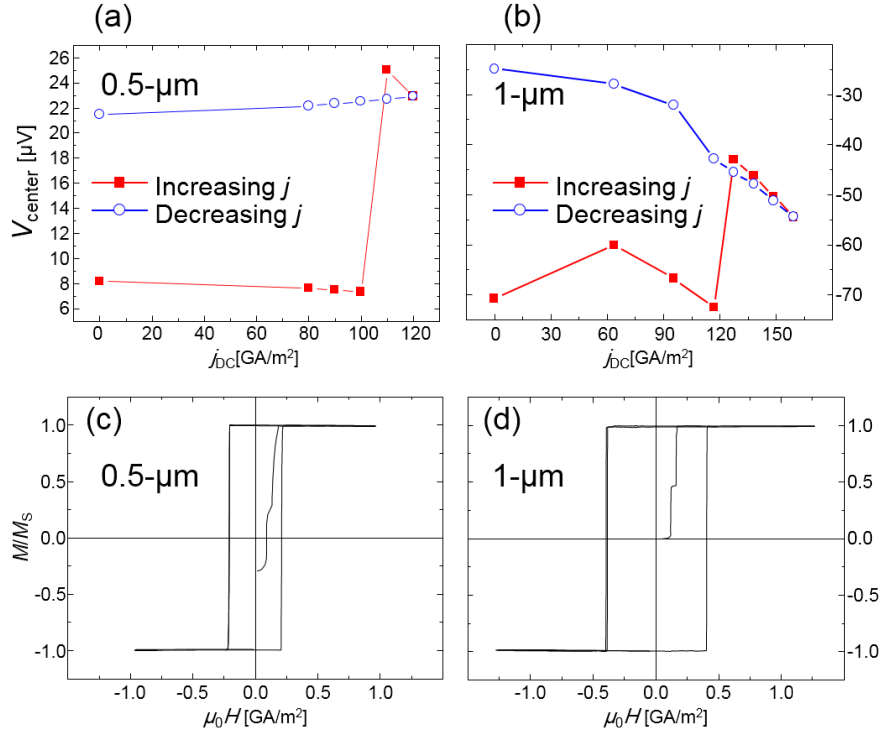
Figure 4-5: Schematic illustration of 4-probe voltage under magnetic field and corresponding DW arrangement. The proportional slope of resistance respect to the field is due to MMR. Rectangular signal corresponds to the difference of Hall signal between 2 Hall crosses.



Figures 4-6: (a), (b) 4-probe resistance between the center and right Hall crosses as a function of the magnetic field, for (a) a 0.5- μm and (b) a 1- μm -wide device. The red dots indicate the end of the minor loop. (c) AFM and (d) MFM images of a 0.5- μm -wide strip after partial reversal. The phase difference $\Delta\phi$ between the two sides of the constriction, shown in (e) suggest that a DW is indeed pinned at the notch.

4.4. CIDWM without external field assistance

After pinning DW at the notch, a DC current was injected in absence of external magnetic field. The magnetic state was monitored by measuring the AHE signal in the central Hall cross, here again using a lock-in technique with small AC for the detection, for various DC bias. The direction of positive current is defined as in the last section, from the nucleation pad towards the right side, so that a positive current pushes the DW from the right side to the left side. Figures 4-6 show the anomalous Hall voltage of the central Hall cross for (a) 0.5- μm -wide and (b) 1- μm -wide device under several DC bias. After injection of a 1.2×10^{11} A/m² DC, the Hall voltage rose to a higher value indicating, the arrival of the DW at the Hall cross. This threshold current density for CIDWM can be compared to the propagation field. Figures 4-6 (c) and (d) are the hysteresis loops after the DC sweep experiment. These initial states were not saturated, which means that during the CIDWM experiments, the DWs stopped in the middle of Hall crosses, probably because their wider cross-section induces locally a decrease of the current density. On the other hand, the transverse voltage at the right cross did not change during the DC injection, indicating the DW motion occurs from the notch towards the left, along the direction of the electron flow. This result shows that the sign of the spin polarization of conduction electrons is positive, in agreement with the results of the last section and with ref. [117].



Figures 4-6: (a), (b) Hall voltage of the central Hall cross when sweeping positive DC bias in (a) $0.5\text{-}\mu\text{m}$ and (b) $1\text{-}\mu\text{m}$ -wide devices, respectively. The red squares and blue circles denote the increasing and decreasing sweep of current. In the initial state, a DW is pinned on the notch, far from the cross. (c), (d) hysteresis major and minor loops measured by AHE for each device after the CIDWM measurement. From the initial magnetization ratio, the last position of DW in the Hall crosses can be estimated.

4.5. Summary

In this chapter, we used transport measurements to observe STT in Mn_4N . We showed that DC can prevent field-driven DW motion, thus increasing the coercivity of Hall bars. We also demonstrated DW depinning from a notch and subsequent CIDWM by DC, in absence of magnetic field. The STT efficiency, derived from the equivalency between DC and external fields, is found to be of $7 \times 10^{-12} \text{ T}\cdot\text{m}^2/\text{A}$, with a threshold current density for DW motion of $1.2 \times 10^{11} \text{ A/m}^2$.

As said before this high efficiency might also be a consequence of the small magnetization. In the next chapter, we will study directly the variations of the DW velocity with the DC, in absence of magnetic field.

Chapter 5 Evaluation of DW speed and spin-transfer efficiency

In chapter 4, CIDWM in Mn₄N microstrips has been achieved using DCs. However, for practical applications the threshold current density is not the sole important parameter: the DW velocity is an indicator of the speed at which information can be written or read in any DW-based device. In order to determine DW velocities it is thus necessary to use current pulses. In this chapter, we use current pulses coupled to MOKE microscopy observations, and we demonstrate the potential of Mn₄N as a candidate for CIDWM application by showing that standard STT can lead to very high DW speeds in this material, reaching almost 1 km/s.

After discussing the device fabrication, we will show the results of DW velocity measurements. We will then discuss the origin of the high DW mobility in Mn₄N. We will finally show that these measurements provide an estimation of the spin polarization.

5.1. Device fabrication

10-nm-thick Mn₄N film have been grown by MBE on STO, using the process presented in chapter 3. Figures 5-1 (a) show the results of out-of-plane XRD, in-plane XRD, and RHEED, which evidence a successful epitaxial growth. The result of ω -rocking curve measurements shown in Figures 5-1 (b) evidenced that the Mn₄N crystal has been oriented along [001] direction well and with low mosaicity.

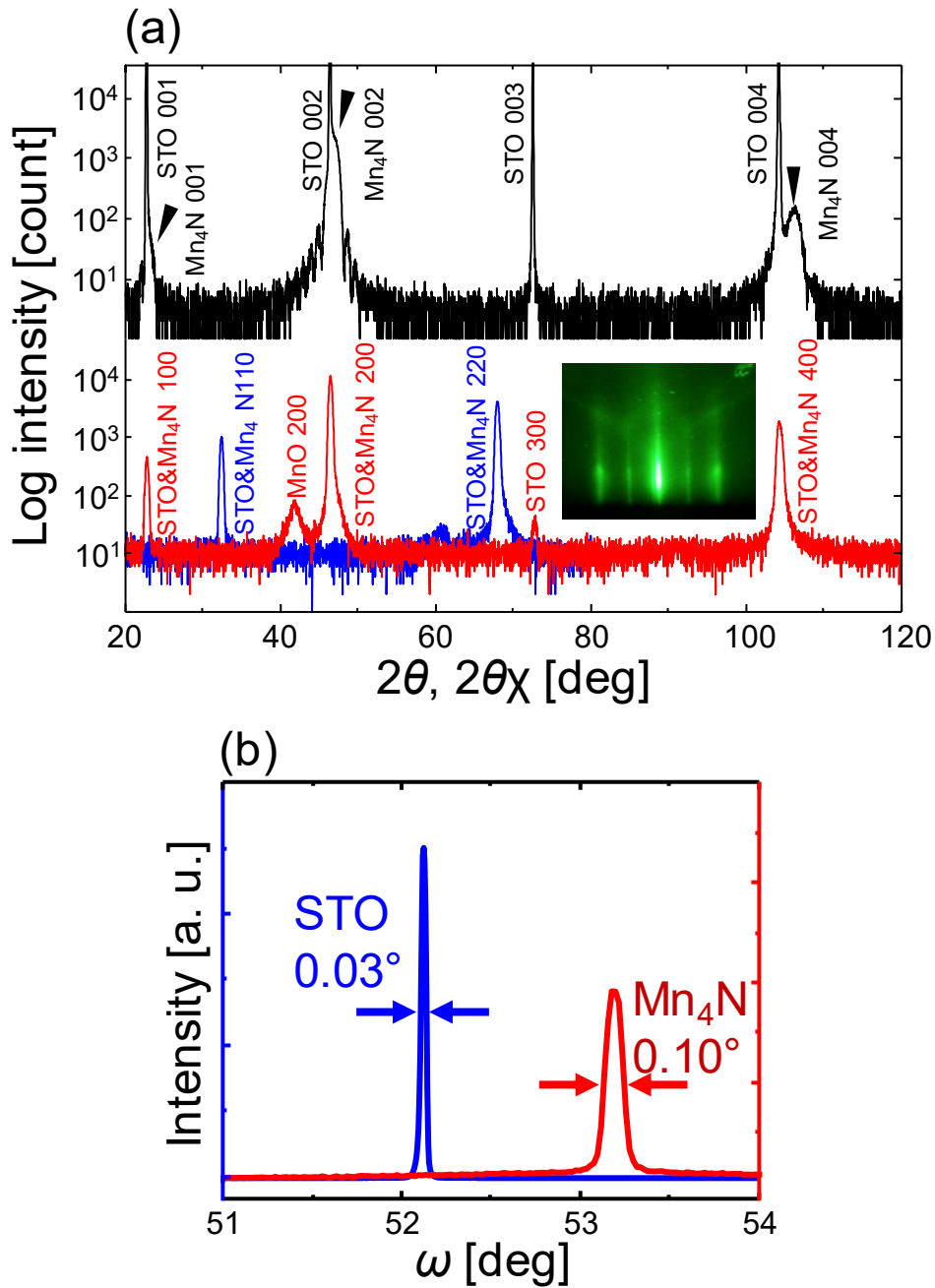
The magnetic and magneto-transport properties of the film have been measured before nanofabrication. Figures 5-2 present the hysteresis loops measured (a) by MPMS and (b) by AHE using a magneto-transport measurement system. From the integration of the M - H loops, the uniaxial anisotropy K_u is estimated to be 1.1×10^5 J/m³, similarly to the sample of chapter 3, and even though the spontaneous magnetization was smaller (only 66.1 kA/m). Note that the magnetization Mn₄N is quite sensitive to the amount of nitrogen atoms¹¹⁵.

The magneto-transport properties shown in Figures 5-2 (b) are typical of our Mn₄N/STO samples: $\rho_{xx}=178 \mu\Omega\cdot\text{cm}$, $\rho_{AH}=3.97 \mu\Omega\cdot\text{cm}$, $\theta_{AH}=-2.23 \%$. The domain structure observed by MOKE and shown in Figures 5-2 (c) possesses also millimeter-sized domains.

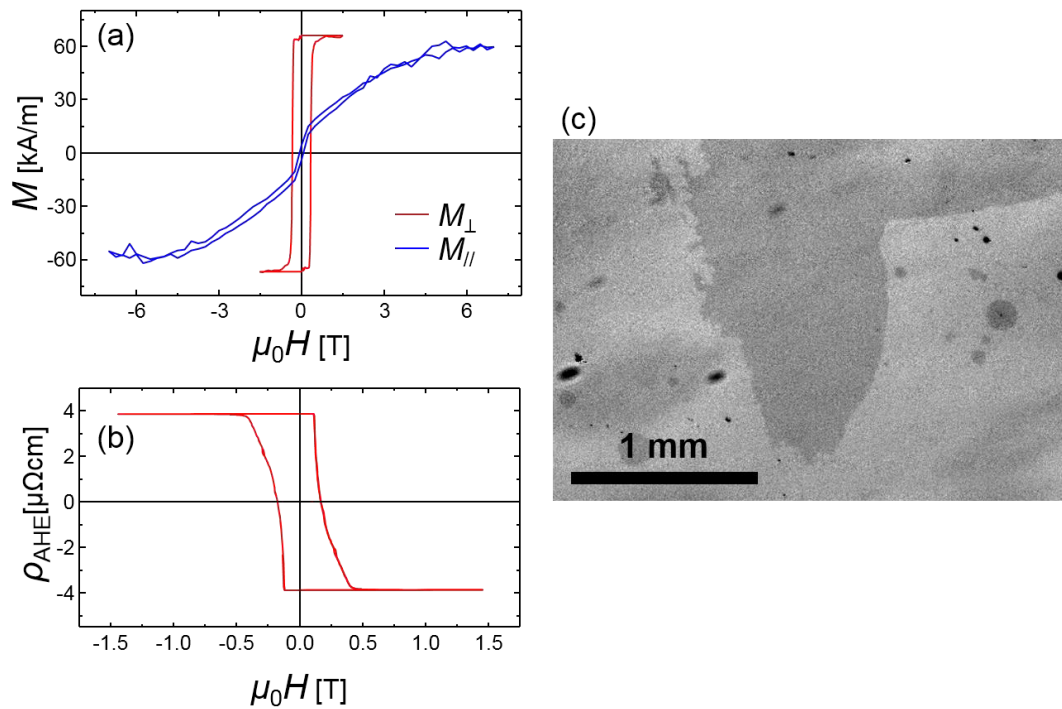
The Mn₄N film has been processed to create the multi-microstrips device shown in Figures 5-3 (a). This device consists of 2 electric contacts connected by 20 strips. The current flows through the strips, where it can possibly induce DW motion.

Under perpendicularly applied fields, the reversed domains nucleate firstly in the pad, probably because nucleation is extrinsic, and because the odds of finding a defect with a low nucleation field are bigger in a large area¹⁶⁵. Both electrical contacts are covered by Ti/Au/Ti electrodes, obtained using a lift-off process. This allows wire-bonding the sample, and being sure that all the strips are submitted to the same voltage difference, and thus to the same current density.

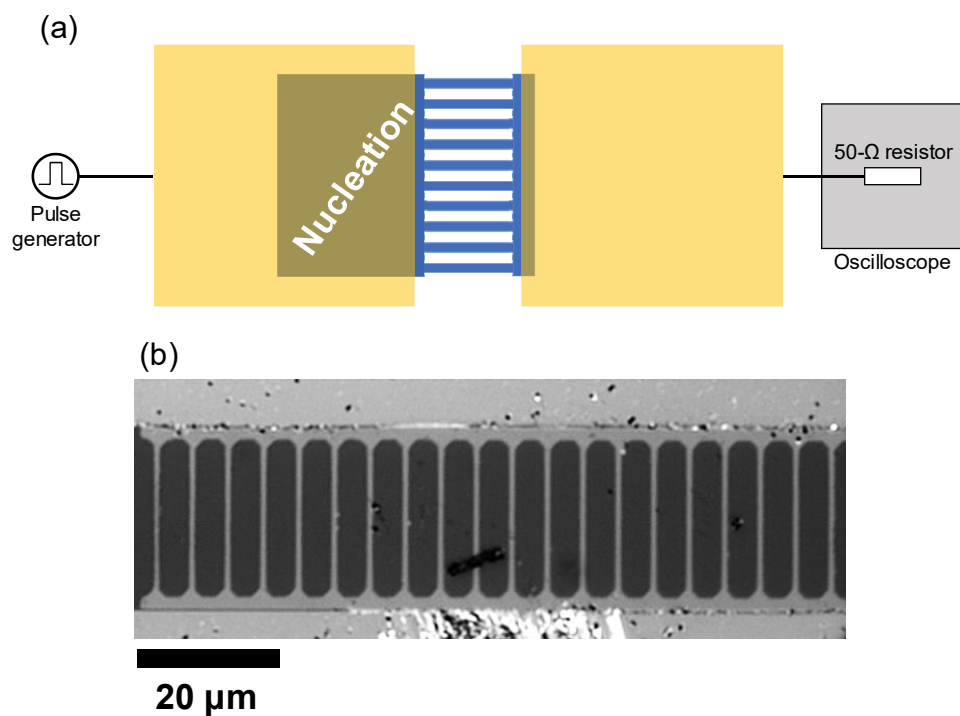
The top Ti layer suppresses the reflection at the surface that could be caused by Au, and enable to increase the light intensity to optimize MOKE signal with avoiding saturating the CCD sensor. Figures 5-3 (b) is an optical microscope image of multi-strips patterns.



Figures 5-1: (a) XRD spectra with the scattering vectors along (black) [001] (out-of-plane), (red) [100], and (blue) [110] direction. The inset is the RHEED pattern for an incidence of the electron beam along STO [100]. The series of diffraction peaks only 001-oriented in the XRD spectra, and the streaky RHEED pattern testify of the successful epitaxial growth of Mn₄N. (b) ω-rocking curve at the (blue) STO 004 and (red) Mn₄N 004 diffractions peak.



Figures 5-2: (a) Hysteresis loops for out-of-plane (red) and in-plane (blue) fields, measured by MPMS. (b) Hysteresis loop measured by anomalous Hall effect, for out-of-plane applied field. (c) MOKE image of the thin film after partial reversal.



Figures 5-3: (a) Schematic of multi-strips device with electronic scheme. (b) Optical microscope image of the multi-strips.

5.2. Speed of DWs driven by current pulses

The domain wall displacement during the pulses has been measured using a differential Kerr imaging technique, *i.e.* subtract the MOKE image before pulse injection as a background from the one obtained after to highlight the difference between them and showing the corresponding magnetization reversal by DW displacement. After saturation of the magnetization, magnetic field pulses have been applied to nucleate a domain in a pad and to inject DWs into the microstrips. The DWs have then been pushed by current pulses, generated by a pulse generator able to provide voltage up to 80V, and pulses duration down to 1 ns.

5.2.1. DW speed measurement

Figure 5-4 shows the measurement set-up. The multi-strips device has been connected to the pulse generator and to an oscilloscope, in order to monitor the shape of pulse using the oscilloscope. A coil and its power supply under the sample stage allows applying magnetic field pulses. The magnetic state of the device is being monitored by MOKE microscope in differential mode.

Figures 5-5 (a) - (d) denotes a typical result of a DW motion measurement. The magnitude and length of field pulse have been optimized in order to stop DWs in the middle of strips as shown in Figures 5-5 (a). In Figures 5-5 (b), the black contrast corresponds to the displacement of the DWs during the current pulse. The direction of DW motion is opposite to the current, which is consistent with the movement due to STT. The displacement of the DWs Δx is obtained by measuring the full width at half of maximum (FWHM) of the MOKE profile along the wire (*cf.* Figures 5-5 (c)).

As seen in Figures 5-5 (d), the pulse shape is not perfectly square. It can be analyzed to derive DW velocity and the current density, by assuming that the DW cannot move under the threshold current, and that its speed is proportional to the current density.

This analysis process is repeated for each input voltage, and consist in 5 steps:

- (i) calculation of the current density by dividing the current measured through the 50- Ω resistor by the number of strips (20) and their cross-sectional area ($1, 2 \mu\text{m} \times 10 \text{nm}$)
- (ii) integration of the j - t curve to obtain the area S over the threshold current ($j_{\text{th}}=3.0 \times 10^{11} \text{ A/m}^2$ for 1-ns-long pulse) as illustrated on Figures 5-5 (d)
- (iii) calculation of the pulse height j_{ave} , obtained by averaging the data points beyond 80 % of the maximum height.
- (iv) calculation of the precise pulse length and DW velocity as $\tau = S / (j_{\text{ave}} - j_{\text{th}})$ and $v_{\text{DW}} = \Delta x / N \tau$, respectively, where N is the number of pulses injected in-between the two images
- (v) averaging of all the v_{DW} values for all the DWs, except for the obviously irregular ones, for which v_{DW} is smaller than one-third of the maximum v_{DW} at the studied current density.

Finally, the pulse length was varied to check the influence of the rising and falling tail of the pulse on the estimation of the DW speed. The experiment was performed for current pulse ranging from 0.5 to 3 ns and show consistent DW velocities.

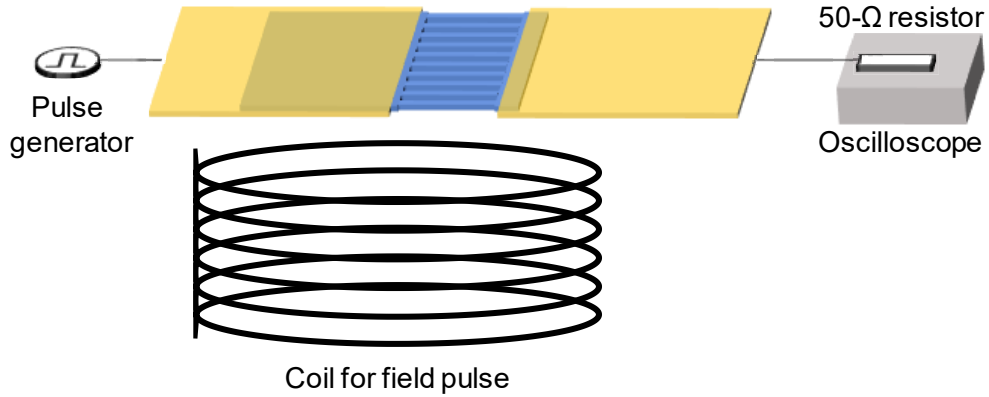
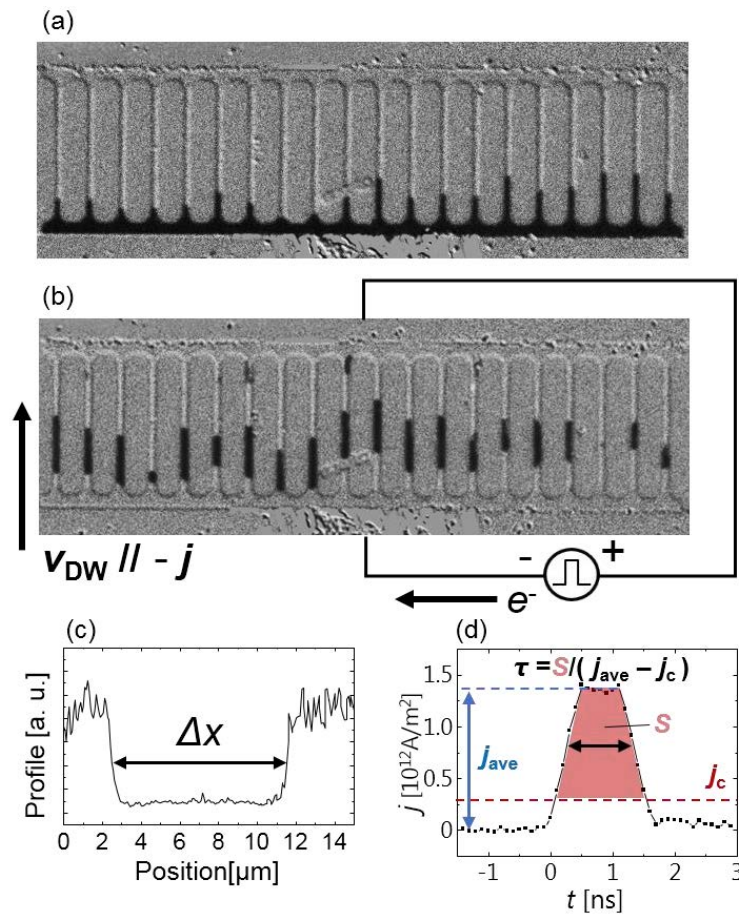


Figure 5-4: Experimental set up used to measure current-induced DW velocities. The whole set-up is placed under the objective of a MOKE microscope.



Figures 5-5: (a) Differential MOKE image after domain nucleation using a field pulse of 0.6 T during 300 μs . (b) Differential MOKE image after eight current pulse injection of 1.2 A/m^2 and 1 ns. The area through which the DW propagated appears in black. The DW motion direction is opposite to the current, and thus follows the electrons flow. (c) The profile of MOKE image along the strip after DW motion. The DW displacement has been derived as the FWHM as denoted in the figure. (d) the shape of injected pulse monitored on the oscilloscope.

5.2.2. Current dependence of DW speed

Figure 5-6 presents the current density dependence of the DW velocity. As stated above, the threshold current density for 1-ns-long pulse is $3.0 \times 10^{11} \text{ A/m}^2$. Above $8 \times 10^{11} \text{ A/m}^2$ in 1- μm -wide strips, the trend of the

$v_{\text{DW}}-j$ curve becomes linear. We will show later that this behavior is close to the theory of CIDWM in a 1D model. In the studied range of current densities, the DW reached a maximal average velocity of 900 m/s, for a current density of 1.3×10^{12} A/m² in both 1- μm and 2- μm -wide strips. This value is the highest in all materials and structures whose DW was driven by only pure STT, and the second highest value when looking at SOT-driven systems, then we introduce some report of DW velocities driven by STT and SOT.

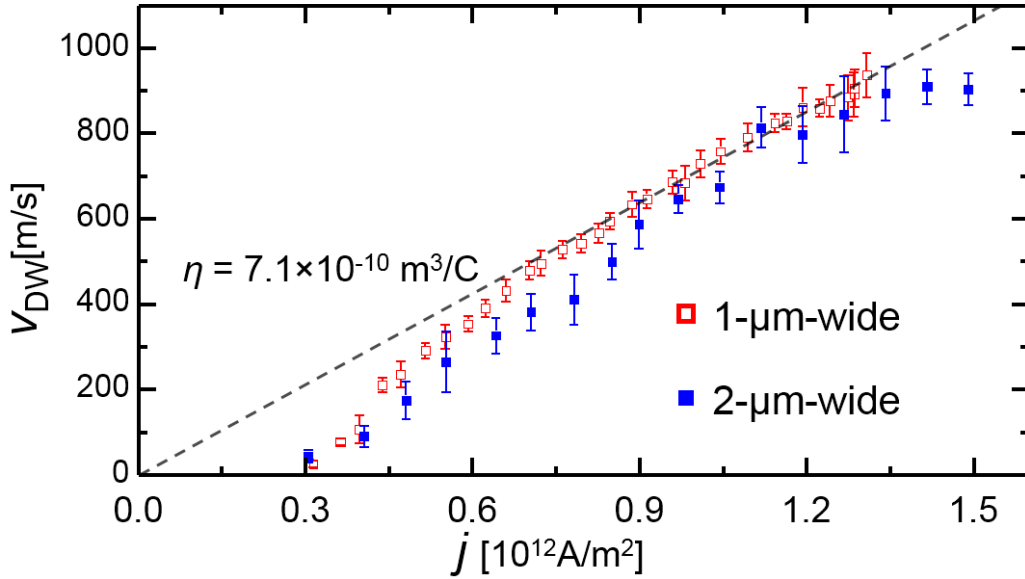


Figure 5-6: Current density dependence of DW velocity measured at room temperature. Both the 1 and 2- μm -wide strips possess similar behavior. The DW mobility has been derived from the linear fitting in the high j regime.

Since DWs are wide ($>100\text{nm}$) in in-plane systems, the interest in applications to logic and storage devices is limited. Quite high spin transfer efficiencies have been measured in systems with perpendicular magnetic anisotropy (PMA) such as Co/Ni or FePt¹⁵⁹, but in these systems DW motion at zero field is usually hindered by pinning, which induces a large coercivity and a stochastic behaviour. In Pt/Co/Pt, DWs could not be moved by STT, due to the limited spin polarisation within the Co layer¹⁶⁶. On the other hand, very high DW mobilities were found in magnetic semiconductor films such as (Ga,Mn)(As,P) for very low current density^{167,168}. However, these measurements were done at low temperature, and the current density was limited to some 10^{10} A/m², with a maximum speed of 30m/s at 10^{10} A/m².

The velocities observed in Mn₄N can thus be considered as a milestone in the history of spin transfer torques. Although in recent years the community has focused nearly entirely on SOT-driven DW dynamics, the giant DW velocities obtained in Mn₄N, show that the STT can be competitive with SOT. SOT has been found to be an efficient mechanism to drive DWs in non-centrosymmetric multilayers, in which a FM is deposited on a heavy metal like Pt^{169,170}. The prototypical example is AlOx/Co(0.6nm)/Pt⁹⁵ where the chiral Néel structure acquired by the DWs in the presence of interfacial Dzyaloshinskii-Moriya interaction⁶⁵ leads to a high mobility ($v = 400$ m/s for $j = 3 \times 10^{12}$ A/m²) with a satisfying reproducibility of the DW movements. Higher SOT-driven DW mobilities were obtained recently in a multilayer structure in which two Co/Ni layers were coupled anti-ferromagnetically through a Ru layer⁹⁶, or in GdCo ferrimagnet layers deposited on top of Pt⁹⁷. In these systems the DW velocity was clearly observed to vary with the total magnetization. In the former experiment, a

maximum velocity of $v = 750$ m/s for $j = 3 \times 10^{12}$ A/m² was obtained at room temperature using a Ru spacer layer, so that the stack magnetization was reduced to 8% of the spontaneous magnetization of a single Co/Ni layer. In the latter one, a peak velocity of 1300 m/s was reported at the compensation temperature, for a current density of 2×10^{12} A/m² and still high even at 300 K of 850 m/s. In this context, the velocities presented here at room temperature for DWs in Mn₄N are comparable to the best results obtained using SOTs. Moreover, they represent the first demonstration of very efficient current-driven DW motion by pure STT using a system with PMA.

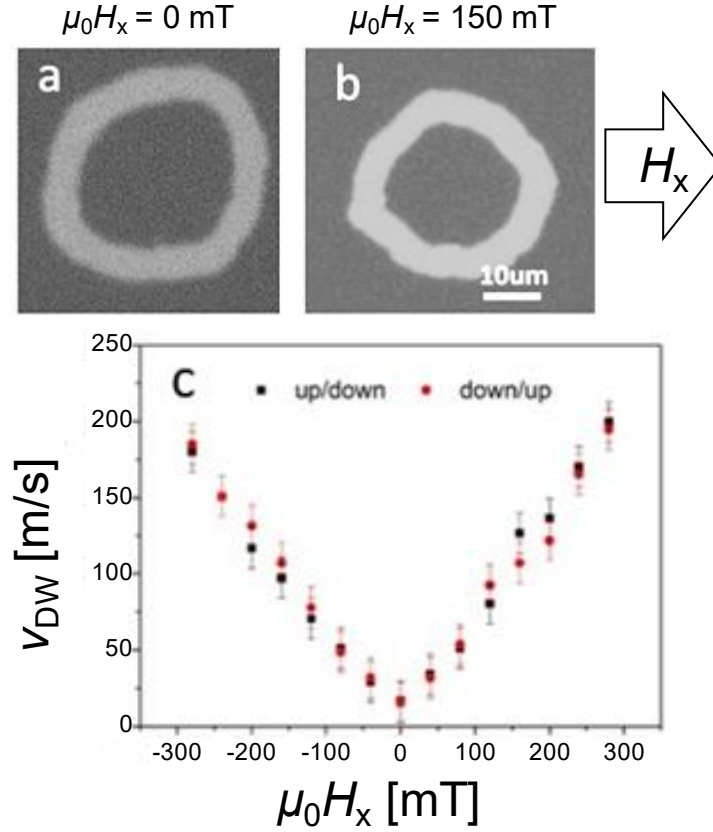
Another figure of merit of the STT efficiency is the DW mobility $\eta = \frac{dv_{\text{DW}}}{dj}$, that can be derived from the $v_{\text{DW}}-j$ curve, and is equal to 7.1×10^{-10} m³/C. This mobility is also the highest value in all STT-driven systems, and it is superior to most SOT-driven records.

Above 1.3×10^{12} A/m², many domains nucleate everywhere, probably because the sample reaches the Mn₄N Curie temperature about 745 K¹⁰⁷, and becomes temporarily paramagnetic.

5.2.3. Field driven Domain wall motion

DWs having a chiral Néel structure stabilized by interfacial Dzyaloshinskii-Moriya Interaction (DMI) can be driven by spin-orbit torques (SOTs), arising from the Spin Hall Effect or from Rashba effects¹⁷¹. In order to exclude the contribution of SOTs to the DW dynamics in our system, we have carried out measurements aiming at establishing the nature of the DW structure. The domain wall dynamics was driven by an out-of-plane magnetic field, in the presence of a continuous longitudinal in-plane field H_x . The domain wall velocity in the direction of the in-plane field depends on the nature of the internal DW structure. In the case of Bloch walls, the DW speed increases as a function of H_x , and is the same for fields of opposite signs (v_{DW} vs. H_x curve is symmetric). On the other hand, the presence of DMI induces an asymmetry of v_{DW} vs. H_x curve, with a minimum of the speed when the H_x field compensates the DMI field^{172,173}.

An example of DW displacement in absence and in presence of an in-plane magnetic field of 150 mT is shown in Figures 5-7 (a, b). The white contrast in the Kerr images represents the displacement of the DW during the field pulse. This displacement is isotropic in the presence of the in-plane field, which indicates the absence of DMI. The domain wall speed vs. H_x curve is shown in Figures 5-7 (c).



Figures 5-7 (a, b): Differential Kerr images showing the displacement of domain walls driven by an out-of-plane magnetic field pulse, of amplitude of around 400 mT, and of 30 ns duration (white contrast), in the absence (a) and in the presence (b) of an in-plane continuous magnetic field H_x of 150 mT. (c): domain wall speed driven by $\mu_0 H_z = 320$ mT perpendicular field pulses, as a function of the in-plane field amplitude H_x , for an up/down and a down/up domain wall. The symmetric curve confirms the presence of achiral domain walls.

5.3. Origin of the high DW mobility in Mn₄N

In order to understand the origins of such a high DW mobility, which appears to be induced by only classical STT in Mn₄N thin films, we have considered the analytical expression of the STT in the adiabatic limit.

As introduced in the chapter 2, when $j \gg j_c$, the DW moves in the precessional regime at a velocity given by,

$$v_{\text{DW}} \approx \frac{1}{1 + \alpha^2} |\mathbf{u}| \quad (5-1)$$

where $\mathbf{u} = \frac{g\mu_B}{2eM_s} P\mathbf{j}$ is the spin-drift velocity, parallel to the electrons flow. Experimentally, a linear regime indeed appears in the $v_{\text{DW}}-j$ curve above the steady regime. The conjunction of the small M_s and high P is responsible for the large observed DW velocities, as the mobility dv_{DW}/dj is expected to be proportional to P/M_s .

To confirm this interpretation, micromagnetic simulation have been performed by the finite-difference software MuMax3¹⁷⁴. Simulations at 0 K have been performed in a defect-free strip of $6000 \times 120 \times 10$ nm³ with a cell size of $2.5 \times 2.5 \times 10$ nm³. The results are shown in Figure 5-8 with the used parameters, giving an overall agreement with the 1D model and with the experimental results in the high current densities regime. On the other hand, the trend of the DW speed in the low current regime is different from the experiment, the experiment

showing a relatively large critical current density of 3.0×10^{11} A/m². This is due to the pinning of the DWs by defects in the actual devices while the system is supposed to be perfect without any disorder in the simulation. If the sample were perfect, we could move DW starting at j_c .

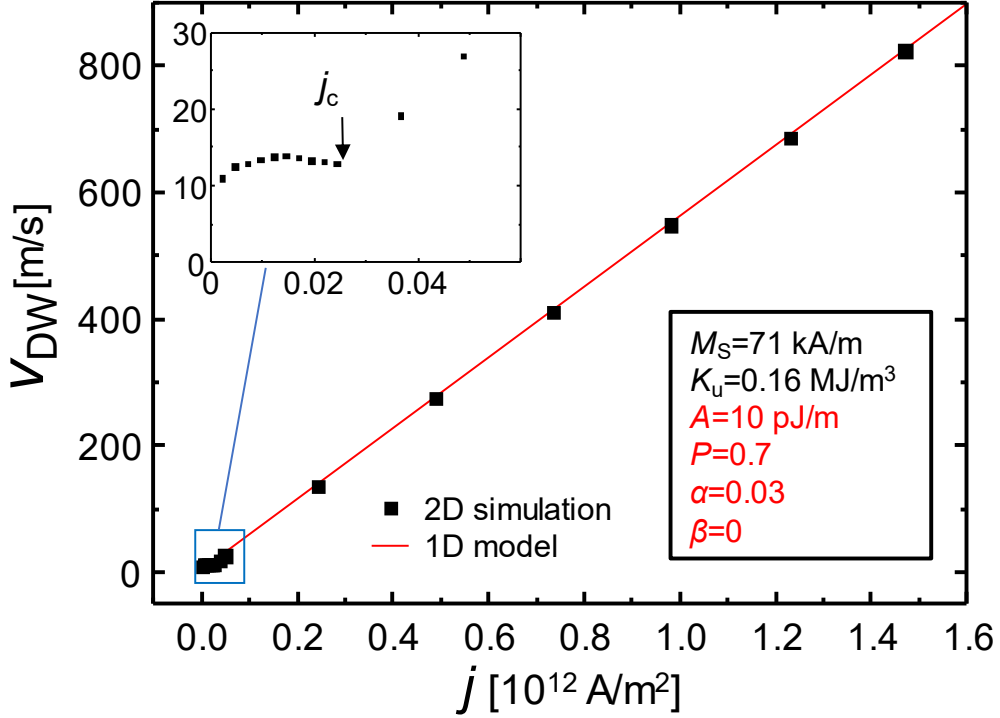


Figure 5-8: DW velocity as a function of the current density dependence of in the adiabatic limit. Squared dots denote the results of 2D micromagnetic simulations while the red line is the theoretical v_{DW} obtained using the 1D model. The upper left inset shows the DW speed around the theoretical threshold current j_c . The lower right inset is the list of the used parameters, those in black being measured and those in red being assumed.

5.4. Estimation of the spin-polarization

In the last section, we saw that the DW velocity v_{DW} is expected to vary linearly with the current density j , and that it corresponds to the spin-drift velocity u . The spin polarization of Mn₄N can be derived from the slope in the high current regime graph, which corresponds to the DW mobility η . Indeed, the spin polarization P is given in the 1D model by,

$$P = \eta \frac{2eM_S}{g\mu_B} \sim 0.75 \quad (5-2)$$

where $e = 1.60 \times 10^{-19}$ C, $g = 2.0$, $\mu_B = 9.27 \times 10^{-24}$ Am², $M_S = 66.1$ kA/m and $\eta = 7.1 \times 10^{-10}$ C/m³. Note that as mentioned in chapter 2, for ferrimagnet, it is necessary to replace g by g_{eff} . This value is in agreement with the value expected from the first principle calculation ($P = 0.75$), though the experimental P should be the spin polarization of the current corresponding to that of conductivity P_σ ⁷⁵ whereas the calculated P is that of the density of state P_{DOS} ¹⁷⁵. For example of the difference between P_σ and P_{DOS} , ferromagnetic nitride Fe₄N has been expected to possess fully polarized conduction electrons $P_\sigma = -1.0$ while P_{DOS} is only -0.6 ¹⁷⁶. Such a high spin polarization could be of interest not only to develop CIDWM devices, but also for magneto-resistive applications such as GMR or TMR devices.

5.5. Influence of the non-adiabatic torque and of the damping parameter on CIDWM

Up to now we have neglected the effect of the non-adiabatic torque on the dynamics of DWs in PMA systems. While this term had to be considered to explain the DW motion observed experimentally in in-plane magnetized systems like permalloy strips below the intrinsic j_c , we have shown that the large DW velocities observed in our Mn₄N stripes for low current densities can be explained by the adiabatic term alone. It has been shown analytically that the non-adiabatic torque results in a steady regime motion with velocity $v = (\beta/\alpha)u$ below the critical current j_c . On the other hand, a term $\alpha\beta / (1+\alpha^2)u$ is added to the velocity in the precession regime¹⁷³. However, since α is expected to be small in Mn₄N and β is expected to be of the same order of amplitude as α , this term may be neglected

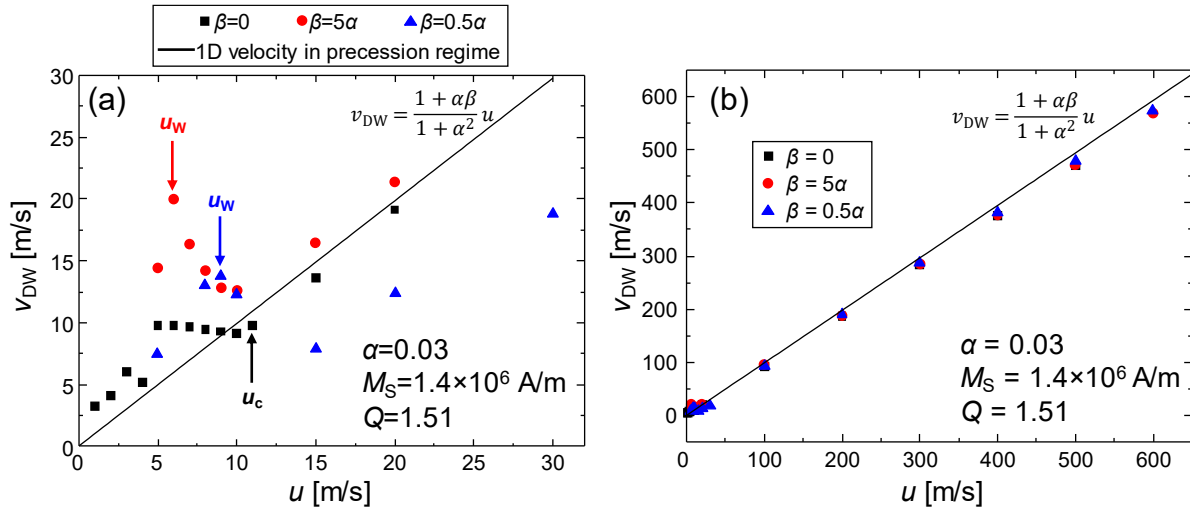
In order to justify our choice to neglect the non-adiabatic torque, we performed micromagnetic simulations considering two extreme cases: $\beta = 5\alpha$ and $\beta = 0.5\alpha$, with $\alpha = 0.03$. The results are shown in Figures 5-9. As shown in Figures 5-9 (a), when the non-adiabatic torque is taken into account, the DW moves in the steady regime until it reaches the Walker spin-drift velocity u_W :

$$u_W = u_c \cdot \frac{\alpha}{|\beta - \alpha|} \quad (5-3)$$

Note that when the non-adiabatic torque is neglected, the Walker spin-drift velocity coincides with the critical spin-drift velocity. Beyond j_c , the DW starts moving linearly with j , in the precessional regime, and the DW mobility is practically independent from the value of β as shown in Figures 5-9 (b).

These results led us to conclude that the non-adiabatic torque is not necessary to explain the velocities experimentally observed. Nevertheless, our experiments do not allow to exclude a priori the presence of the non-adiabatic term, because the regime where it really matters, below j_c , is hidden by the thermally activated regime.

The Gilbert damping could play an important role in the DW motion. In our simulations we have considered a low damping $\alpha = 0.03$, but this value, though plausible, has not been verified experimentally. In order to evaluate the impact of the value of α to the DW mobility, we have carried out micromagnetic simulations for the cases $\alpha = 0.03$ and $\alpha = 0.3$, and compared the results with the 1D model. $\alpha = 0.3$ is the typical high Gilbert damping value obtained for Co layers deposited on large spin-orbit Pt layers. The results are shown in Figure 5-10. The difference in velocity for the maximum current density considered here is only about 6%. The larger damping also results into a larger u_c , but the difference is negligible (see inset of Figure 5-10). Therefore, we can conclude that the uncertainty we have over α does not affect our interpretation.



Figures 5-9: Results of micromagnetic simulations showing the DW velocity under spin-polarized current for different values of β : $\beta=0$ (black squares), $\beta=5\alpha$ (red circles), and $\beta=0.5\alpha$ (blue triangles). The black solid lines represent the 1D model velocity. (a) The results zoomed in the low current regime around the Walker current. Each arrow denotes the point where the magnetization in the DW starts precession, corresponding to the Walker current. (b) The result in wide range of current, mainly illustrating the precession regime.

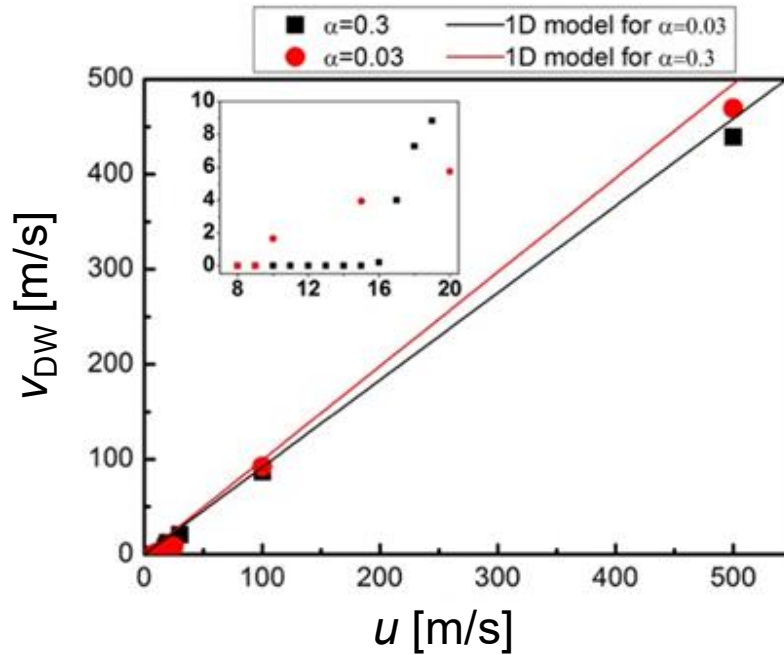


Figure 5-10: Results of micromagnetic simulations showing the DW velocity vs. spin-drift-velocity for two different values of α : $\alpha=0.03$ (red circles), $\alpha=0.03$ (black squares). The solid lines represent the 1D model velocity. The inset presents the zoomed area around the critical current.

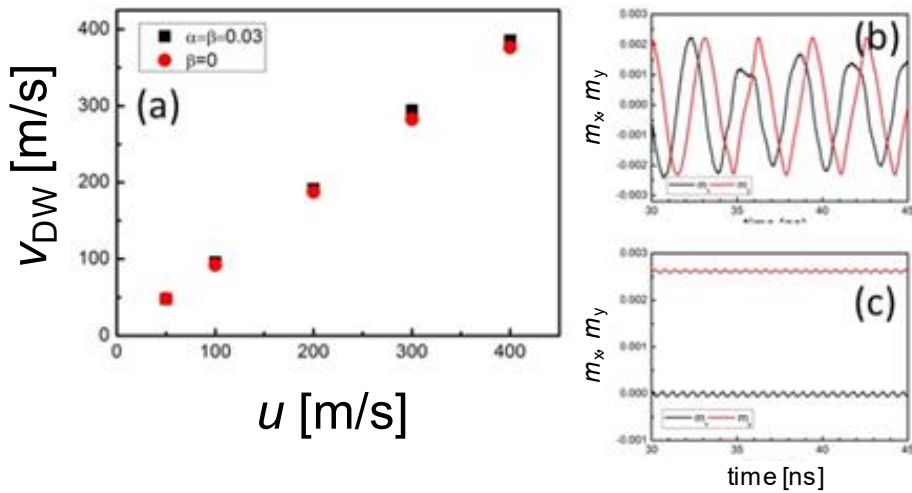
5.6. Damping and non-adiabatic torque: the particular case for which $\alpha = \beta$

So far, we have divided the DW motion behavior in two regimes: the steady regime, below the Walker

breakdown, and the precessional regime for currents above the Walker breakdown. Simulating the DW motion in the precessional regime, and modelling our system as a low-damping material (which implies that $v_{\text{precession}} \approx u$) has allowed us to reproduce the experimental DW velocities.

However, when the Gilbert damping and the non-adiabatic torque compensate each other, *i.e.*, in the hypothesis where $\alpha = \beta$, the 1D model predicts that the Walker spin-drift velocity becomes infinite (eq. (5-4)). In this particular case, the DW moves in the steady regime at a velocity equal to the spin-drift velocity $v_{\text{steady}} = u$, whatever the applied current density. In order to confirm this result, we have simulated a PMA strip with $Q = K_w/K_d = 1.51$, and $\alpha = \beta = 0.03$. The results are shown in Figures 5-11 where they are compared with the case $\beta = 0$. We can note that the velocities do not vary significantly between the two cases. On the other hand, as expected, the DW moves in the precessional regime when $\beta = 0$ while it moves in the steady flow regime when $\alpha = \beta$. This is confirmed by the temporal evolution of the averaged x - and y - components of the DW magnetization that are plotted in Figures 5-11 (b-c).

Note that an experimental evidence of a case where $\alpha = \beta$ has been reported [168, 177]. Here, owing to the small difference between the DW velocity when the non-adiabatic and the damping torque are balanced or unbalanced, we cannot distinguish experimentally between the two cases.



Figures 5-11: Results of micromagnetic simulations showing (a): the DW velocity as a function of the spin-drift velocity for $\beta = \alpha = 0.03$ (black square) and $\beta = 0$ (red circle). (b, c): the temporal evolution of the averaged x (black) and y (red) DW magnetic components: (b) $\beta = \alpha = 0.03$ and (c) $\beta = 0$.

5.7. Summary

In this chapter, the efficiency of the STT in Mn_4N thin films has been evaluated by measuring the speed of DWs driven by current pulses. The DW velocity reaches record values of 900 m/s for a current density of $1.3 \times 10^{12} \text{ A/m}^2$. This value is the highest in all STT-driven systems, and is comparable to the highest speed obtained using SOTs. The DW mobility η derived from the slope of the $v_{\text{DW}}-j$ curve is also very large ($7.1 \times 10^{-10} \text{ m}^3/\text{C}$), the highest in all STT-based systems too. Fit of our data using a 1D analytical model allows extracting a spin polarization of the conduction electrons of 0.75 ± 0.05 , suggesting that Mn_4N could be suitable to obtain

large MRs. As a future perspective, we plan to investigate CIDWM in the flow regime: below the threshold current density with longer current pulses. SOT-driven DW motion measurement is also planned by harmonic Hall measurement¹⁷⁸ in W/Mn₄N/STO stack structure to evaluate the SOT properties.

Chapter 6 Mn substitution by Ni in Mn₄N thin films

Rare-earth based ferrimagnetic materials with PMA such as TbFeCo and GdFeCo are currently attracting attention because their magnetization is controllable by tuning the composition. In particular, at the angular momentum compensation point, extremely fast DW motion driven by magnetic field and SOT is reported^{97,179}.

Mn₄N possesses suitable properties for spin-torque applications, i.e., a small M_S (~100 kA/m), and a high K_u (~0.1 MJ/m³). Additionally, we have shown in previous chapters amazing features for DW motion applications, such as the huge domain structure resulting from the scarcity of DW pinning sites and domain nucleation centers, the ultrafast CIDWM ($v_{DW} \sim 900$ m/s with $j \sim 1.3 \times 10^{12}$ A/m²), and the high spin polarization of conductivity ($P_\sigma \sim 75 \pm 5$ %), even though it is composed of only light and abundant elements.

The ferrimagnetic mechanism of Mn₄N is due to the existence of crystallographic sublattices, i.e., of a large moment at the corner site (I-site), and small moment at the face-centered site (II-site), as shown in Figure 6-1. This contrasts to rare-earth ferrimagnets where the moment of rare-earth atoms is antiparallel to that of Fe and Co. Therefore, Mn₄N cannot be compensated by tuning the composition.

During these 5 years, we have been investigating some alloys based on Mn₄N in which Mn was substituted by 3d metals such as Co¹⁰⁴, Fe^{105,118,180} and Ni¹⁸¹ to tune the magnetic properties. Beyond exploring the properties of Nitrides, the main objective was to search for a M_S reduction of Mn_{4-x}Co_xN and Mn_{4-x}Ni_xN, while conserving the perpendicular magnetization.

In this chapter, we focus on Mn_{4-x}Ni_xN samples grown on STO, evaluating their magnetic and magneto-transport properties, and trying to reach the compensation point by substituting Mn by Ni.

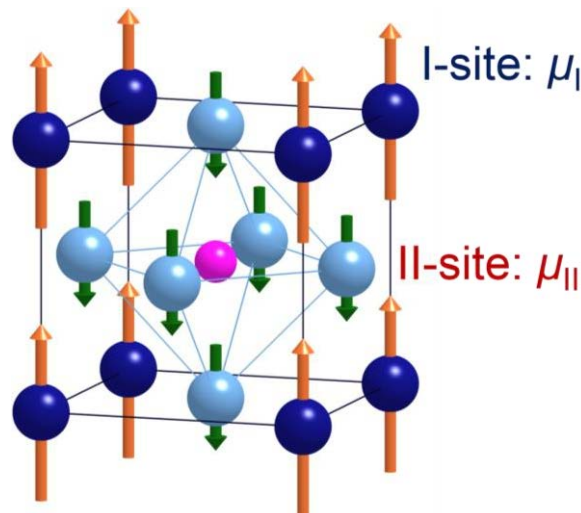


Figure 6-1: Anti-perovskite structure of Mn₄N, with the magnetic moments at each sublattice. The I (II) site corresponds to the corner (center of the faces) of the unit cell.

6.1. Growth and crystallinities

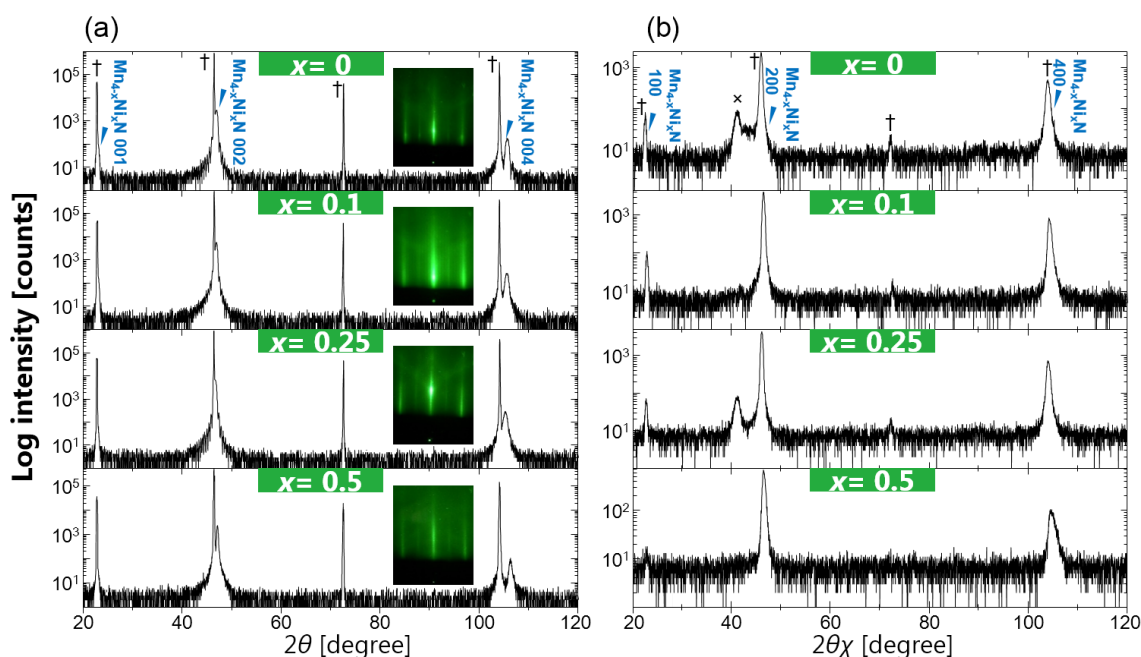
6.1.1. MBE growth of Mn_{4-x}Ni_xN

Mn_{4-x}Ni_xN thin films were grown on STO substrates by molecular beam epitaxy, using the process already described in chapter 3 and 5. The nominal amount of Ni-substitution, x , has been determined from the

ratio of the deposition rates measured before the growth. Four compositions have been probed: 0, 0.1, 0.25, and 0.5.

6.1.2. Crystalline quality of the Mn_{4-x}Ni_xN films

The crystalline quality of the deposited samples has been characterized by out-of-plane/in-plane XRD and RHEED, similarly to what has been done in chapter 3. Figures 6-2 show the results of (a) out-of-plane and (b) in-plane XRD, together with the RHEED result along STO [100]. They indicate a successful epitaxial growth of Mn_{4-x}Ni_xN, in single phase, and with good orientation. The thicknesses of these films have been also measured by X-ray reflectometry, and all sample are 25 nm thick.

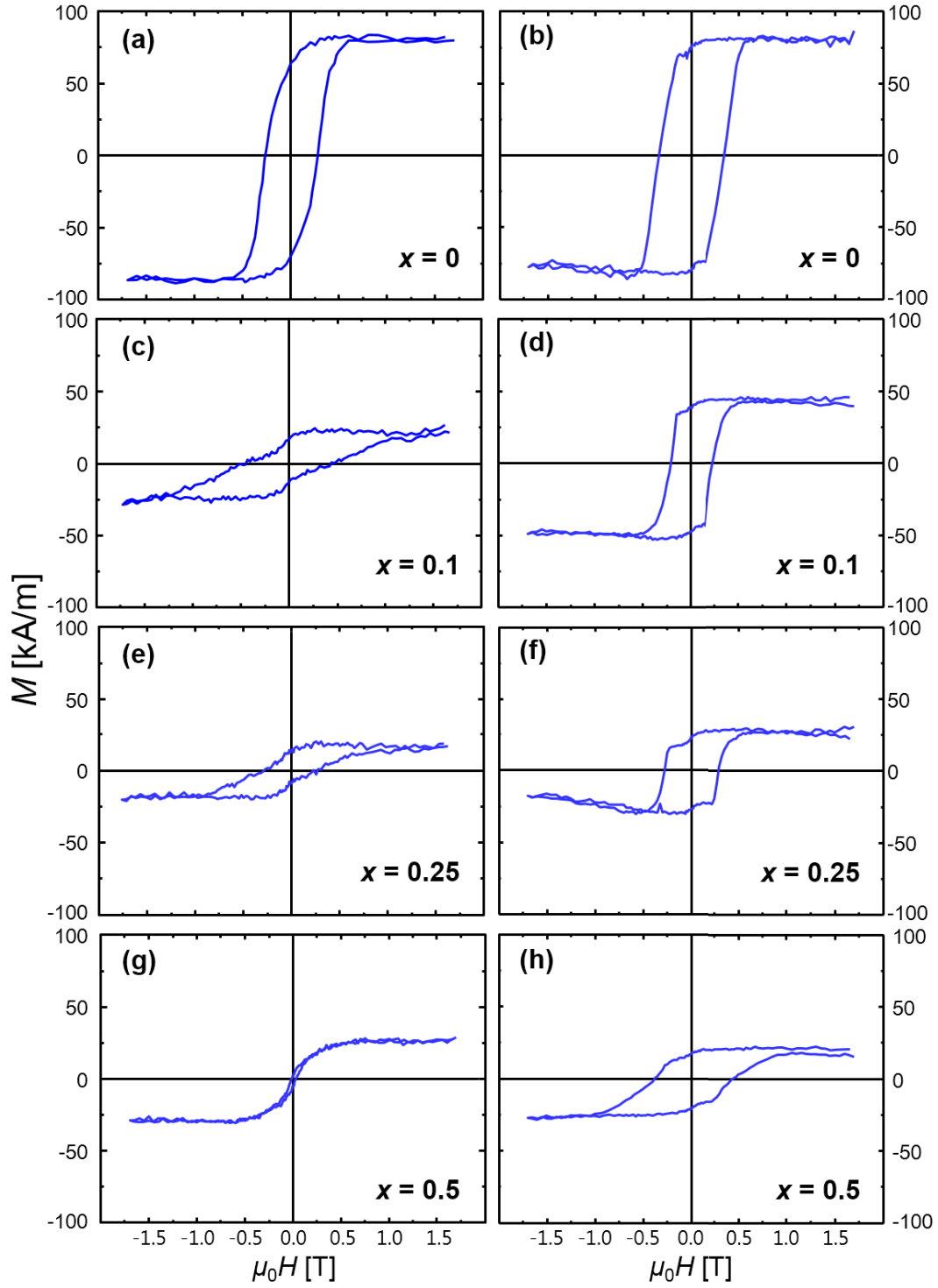


Figures 6-2: (a) Out-of-plane and (b) in-plane XRD spectra of Mn_{4-x}Ni_xN thin films grown on STO. The scattering vector of in-plane XRD is along STO [100]. The marks of † and × denote the diffraction peaks from the substrate and from the oxidized phase (MnO), respectively. The in-plane diffraction peaks from Mn_{4-x}Ni_xN are invisible, due to the overlapping with those of STO, which possess a close lattice constant. The insets are RHEED patterns, with the azimuth of electron beam along the STO [100] direction.

6.2. Magnetic and electric properties

6.2.1. VSM characterization

The spontaneous magnetizations have been measured by VSM. Figures 6-3 show out-of-plane *M-H* loops grown on (a)-(d) MgO¹⁸¹ and (e)-(h) STO substrates, respectively. Table 6-1 and Figure 6-4 presents the *M_S* of each samples, grown on MgO and STO. The reduction of *M_S* has been observed for both kind of substrate. However, the samples grown on STO possess larger *M_S* and a more obvious PMA, resulting in a sharper magnetization switching for the same value *x* of the Ni composition. We attributed these evolutions of the *M_S* and of the *M-H* loops to the differences of the crystalline qualities, due to the evolution of lattice matching, as discussed in chapter 3.



Figures 6-3: Out-of-plane M - H loops of $Mn_{4-x}Ni_xN$ films grown on (a), (c), (e), (g) MgO and (b), (d), (f), (h) STO substrates.

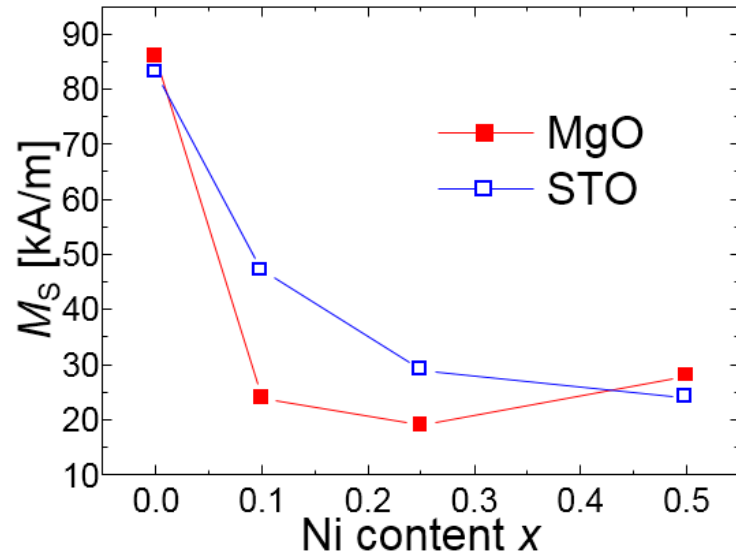


Figure 6-4: Dependence of the spontaneous magnetization with the Ni composition, for thin films deposited on MgO and STO.

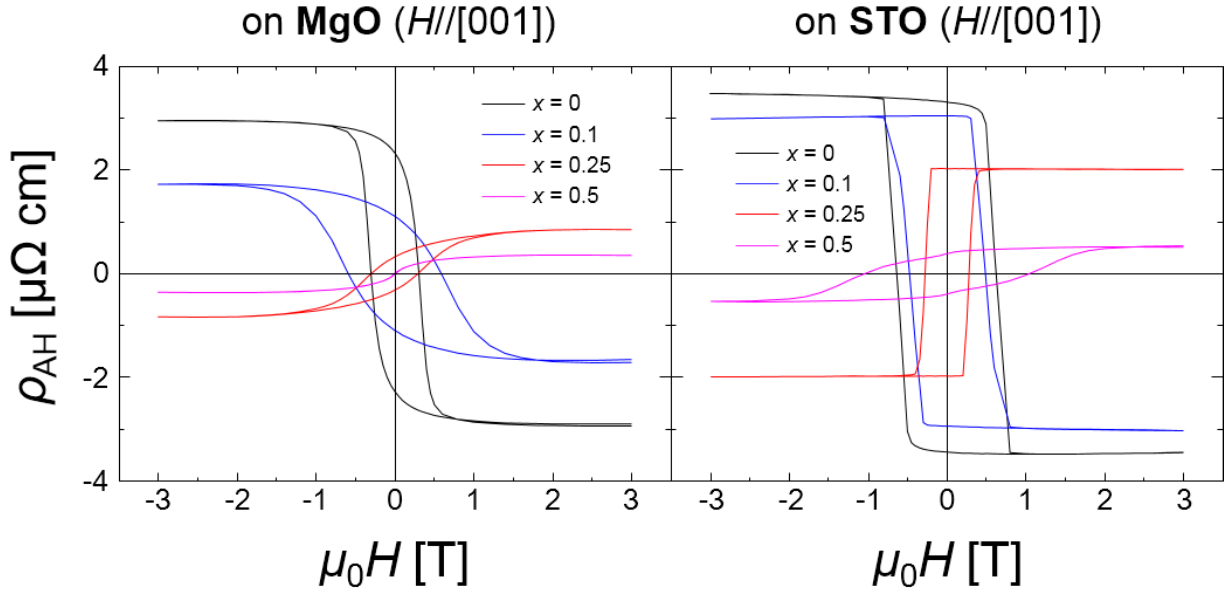
Table 6-1: Spontaneous magnetization M_S [kA/m] of Mn_{4-x}Ni_xN films grown on MgO and STO.

M_S [kA/m]	$x = 0$	$x = 0.1$	$x = 0.25$	$x = 0.5$
MgO	86	24	19	28
STO	83	47	29	24

6.2.2. Magneto-transport properties

Magneto-transport measurement have been performed in a PPMS for both out-of-plane and in-plane fields. Figures 6-5 show the AHE loops of Mn_{4-x}Ni_xN films grown on (a) MgO and (b) STO with out-of-plane magnetic fields. The linear contributions to the voltage due to the magnetic field, which is due to the ordinary Hall effect, has been subtracted from the data.

In chapter 3, we observed differences of remanence ratio M_r/M_S , and of magnetization reversal sharpness between deposits made on MgO and STO substrates. Here, similar results can be observed for $x=0$, 0.1 and 0.25. The sample of composition $x=0.5$ on STO has smooth switching property and not a full remanence, which can probably be attributed to the anisotropy reduction by Ni doping reported in ref. [181]. A very interesting feature is that the sign of anomalous Hall coefficients is reversed between $x = 0.1$ and 0.25.

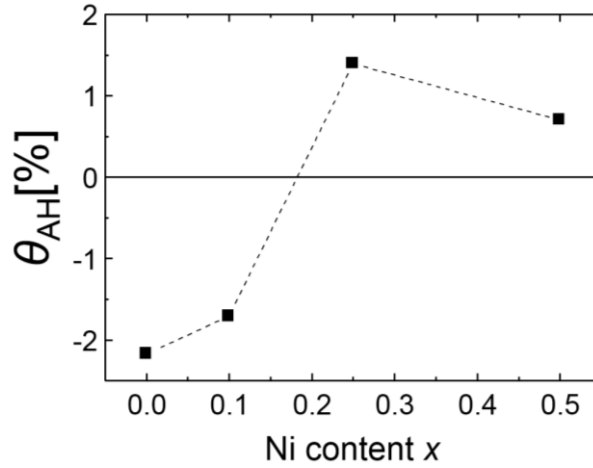


Figures 6-5: AHE hysteresis loops for out-of-plane fields of Mn_{4-x}Ni_xN films deposited on (a) MgO and (b) STO substrates.

Figure 6-6 presents the anomalous Hall angle θ_{AH} for each value of x . θ_{AH} reverses its sign, whereas its amplitude stays relatively high, around 1 %. The sudden reversal of θ_{AH} is probably linked to the ferrimagnetic compensation: at the compensation point, the direction of the magnetic moment at each sublattice is reversed with respect to the external magnetic field. Therefore, this sign reversal is commonly used to confirm the compensation in rare-earth ferrimagnets^{179,182}.

Note however that a sign reversal of the anomalous Hall angle is common in alloys with variation of composition. For instance, in Mn₄N-based materials, we recently investigated the magneto-transport properties of Mn_{4-x}Fe_xN thin films¹¹⁸, whose AHE angle is also been reversed around $x = 1$ (though it loses the perpendicular magnetization). The variation of ρ_{AH} is almost linear with x at 300K, because of the shift of the Fermi level E_F and of variation of the exchange coupling splitting energy¹⁸³ caused by Fe doping. Meng *et al.* also reported the sign reversal of the AHE in Mn_{4-x}Dy_xN thin films for $x=0.08$ and 0.2 ¹⁸⁴, and have concluded that it is caused by a change of band structure and of the position of the Fermi level.

In the Mn_{4-x}Ni_xN system studied here, the sign reversal is caused by a small amount of Ni and the sign change is quite sharp when varying the Ni content, which is different from the smooth case of Fe substitution. Therefore, we expect that this reversal is due to the crossing of the compensation composition. Moreover the amplitude of the AHE is not much affected, thus pointing more to this scenario than a change in the band structure. The next section focuses on several measurements made in order to reveal the compensation mechanism.

Figure 6-6: AHE angles θ_{AH} of Mn_{4-x}Ni_xN for several Ni compositions x .

In-plane AHE measurement have been also performed, similarly to what has been done in chapter 3. Figure 6-7 presents the normalized in-plane magnetizations under in-plane magnetic field, for samples grown on STO substrates. The anisotropic field H_K drastically increases up to 8 T at $x = 0.25$, while the sample of $x = 0.5$ has a weaker anisotropy, which is consistent with the non-full remanence observed in the out-of-plane hysteresis. The anisotropic energy K_u has been calculated by integration, and the results are shown in the Table 6-2. While the anisotropy constant K_u of samples deposited on MgO suddenly decreases as Ni is introduced, those on STO keep a strong anisotropy up to $x = 0.25$.

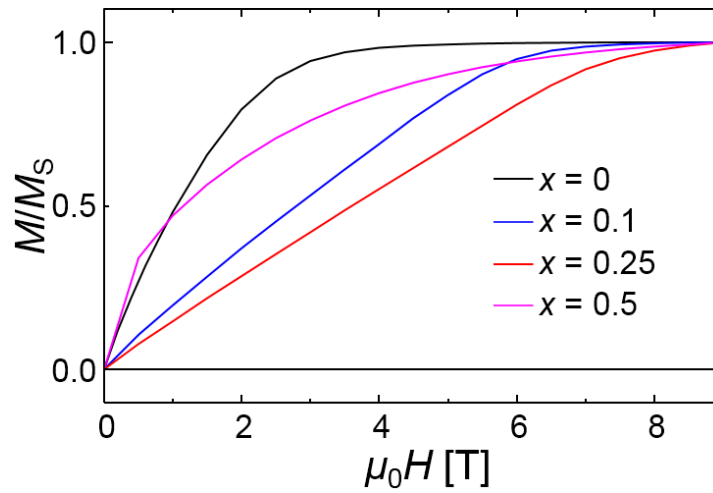


Figure 6-7: In-plane hysteresis loops measured by AHE for samples of STO substrates.

Table 6-2: Magnetic anisotropy constant K_u for each Ni composition and substrate.

K_u [MJ/m ³]	$x = 0$	$x = 0.1$	$x = 0.25$	$x = 0.5$
MgO	0.06	0.03	0.01	isotropic
STO	0.11	0.14	0.11	0.04

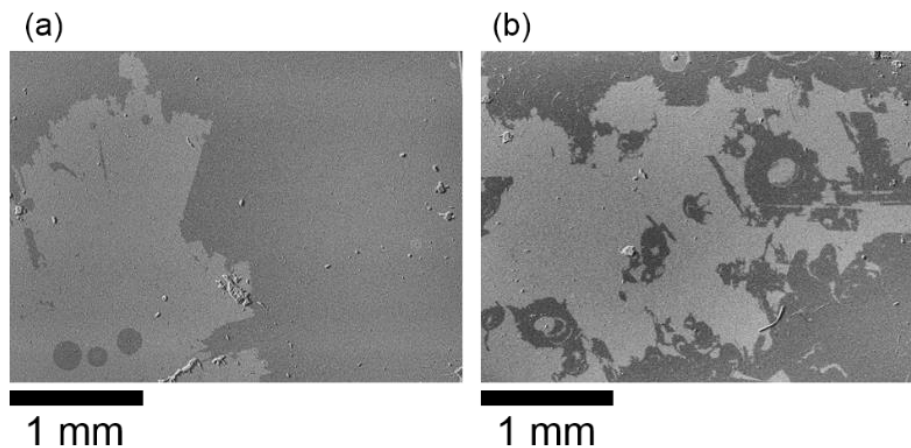
Hereafter, we focus on only the samples for $x=0, 0.1,$ and 0.25 on STO which keep good qualities and

cross the point of the sign reversal of AHE.

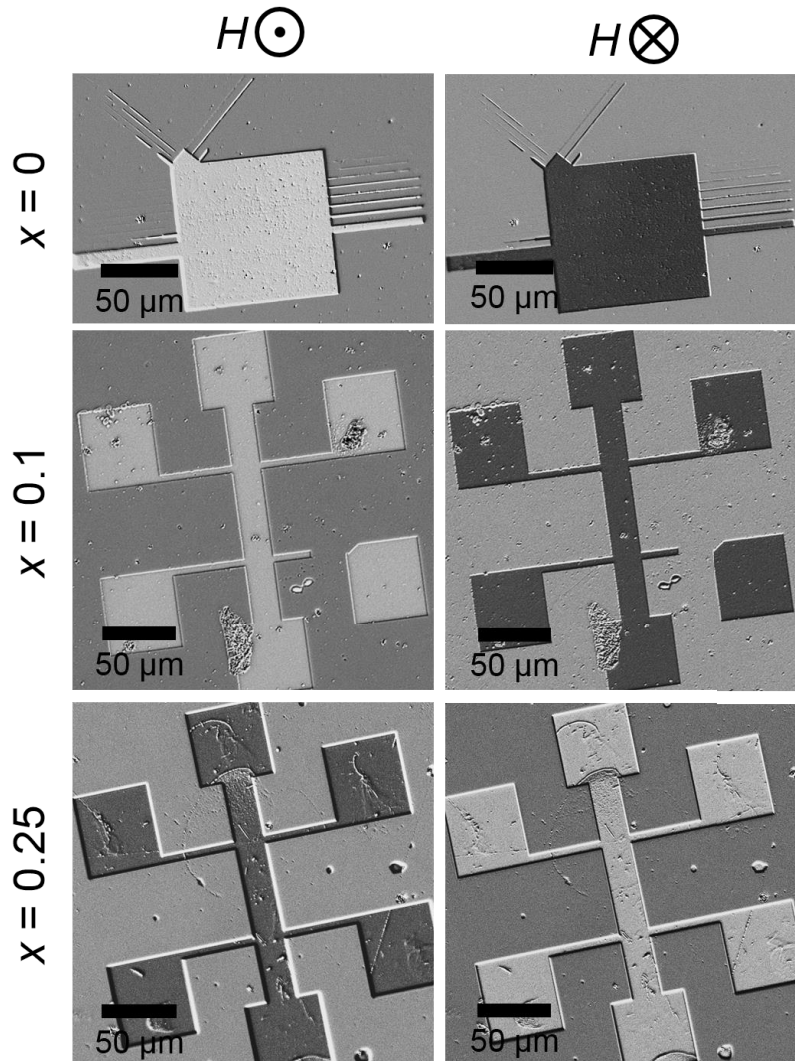
6.2.3. MOKE observation of the domain structure and sign of the MOKE signal

After a partial magnetization reversal process similar to that of chapter 3, the domain structures have been observed by MOKE microscopy. Figures 6-8 present the MOKE images of Mn_{4-x}Ni_xN films on STO for $x = 0.1$ and 0.25 . Both samples possess millimeter-sized domains, like pure Mn₄N films. This result is consistent with the result of AHE measurement, which shows full remanence and sharp switching caused by the strong anisotropy, and by the scarcity of DW pinning sites and domain nucleation centers. Similarly to Mn₄N/STO samples, Mn_{4-x}Ni_xN films grown on STO constitute a promising material for CIDWM applications.

Figures 6-9 show the differential MOKE images of the samples on STO after fabrications into device structure, between before and after magnetic field pulse to saturate magnetization. Interestingly, the Kerr rotation angle has been reversed between $x = 0.1$ and 0.25 , similarly to the AHE angle. The reversal of the MOKE signal is also employed to confirm magnetization compensation⁹⁷, so that this result comfort the hypothesis of a compensation concentration in-between $x = 0.1$ and 0.25 .



Figures 6-8: The MOKE images at $x =$ (a) 0.1 and (b) 0.25 after partial reversal process.



Figures 6-9: Differential MOKE images of microstructures after saturation by magnetic field pulses for each H -direction and Ni-content x .

6.3. Temperature dependence of the magnetic and magneto-transport properties

6.3.1. Magnetization at low temperature

Magnetization and magneto-transport measurements have also been performed at low temperature by VSM-SQUID. Figure 6-10 shows the M - T curve of Mn_{4-x}Ni_xN samples grown on STO. The measurements have been performed in MPMS 3 under a magnetic field of 0.1 T. The M - T trends of pure Mn₄N and $x = 0.1$ samples are the same, with a M_S increasing at low temperature, while a decrease is observed for $x = 0.25$, after a slight increment of M_S . Such behaviors have already been reported more than a half century ago by Mekata¹⁸⁵. He introduced In and Sn into Mn₄N powder samples, and measured the M - T curve using a magnetic torsion balance. In the Mn_{4-x}(In or Sn)_xN systems, he found a linear reduction of M_S with the composition x , and attributed it to the ferrimagnetic compensation from the two sublattice. Note that he explained that the origin of compensation is the variation of the Fermi level, leading to a change of the magnetic moment of Mn atoms, since neither In nor Sn is a magnetic element. In the report, this specific M - T curve has been obtained above compensation composition, shown in Figures 6-11, which is similar to Mn_{3.75}Ni_{0.25}N samples. The simplified M - T curves quoted from ref.

[185] are shown in Figures 6-12. The hypothesis is that the magnetic moment at the I-site (μ_I) rises at low temperature faster than that at the II-site (μ_{II}). Therefore, below compensated states where μ_I dominates the total magnetization ($\mu_I > \mu_{II}$), M_S monotonically increases as the temperature decreases. On the other hand, above the compensation composition, μ_{II} dominates the total magnetization, and the $M-T$ curve possesses a more complicated shape at low temperature. Thus, the shape of the $M-T$ curve of Mn_{3.75}Ni_{0.25}N samples can be attributed to the fact that the Ni concentration is above the compensation concentration.

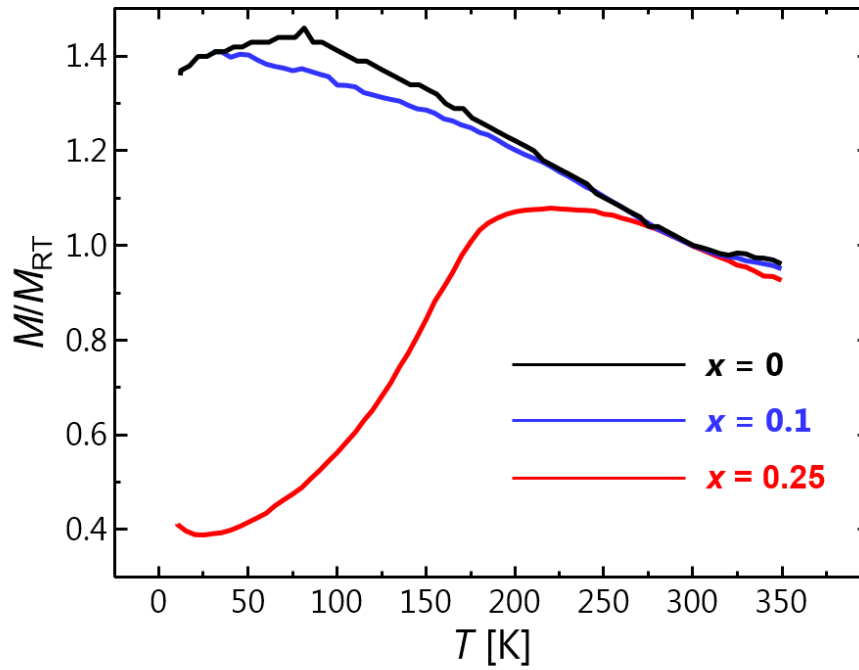
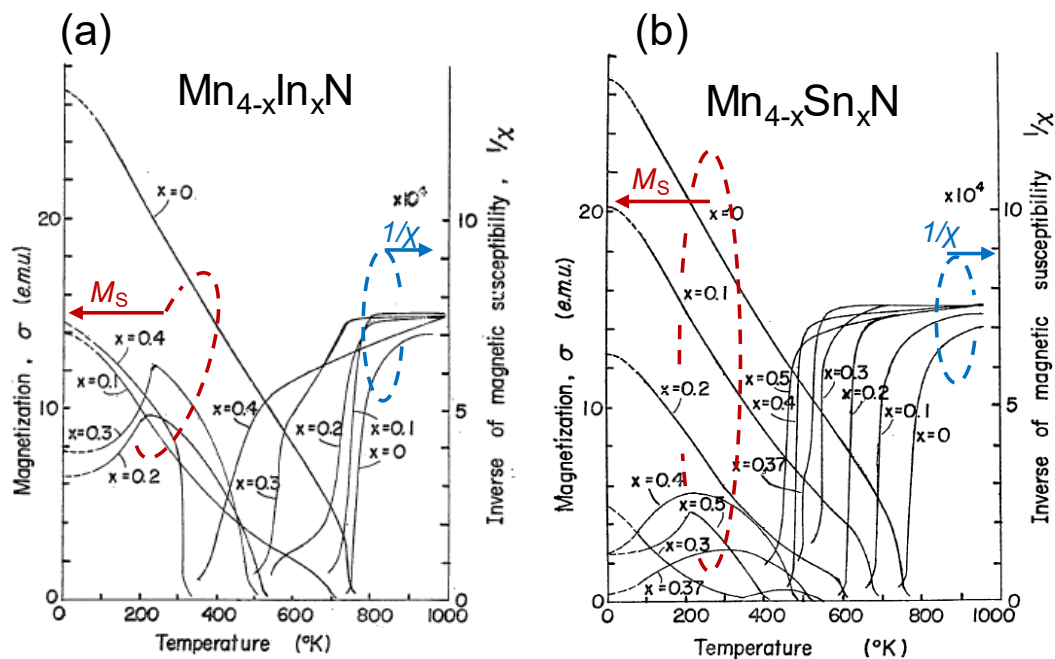
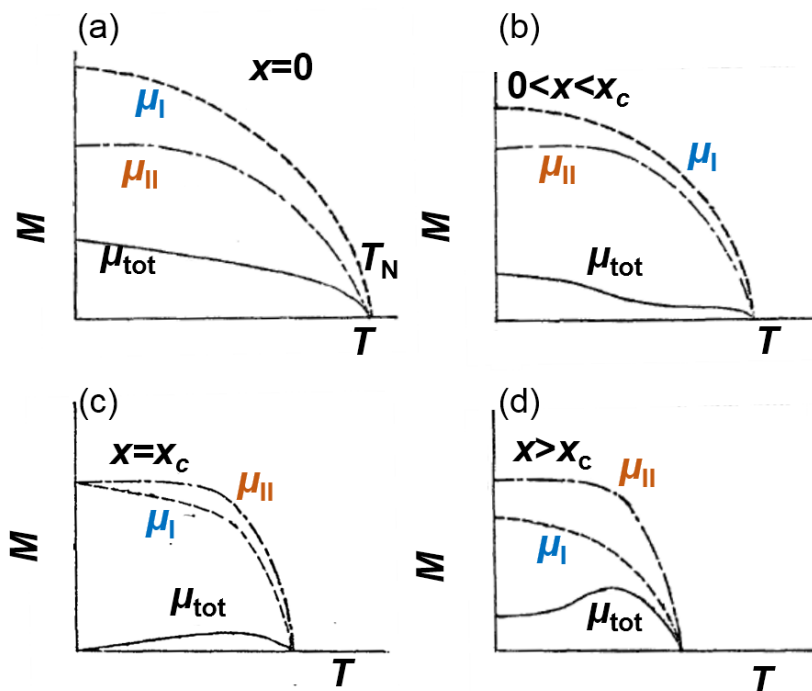


Figure 6-10: Temperature dependence of the spontaneous magnetization in Mn_{4-x}Ni_xN films.



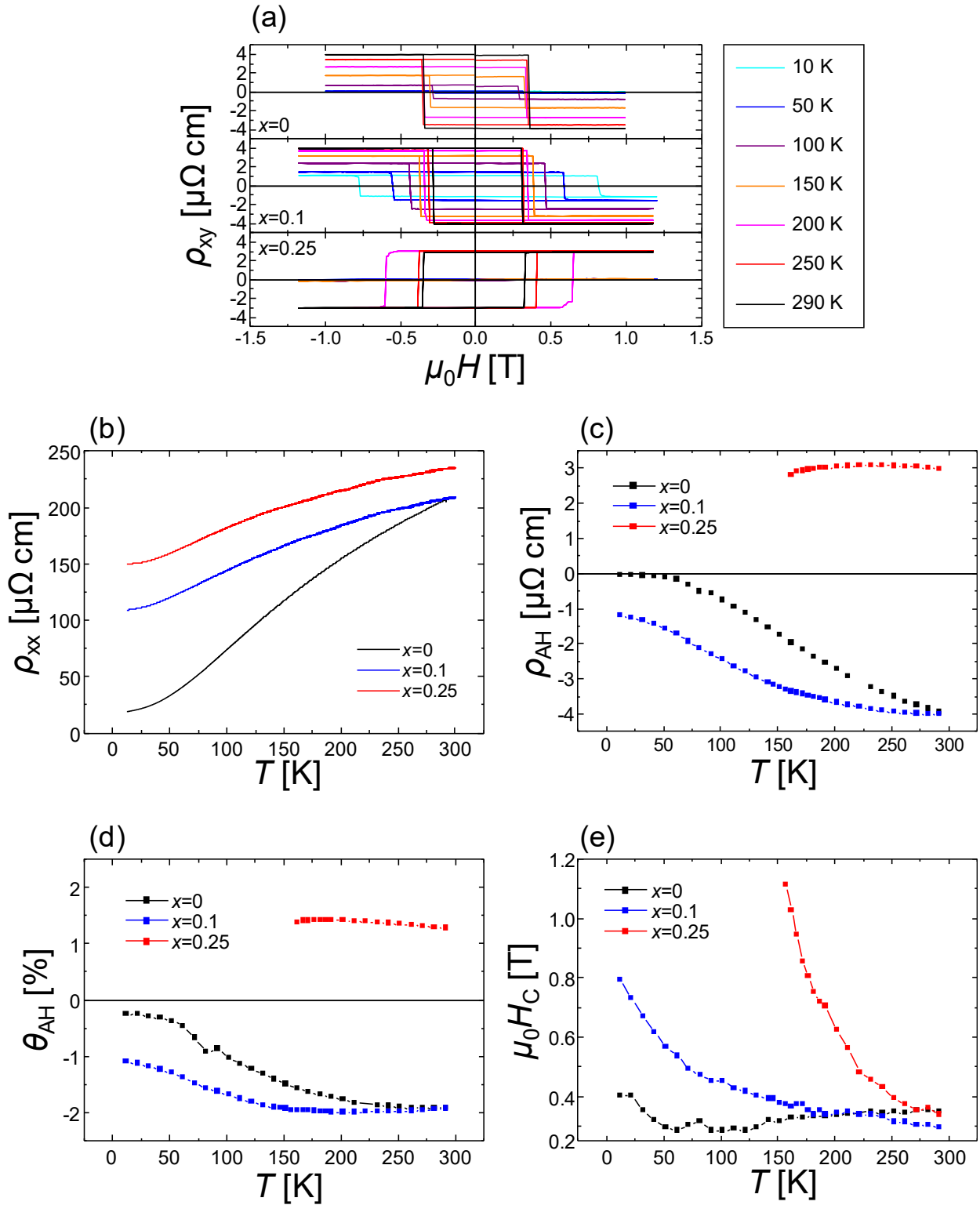
Figures 6-11: Temperature dependence of the magnetization ($T < T_N$) and of the susceptibility ($T > T_N$) in (a) $Mn_{4-x}In_xN$ and (b) $Mn_{4-x}Sn_xN$ powders¹⁸⁵. The left (right) curves correspond to spontaneous magnetization M_S (inverted susceptibility $1/\chi$). Above compensation, M - T curves are bended in (a) $x = 0.2, 0.3$ and (b) $x = 0.4, 0.5$.



Figures 6-12: Temperature dependence of the magnetization in $Mn_{4-x}(In \text{ or } Sn)_xN$ films¹⁸⁵ for (a) pure Mn_4N ($x = 0$), (b) under compensation ($x < x_c$), (c) just compensated at 0 K ($x = x_c$), and (d) over compensation ($x > x_c$). T_N and x_c are the Néel temperature and the compensation composition at 0 K.

6.3.2. Magneto-transport properties at low temperature

Magneto-transport measurements have been performed in a helium-free cryostat equipped with electrical contacts, after a nanofabrication process into Hall bars. Figures 6-13 (a) presents the hysteresis loops of Mn_{4-x}Ni_xN ($x = 0, 0.1, 0.25$) at several temperatures. The temperature dependence of each property is summarized in Figures 6-13, with the evolutions of properties such as (b) the longitudinal resistivity ρ_{xx} , (c) the anomalous Hall resistivity ρ_{xy} , (d) the anomalous Hall angle θ_{AH} , or (e) the coercivity H_C obtained from AHE loops. The trends of ρ_{xx} , ρ_{AH} , and θ_{AH} are similar to those observed in Mn_{4-x}Fe_xN alloy¹¹⁸: a drastic decrease with the temperature for the pure composition ($x = 0$), while alloying weakens the temperature dependence of ρ_{xx} and ρ_{xy} , and keeps θ_{AH} nearly independent of the temperature for $x = 0.25$. Note that such a temperature-independent anomalous Hall angle could be applicable to AHE-based devices requiring a relatively high θ_{AH} and a wide working temperature range. The coercivity H_C diverged at low temperature only in Mn_{3.75}Ni_{0.25}N sample, which can be attributed to the M_S reduction, as demonstrated in the Figure 6-10. Note that this kind of divergence of H_C is also utilized to confirm the compensation point¹⁷⁹, even though the composition $x = 0.25$ has no actual compensation temperature, and that H_C just exceeds the maximum field to be applied in our system. We expect that intermediate compositions ($0.1 < x < 0.25$), which are slightly more Ni-rich than the compensation composition at room temperature, should possess a compensation temperature.



Figures 6-13 (a): AHE hysteresis loops for compositions $x=0, 0.1$ and 0.25 , at several temperatures. (b)-(e): Temperature dependence of (b): the longitudinal resistivity ρ_{xx} , (c): anomalous Hall resistivity ρ_{AH} , (d): anomalous Hall angle θ_{AH} , and (e): coercivity H_C in Mn_{4-x}Ni_xN films.

6.4. Hypothesis of compensation by Ni atoms

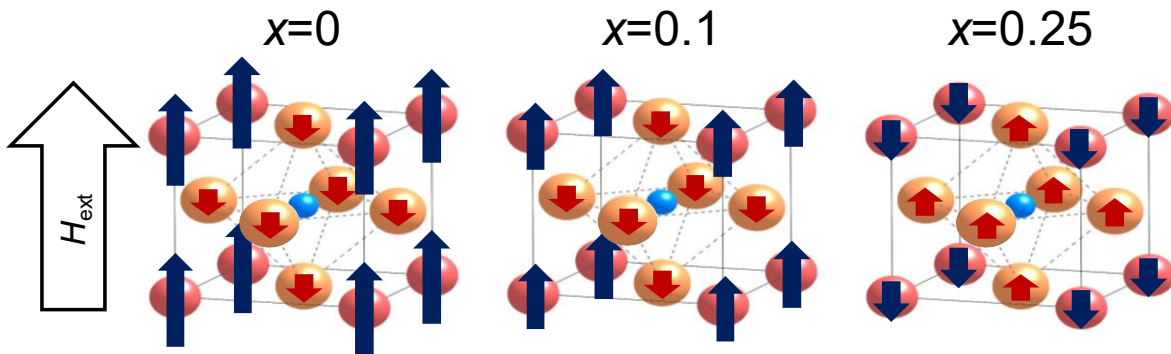
Let us assume a mechanism of compensation in the Mn_{4-x}Ni_xN system, with 2 hypotheses, *i.e.*

1. The magnetic moment of Ni atoms μ_{Ni} should be smaller than that of Mn atom μ_{Mn} , as predicted by the Slater-Pauling curve^{186,187} ($1 \mu_{\text{B}}$ for Mn and $0.6 \mu_{\text{B}}$ for Ni).
2. Most Ni atoms are substituted to Mn atoms at the I-site of the Mn₄N lattice, as expected from site-resolved evaluations by X-ray Magnetic Circular Dichroism (XMCD) of Fe_{4-x}Ni_xN alloy, where Ni atoms have been positioned at the corner site¹⁸⁸. Also, practically, only substitution of I-site Mn atoms, with smaller magnetic moment, enable compensation in Mn₄N-based system.

Using these hypotheses, the total magnetic moment μ_{tot} is derived as,

$$\begin{aligned} \mu_{\text{tot}} &= |\mu_{\text{I}} - 3\mu_{\text{II}}| \\ \mu_{\text{I}} &= (1-x)\mu_{\text{Mn,I}} + x\mu_{\text{Ni}} \\ \mu_{\text{II}} &= \mu_{\text{Mn,II}} \end{aligned} \quad (6-1)$$

where $\mu_{\text{Mn,I}}$ and $\mu_{\text{Mn,II}}$ are estimated to be $3.53 \mu_{\text{B}}$ and $-0.89 \mu_{\text{B}}$, respectively, from the results of neutron diffraction measurements¹⁰⁷. However, these values are obtained for powder samples, whose magnetic properties are slightly different from those of our thin films. Therefore, $\mu_{\text{tot}}(x=0)$ does not correspond to the experimentally measured value of M_{S} of 83 kA/m. Here, we normalized $\mu_{\text{Mn,I}}$ and $\mu_{\text{Mn,II}}$ to retrieve the experimental value: $\mu_{\text{Mn,I}} = 2.13 \mu_{\text{B}}$ and $\mu_{\text{Mn,II}} = -0.54 \mu_{\text{B}}$. Actually, Ni introduction also reduces the Néel temperature, so that M_{S} can also be reduced independently from the substitution of magnetic moments described above. Therefore, we will discuss only Ni-poor compositions of $x = 0, 0.1$ and 0.25 in this simple compensation model. Figures 6-14 display the crystalline structures and estimated magnetic moments for $x = 0, 0.1$ and 0.25 . Only at $x = 0.25$, the II-site dominates total magnetization.

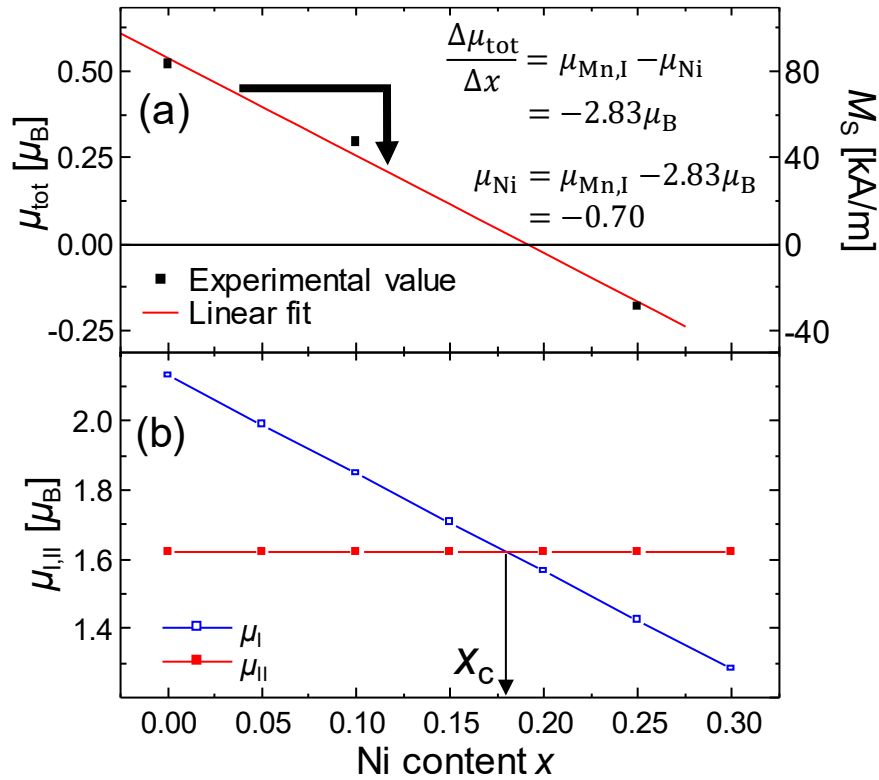


Figures 6-14: Ferrimagnetic arrangement of the magnetic moments in Mn_{4-x}Ni_xN samples for three different Ni concentrations x which is applied an external field in the up direction.

Figures 6-15 show the (a) experimentally obtained M_{S} and calculated values of μ_{tot} with the corresponding M_{S} , and (b) the estimated μ_{I} and μ_{II} , for each Ni content x . The value of μ_{Ni} can be derived from the linear fit of the $\mu_{\text{tot}}-x$ curve. From the eqs. (6-1), the slope of $\mu_{\text{tot}}-x$ plot is equal to $\mu_{\text{Ni}}-\mu_{\text{Mn,I}}$. As a result, μ_{Ni} can be estimated to be $-0.7 \mu_{\text{B}}$. This magnitude is not so far from the prediction from the Slater-Pauling curve. Such a negative value means that the magnetic moments of Ni atoms are parallel to that of the II-site Mn atoms and

anti-parallel to that of I-site Mn atoms. The compensation composition x_c can also be estimated to be around $x = 0.18$.

Of course, the possibility that the compensation has been caused not by the substitution of magnetic moments, but by variations of the band structure and of the Fermi level cannot be completely ruled out. Now, we have already found similar results in the Mn_{4-x}Co_xN system, and revealed the individual moment at each site and the ferrimagnetic arrangement by X-ray magnetic circular dichroism (XMCD) measurement¹⁸⁹. The XMCD and Nuclear Magnetic Resonance (NMR) measurements for Mn_{4-x}Ni_xN samples are scheduled to characterize the magnetic moment for each site. In parallel, first principle calculations are also under progress.



Figures 6-15 (a): Calculated Ni-content dependence of μ_{I} and μ_{II} in our model. The data point after compensation ($x=0.25$) is plotted as a negative value. From the linear fitting, μ_{Ni} has been estimated.

(b): Calculated x -dependence of μ_{I} , μ_{II} . The x_c denotes the compensation composition at room temperature.

Chapter 7 Total summary and prospects

My thesis focused on the potential of Mn₄N as a new material for spintronics applications. The obtained results and the most significant contributions can be summarized as follows:

Substrate dependence of the magnetic properties

The basic magnetic and magneto-transport properties of Mn₄N thin films deposited on either MgO or STO have been measured. I showed that a dramatic improvement can be obtained by replacing conventional MgO substrates by STO substrates. The Mn₄N/STO system exhibits astonishing properties: a millimeter-sized domain structure, a fully remnant magnetization, and a sharp magnetization switching caused by scarce nucleation and smooth DW propagation. These properties, associated to a very small M_S and a PMA large enough to induce perpendicular magnetization, underline its potential for spintronic applications.

We are now attempting to grow Mn₄N thin films on several other substrates possessing lattice parameters close to Mn₄N, such as MgAl₂O₄, LaAlO₃, (LaAlO₃)_{0.3}(SrTaAlO₆)_{0.7} (LSAT), and some perovskite oxides, to explore the best substrate for the growth of Mn₄N thin films.

STT efficiency measured by DC

Magneto-transport measurements have been performed using Hall-bars to observe CIDWM using DW in Mn₄N. We showed that DC can prevent field-driven DW motion, thus increasing the coercivity of Hall crosses. We also demonstrated DW depinning from a notch and subsequent CIDWM by DC, in absence of magnetic field. The STT efficiency, derived from the equivalency between DC and external fields, is found to be of 7×10^{-12} T.m²/A, with a threshold current density for DW motion of 1.2×10^{11} A/m². This type of experiments could be further used get some insight into the temperature dependence of the STT.

DW speed in Mn₄N using current pulses

The efficiency of the STT in Mn₄N thin films has also been evaluated by measuring the speed of DWs driven by current pulses. The DW velocity reaches record values of 900 m/s for a current density of 1.3×10^{12} A/m² at room temperature. This value is the highest in all STT-driven systems, and is comparable to the highest speeds obtained using SOTs. The DW mobility η derived from the slope of the $v_{DW}-j$ curve is also very large (7.1×10^{-10} m³/C), the highest in all STT-based systems. Fits of our data using a 1D analytical model allows extracting a spin polarization of the conduction electrons of 0.75 ± 0.05 , suggesting that Mn₄N could be suitable to obtain large magnetoresistances.

Measurements of CIDWM in Mn₄N microstrips have been scheduled with much longer current pulses (typically 1 μ s), in order to observe the effects of the STT in the creep regime. In order to reduce the threshold current density for CIDWM, we are also working on adding SOTs, using current pulses on DWs and harmonic Hall measurement¹⁹⁰ in a W/Mn₄N/STO structure. We also envision checking the spin polarization using GMR measurements in lateral spin valves¹⁹¹ and spinmotive force measurements¹⁹².

Magnetic properties of $\text{Mn}_{4-x}\text{Ni}_x\text{N}$ films

Ni-introduction induces a reduction of the spontaneous magnetization, while preserving the perpendicular magnetic anisotropy and the full remanence. Our results evidence the possibility of finding a compensation composition for ferrimagnetic Mn_4N -based systems. Three results are indication that this point has been crossed: the reversal of the anomalous Hall angle, the Kerr rotation chirality, and the temperature dependence of the magnetization. We proposed a compensation model of Mn_4N by Ni introduction which is consistent with the M_S reduction, the reversal of AHE, the Kerr and the $M-T$ curves. The compensation composition x_c has been estimated to be around $x=0.18$.

We are currently trying to resolve magnetic moments at different sites, using techniques such as XMCD and NMR. First principle calculations are also in progress to explore the electronic structure of $\text{Mn}_{4-x}\text{Ni}_x\text{N}$ samples, such as the magnetic moments for each sublattice and atom, and the spin polarization of the density of states. We will also perform CIDWM measurements in these samples, similarly to what has been done in chapter 5.

Impact of this work

The amazing properties of Mn_4N for CIDWM are particularly interesting because they can be obtained without any rare earth elements, stack structures, nor external assistance such as magnetic/electric field or mechanical stress. These results have obviously revealed the potential of Mn_4N thin films as a new spintronic material consisting of only cheap elements and indicated that STT-driven CIDWM technique still remains competitive with SOT. We hope that it will be considered as milestone, and because it may lead to solve the problems concerning material criticality such as a supply risk and sustainability.

Acknowledgement

This thesis and all experimental results have been completed thanks to a lot of supports. Here, I acknowledge all of them such as supervision of my Ph. D course, technical advice, research funds and equipment for experiments.

Supervision

My research activities in PhD course has been supervised by by Prof. Takashi Suemasu in university of Tsukuba (UT), and Dr Olivier Fruchart, Dr. Jean-Philippe Attané, Dr. Laurent Vila in Spintec, CEA-Grenoble, for discussing the direction of my research, writing papers, brushing up presentations, and admission processes for the universities. In particular, the double degree program (DDP) between UT and Université Grenoble Alpes (UGA), which I belong to, needed a lot of complicated processes. Thank you very much for supporting and leading me. I also acknowledge Prof. Akimoto and Prof. Etienne Gheeraert who are in charge of DDP and secretaries in UT, UGA and CEA.

Technical advice and experimental support

In Japan, I have been given lots of advice from Prof. Suemasu and Assoc. Prof. Toko for the growth and characterization technique of crystalline thin film by MBE. Prof. Mitani in National Institute for Material Science (NIMS), Prof. Yanagihara and Prof. Ohno in UT provided me kind advice and feedback of my research in several check points in my PhD course and especially in the pre-defense. Dr. Isogami in NIMS and has contributed to specialized physics to our material, ferromagnetic nitrides. Assistant Prof. Ito in Tohoku University also gave me kind advice and taught me how to manage researching since I was an under graduate student.

In France, lots of researchers in Spintec and Institut Néel contributed to my research. In addition to my supervisors, Dr. Fruchart provided me many hints to brush up my thesis and presentation slideshows. Dr. Attané revised my manuscripts, papers for journal and this PhD theses, etc and often discussed the experimental results and the schedules. Dr. Vila took care of my life in Grenoble, from the viewpoints of not only research but also in private. He also performed all nanofabrication process of blanket layers. Dr. Alain Marty in Spintec helped me to evaluate the crystalline qualities. Dr Stéfania Pizzini and Dr. Jan Vogel in Institut Néel is owed to many experiments to observe domain configuration, measure DW speed and magnetization, and gave me lots of kind advice. Nicolas Thiery, Paul Noël, Thomas Guillet in Spintec and Matic Klug in Kiel university, PhD students, helped me to operate equipment for experiments. José Pena-Garcia performed micromagnetic simulations instead of me and discussed the results.

Research fund

This work was supported in part by JSPS Grants-in-Aid for Scientific Research (A) (No. 26249037) and JSPS Fellows (Nos. 16J02879). As supports for flight fee and accommodation, the fund from the “Tsukuba resonance education program” and double degree program contributed to my research abroad. Support from the ANR OISO and Laboratoire d'excellence LANEF in Grenoble (ANR-10-LABX-51-01) are also acknowledged.

Equipment for experiments

Magnetization measurements have been performed with the help of Professor H. Yanagihara of the University of Tsukuba and with the help of Dr. Vogel in Institut Néel. Magneto optical Kerr effect imaging has been performed with the support of Dr. Pizzini in Institut Néel. The pulse generator for CIDWM experiments is attributed to Dr. Mihai Miron in Spintec. MFM tips have been contributed by Simon Le Denmat, from Institut Néel. Nanofabrication process has been held in PTA in Grenoble with great support of Dr. Vila.

Special thanks

My life as a PhD student in Japan and France has been realized owing to many kind supports concerning not only research, but also daily life. I have been indeed fortunate to meet such kind people.

Prof. Takashi Suemasu has given me a lot of advice, good environment and opportunities for research and learning, such as JSPS fellowship program and double degree program in PhD years. Without you, I would never choose PhD course.

Dr Laurent Vila is one of the best benefactors in my French student life. Thank you very much for not only scientific advice, but also taking care of my accommodation and funding process, etc. Please also say hello to your wife, Hanako.

Dr. Jean-Philippe Attané taught me physical theory to discuss my experimental results and brushed up my English writing. You are the best contributor to this thesis.

Dr. Olivier Fruchart managed my admission process to UGA, thank you very much.

Associate prof. Toko in UT taught me the attitude as a young researcher. Thank you very much.

As senior students, assistant prof. Ito, Mr. Sanai and Ms. Yasutomi taught me how to manage research life in Suemasu-lab. In particular, Ito-san often took care of my laboratory life and served me such a great scientific topic. Thank you very much.

As junior students, Mr. Higashikozono, Mr. Takata, Mr. Anzai, Mr. Komori and Mr. Hirose helped my experiments and lots of discussion, and activated me by their own attitude for research. Thank you very much.

Owing to all members in Suemasu-laboratory, I could enjoy my student life in Tsukuba, such as recreations. Thank you very much.

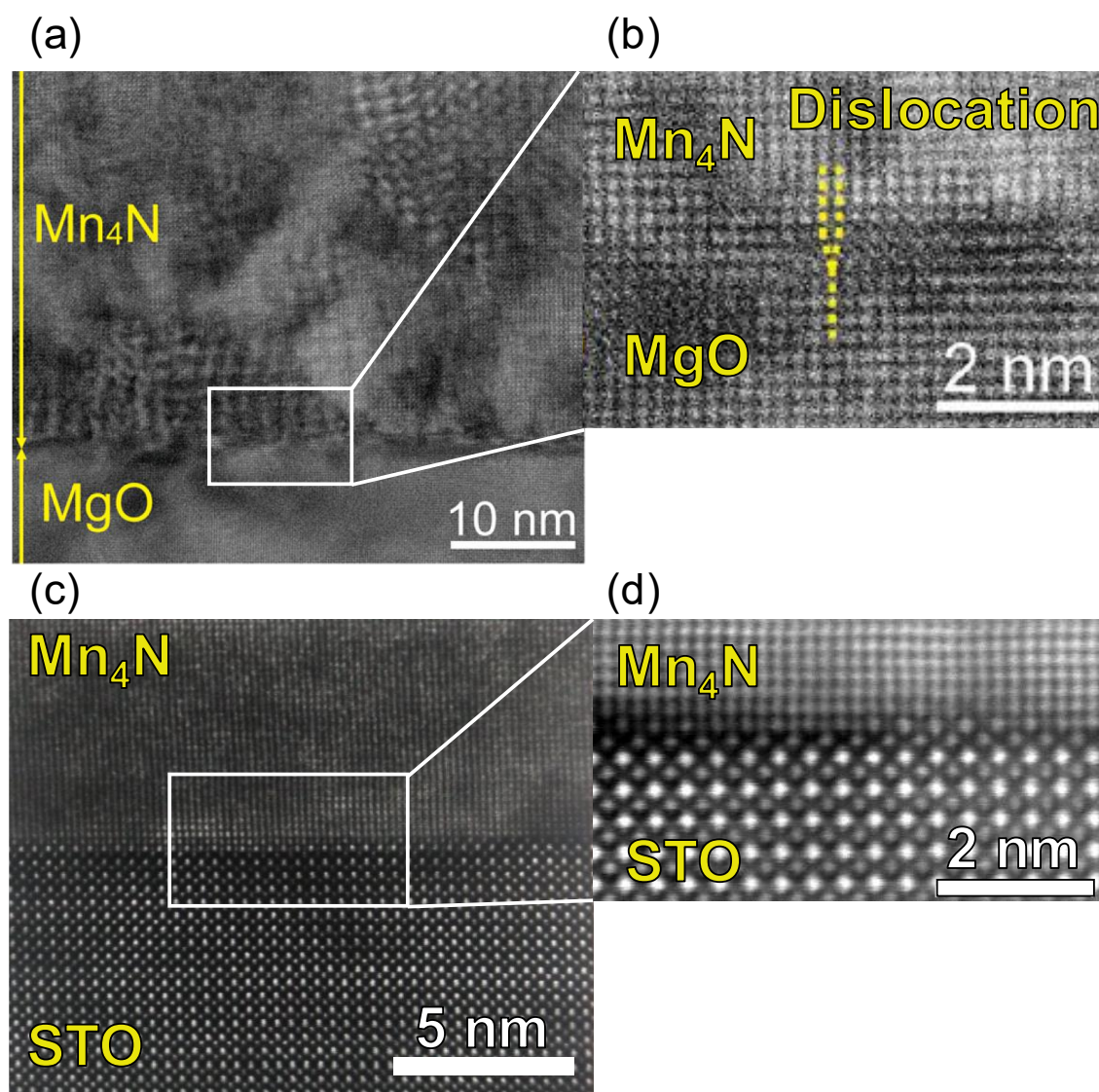
In France, thanks to many friends in laboratory and Japanese community, I could enjoy my first long stay in foreign country and expand my friendship network. Thank you very much.

Finally, thank you very much my parents, for growing me and supporting my student life.

Appendix

Cross-sectional TEM observation of Mn₄N/STO interface

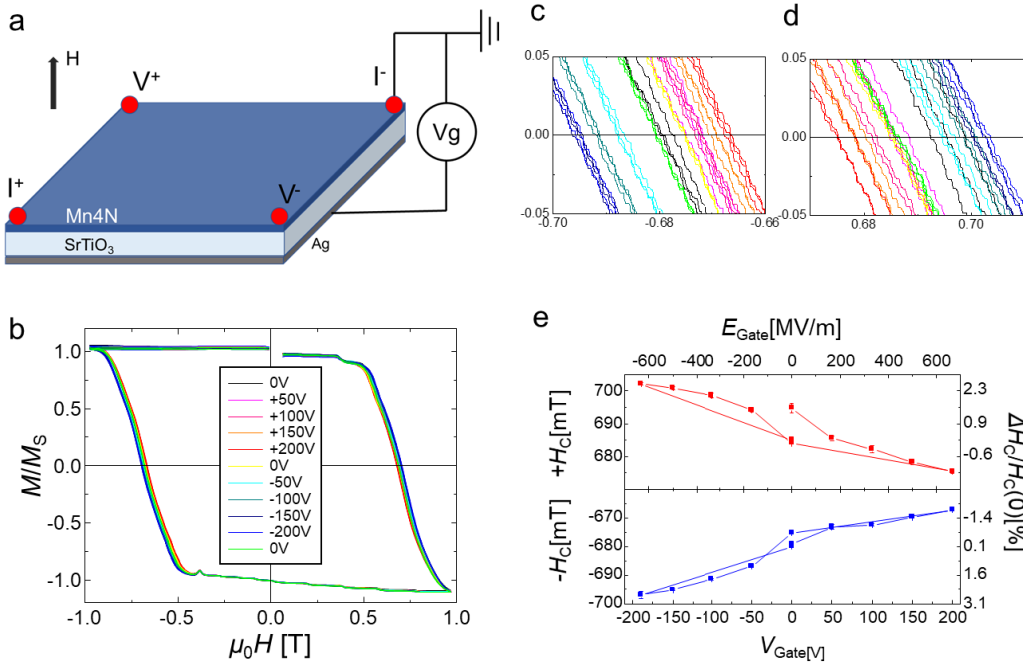
In chapter 3, we have suggested that the difference of magnetization reversal properties between MgO and STO substrate should be caused by dislocations at the interface. Therefore, we have performed cross-sectional TEM observation to examine this assumption and compare the Mn₄N/STO sample with Mn₄N/MgO, reported in ref. [114]. Figures A1 present cross-sectional TEM images of (a, b) Mn₄N/MgO and (c, d) Mn₄N/STO. While the moiré fringes in Fig. A1 (a) suggest the presence of misfit dislocation in Mn₄N film on MgO as shown in Fig. A1 (b), Mn₄N/STO sample has shown no dislocations in long-range area indicating extremely good crystalline quality. Consequently, we have successfully revealed the amazing quality of the Mn₄N thin film grown on STO(001) substrate.



Figures A1: Cross-sectional TEM images of Mn₄N thin films grown on (a), (b) MgO¹¹⁴ and (c), (d) STO substrates. (b) and (d) are magnified views near the Mn₄N/substrate interfaces. Yellow dashed lines in (b) denote a misfit dislocation.

Voltage control of magnetic anisotropy

As an appendix, we would like to address the properties concerning the effect of the electric field on the anisotropy of the Mn_4N layer. A back-gate voltage was applied to the bottom of the 300 μm STO substrate, while measuring the coercivity of a 4.4 nm-thick Mn_4N layer with a magnetic field. The measurements were performed at 10 K, so that the dielectric constant of STO reaches very high values ($\sim 3 \times 10^4$). The experimental geometry and results are shown in Figs. A. The gate voltage acts on both the negative and positive parts of the magnetic hysteresis, the coercivity varying linearly with the applied voltage. By assuming that the coercivity variations correspond to variations of the anisotropy energy, the efficiency of the electric field effect can be written $\eta = \frac{d(E_k/S)}{dE_{\text{Gate}}} = \frac{E_k/S}{H_C} \frac{dH_C}{dE_{\text{Gate}}}$, where E_k/S is the anisotropy energy per surface, and H_C the coercive field. In our system, η reaches a value of $-15 \text{ pJ.V}^{-1}.\text{m}^{-1}$. This very large efficiency, which could be enhanced by using thinner Mn_4N films, requires further in-depth studies to be understood. Table I compares the values of η obtained in this work with those reported previously. η for our system is negative, much larger than most reports by the order of 1-3, and comparable with Co/Pt system which also utilize the giant dielectric constant of STO at low temperature. In particular, it is possible that a strain-based mechanism adds up to the charge transfer mechanism, due to the STO substrate behavior in the low-temperature tetragonal phase. Whatever the mechanism, this value is up to now only approached in systems with much thinner magnetic layers.



Figures A2: Voltage based modulation of the coercive field of the Mn_4N layers. (a) Schematics of the experiments. A gate voltage is applied to the back of the STO substrate while top electrical contacts arranged in a Van der Pauw configuration are used to measure the extraordinary Hall effect of the Mn_4N layer. (b) Hysteresis loops recorded for various applied back gate voltages. (c) and (d) Zoom of the figure (b) close to the switching fields, for negative and positive applied fields, and using the same color code. (e) Evolution of the coercivity with the applied gate voltage, for both the positive (top) and negative (bottom) half-loops.

Table A: The lists of reported η values with the magnetic layers and dielectric layers.

Magnet	Dielectric	η [fJ/Vm]	Ref
FeCo	MgO	-37.5	193
		-29.2	194
CoFeB	ZrO ₂ /MgO	-33	195
	MgO	-29	196
	Al ₂ O ₃ /MgO	-60	197
Co/Pt	HfO ₂ /MgO	-141~130 (200-300 K)	198
	GdO _x	5000	199
	STO	1300~23100 (2-150 K)	200
Mn ₄ N	STO	-15000(10 K)	This work

List of publications

Papers

1. **T. Gushi**, K. Ito, S. Honda, Y. Yasutomi, K. Toko, H. Oosato, Y. Sugimoto, K. Asakawa, N. Ota, and T. Suemasu, " *Fabrication of L-shaped Fe_4N ferromagnetic narrow wires and position control of magnetic domain wall with magnetic field*, " *Jpn. J. Appl. Phys.* **54**, 028003 (2015).
2. K. Ito, T. Sanai, Y. Yasutomi, **T. Gushi**, K. Toko, H. Yanagihara, M. Tsunoda, E. Kita, and T. Suemasu, " *Mossbauer study on epitaxial $Co_xFe_{4-x}N$ films grown by molecular beam epitaxy*, " *J. Appl. Phys.* **117**, 17B717 (2015).
3. K. Ito, Y. Yasutomi, K. Kabara, **T. Gushi**, S. Higashikozono, K. Toko, M. Tsunoda, and T. Suemasu, " *Perpendicular magnetic anisotropy in $Co_xMn_{4-x}N$ ($x = 0$ and 0.2) epitaxial films and possibility of tetragonal Mn_4N phase*, " *AIP Advances* **6**, 056201 (2016).
4. F. Takata, K. Ito, **T. Gushi**, S. Higashikozono, K. Toko, and T. Suemasu, " *Epitaxial growth and magnetic properties of $Ni_xFe_{4-x}N$ ($x = 0, 1, 3,$ and 4) films on $SrTiO_3(001)$ substrates*, " *J. Appl. Phys.* **120**, 083907 (2016).
5. **T. Gushi**, K. Ito, S. Higashikozono, F. Takata, H. Oosato, Y. Sugimoto, K. Toko, S. Honda, and T. Suemasu, " *Electrical detection of domain wall in Fe_4N nanostrip by negative anisotropic magnetoresistance effect*, " *J. Appl. Phys.* **120**, 113903 (2016).
6. S. Honda, D. Yamamoto, T. Ohsawa, **T. Gushi**, K. Ito, and T. Suemasu, " *Controlling magnetic domain wall positions with an external magnetic field and a low spin-polarized current in chamfered L-shaped ferromagnetic thin ribbons*, " *J. Phys. D: Appl. Phys.* **49**, 385002 (2016).
7. K. Ito, S. Higashikozono, F. Takata, **T. Gushi**, K. Toko, and T. Suemasu, " *Growth and magnetic properties of epitaxial Fe_4N films on insulators possessing lattice spacing near $Si(001)$ plane*, " *J. Cryst. Growth* **455**, 66 (2016).
8. S. Higashikozono, K. Ito, F. Takata, **T. Gushi**, K. Toko, and T. Suemasu, " *Highly oriented epitaxial ($\alpha'' + \alpha'$)- $Fe_{16}N_2$ films on α - $Fe(001)$ buffered $MgAl_2O_4(001)$ substrate and their magnetizations*, " *J. Cryst. Growth* **468**, 691 (2017).
9. F. Takata, **T. Gushi**, A. Anzai, K. Toko, and T. Suemasu, " *Structural characterization and magnetic properties of $L1_0$ - $MnAl$ films grown on different underlayers by molecular beam epitaxy*, " *J. Cryst. Growth* **486**, 19 (2018).
10. A. Anzai, F. Takata, **T. Gushi**, K. Toko, and T. Suemasu, " *Epitaxial growth and magnetic properties of $Fe_{4-x}Mn_xN$ thin films grown on $MgO(001)$ substrates by molecular beam epitaxy*, " *J. Cryst. Growth* **489**, 20 (2018).
11. A. Anzai, **T. Gushi**, T. Komori, S. Honda, S. Isogami, and T. Suemasu, " *Transition from minority to majority spin transport in iron-manganese nitride $Fe_{4-x}Mn_xN$ films with increasing x* , " *J. Appl. Phys.* **124**, 123905 (2018).
12. G. Zahnd, L. Vila, V. T. Pham, F. Rortais, M. Cosset-Cheneau, C. Vergnaud, M. Jamet, P. Noel, **T. Gushi**, A. Brenac, A. Marty, and J.-P. Attané, " *Observation of the Hanle effect in giant magnetoresistance measurements*, " *Appl. Phys. Lett.* **112**, 232405 (2018).
13. S. Isogami, A. Anzai, **T. Gushi**, T. Komori, and T. Suemasu, " *Temperature independent, wide modulation of anomalous Hall effect by Mn doping in $Fe_{4-x}Mn_xN$ pseudo-single-crystal films*, " *Jpn. J. Appl. Phys.* **57**, 120305 (2018).
14. **T. Gushi**, L. Vila, O. Fruchart, A. Marty, S. Pizzini, J. Vogel, F. Takata, A. Anzai, K. Toko, T. Suemasu, and J.-P. Attané, " *Millimeter-sized magnetic domains in perpendicularly magnetized ferrimagnetic Mn_4N thin film grown on $SrTiO_3$* , " *Jpn. J. Appl. Phys.* **57**, 120310 (2018).
15. T. Komori, A. Anzai, **T. Gushi**, K. Toko, and T. Suemasu, " *Molecular beam epitaxy growth of $Mn_{4-x}Ni_xN$ thin films on $MgO(001)$ substrates and their magnetic properties*, " *J. Cryst. Growth* **507**, 163 (2019).

International conferences (Oral presentations)

1. K. Ito, T. Sanai, Y. Yasutomi, **T. Gushi**, K. Toko, H. Yanagihara, M. Tsunoda, E. Kita, and T. Suemasu, " *Mossbauer study on epitaxial $Co_xFe_{4-x}N$ films grown by molecular beam epitaxy*, " 59th Annual Magnetism and Magnetic Materials (MMM) Conference, HF-09, Honolulu, USA, Nov. 7, 2014.
2. **T. Gushi**, K. Ito, S. Honda, Y. Yasutomi, S. Higashikozono, K. Toko, H. Oosato, Y. Sugimoto, K.

- Asakawa, N. Ota, and T. Suemasu, " *Control of domain wall position in L-shaped Fe₄N negatively spin polarized ferromagnetic nanowire*, "IEEE International Magnetics Conference 2015, EC-11, May 14, 2015, Beijing, China.
3. **T. Gushi**, K. Ito, S. Honda, Y. Yasutomi, S. Higashikozono, K. Toko, H. Oosato, Y. Sugimoto, K. Asakawa, N. Ota, and T. Suemasu, " *Observation and control of magnetic domain structure in Fe₄N ferromagnetic nanowire*, " ASCO-NANOMAT 2015, VI.24.03o, Vladivostok, Russia, August 25, 2015.
 4. K. Ito, Y. Yasutomi, K. Kabara, **T. Gushi**, S. Higashikozono, K. Toko, M. Tsunoda, and T. Suemasu, " *Perpendicular magnetic anisotropy of Co_xMn_{4-x}N (x = 0 and 0.2) epitaxial films on SrTiO₃(001) substrates*, " 13th Joint MMM-Intermag Conference, BF-12, San Diego, USA, Jan. 12, 2016.
 5. **T. Gushi**, L. Vila, J. P. Attane, O. Fruchart, A. Marty, S. Pizzini, F. Takata, A. Anzai and T. Suemasu, " *Domain wall properties and spin transfer torque in perpendicularly magnetized Mn₄N ferrimagnet thin films*, " Intermag 2018, Singapore, April 15, 2018.
 6. **T. Gushi**, L. Vila, J.-P. Attané, S. Pizzini, and T. Suemasu, " *Fast STT-driven DW motion in perpendicularly magnetized ferrimagnet Mn₄N*, " The 2nd Southeast Asia Collaborative Symposium on Energy Materials, Tsukuba, Japan, January 28, 2019.

International conferences (Poster presentations)

1. S. Higashikozono, K. Ito, F. Takata, **T. Gushi**, K. Toko, and T. Suemasu, " *Highly oriented epitaxial (α'+α)-Fe₁₆N₂ films on α-Fe(001) buffered MgAl₂O₄(001) substrates and their magnetizations*, " ICCGE-18, ThP-T05-13, Nagoya, Japan, August 11, 2016.
2. F. Takata, K. Ito, K. Kabara, S. Higashikozono, **T. Gushi**, K. Toko, M. Tsunoda, and T. Suemasu, " *Minority spin transport in epitaxially grown nickel-iron nitride films*, " SSDM2016, PS-12-20, Tsukuba, Japan, September 28, 2016.
3. **T. Gushi**, L. Vila, A. Marty, O. Fruchart, F. Takata, A. Anzai, T. Suemasu, and J. P. Attané, " *Millimeter sized magnetic domains in perpendicularly magnetized ferrimagnetic Mn₄N thin films*, " 18e Colloque Louis Néel, Paris, MULTI-P1, September 25, 2017.
4. A. Anzai, **T. Gushi**, F. Takata, K. Toko, T. Suemasu " *Epitaxial growth and magnetic properties of Mn_xFe_{4-x}N films on MgO(001) substrates*, " Tsukuba Global Science Week Interdisciplinary Workshop on Science and Patents 2017 IWP021, Tsukuba, September 26, 2017.
5. F. Takata, **T. Gushi**, A. Anzai, K. Toko, and T. Suemasu " *Fabrication of L1₀-MnAl films on lattice matched Mn₄N buffer layer*, " Tsukuba Global Science Week Interdisciplinary Workshop on Science and Patents 2017 IWP009, Tsukuba, September 26, 2017.
6. **T. Gushi**, M. Klug, L. Vila, J.-P. Attané, F. Takata, A. Anzai, T. Suemasu and S. Pizzini, " *Large STT-driven domain wall velocities in perpendicularly magnetized Mn₄N ferrimagnetic thin films*, " The 9th Joint European Magnetic Symposia Conference 2018, P-C. 108, Mainz, Germany, Sept. 6 (2018).
7. A. Anzai, **T. Gushi**, T. Komori, T. Suemasu, " *Growth of high quality Mn₄N magnetic films on SrTiO₃ substrate*, " Tsukuba Global Science Week Interdisciplinary Workshop on Science and Patents 2018, IWP047, Tsukuba, Sept. 21, 2018.
8. T. Komori, **T. Gushi**, A. Anzai, S. Isogami and T. Suemasu, " *Significant modification of magneto-transport properties of Mn₄N thin films by Ni substitution*, " Tsukuba Global Science Week Interdisciplinary Workshop on Science and Patents 2018, IWP048, Tsukuba, Sept. 21, 2018.

Domestic conferences (Oral presentations)

1. 安富陽子, 伊藤啓太, 佐内辰徳, **具志俊希**, 都甲薫, 末益崇, " MBE 法により作製した Co_xMn_{4-x}N 薄膜の磁気特性評価, " 第 61 回応用物理学学会春季学術講演会, 18a-E7-1, 神奈川, March 18 (2014).
2. **具志俊希**, 伊藤啓太, 佐内辰徳, 安富陽子, 都甲薫, 大里啓孝, 杉本喜正, 浅川潔, 太田憲雄, 本多周太, 末益崇, " Fe₄N 強磁性細線の作製と磁気力顕微鏡による磁区観察, " 第 61 回応用物理学学会春季学術講演会, 18a-E7-4, 神奈川, March 18 (2014).
3. 安富陽子, 伊藤啓太, **具志俊希**, 都甲薫, 末益崇, " Co_xMn_{4-x}N 薄膜における磁気特性の Co/Mn 比依存性, " 第 75 回応用物理学学会秋季学術講演会 18a-S2-6, 札幌, Sept.18 (2014).
4. **具志俊希**, 伊藤啓太, 安富陽子, 都甲薫, 大里啓孝, 杉本喜正, 浅川 潔, 太田憲雄, 本多周太, 末益崇, " < の字型及び円弧状 Fe₄N 強磁性細線の作製と磁区観察, " 第 75 回応用物理学学会秋季学術講演会 18a-S2-7, 札幌, Sept.18 (2014).
5. 伊藤啓太, 佐内辰徳, 安富陽子, **具志俊希**, 都甲薫, 柳原英人, 角田匡清, 喜多英治, 末益崇, "

List of publications

- $\text{Co}_x\text{Fe}_{4-x}\text{N}$ ($x = 0, 1, 3$) エピタキシャル膜のメスバウアー測定, " 第 75 回応用物理学会秋季学術講演会 18a-S2-8, 札幌, Sept.18 (2014).
- 伊藤啓太、安富陽子、鹿原和樹、**具志俊希**、東小菌創真、都甲薫、角田匡清、末益崇, " $\text{Co}_x\text{Mn}_{4-x}\text{N}$ エピタキシャル薄膜の飽和磁化と垂直磁気異方性の評価," 第 62 回応用物理学会春季学術講演会 11p-D11-5, 神奈川, March 11(2015).
 - 東小菌 創真、伊藤 啓太、安富 陽子、**具志 俊希**、都甲 薫、末益 崇, " MBE 法による α' - Fe_{16}N_2 薄膜のエピタキシャル成長," 第 62 回応用物理学会春季学術講演会 11p-D11-6, 神奈川, March 11 (2015).
 - 具志俊希**、伊藤啓太、安富陽子、東小菌創真、都甲薫、大里啓孝、杉本喜正、浅川潔、太田憲雄、本多周太、末益崇, " 負のスピンの分極率を有する Fe_4N 強磁性細線の磁壁形成位置の制御," 第 62 回応用物理学会春季学術講演会 11p-D11-7, 神奈川, March 11 (2015).
 - 具志 俊希**、伊藤 啓太、東小菌 創真、都甲薫、大里 啓孝、杉本 喜正、本多 周太、末益 崇, " Fe_4N 細線における磁壁物性の細線形状依存性の評価," 第 76 回応用物理学会秋季学術講演会 13a-2J-8, 名古屋, September 13 (2015).
 - 伊藤 啓太、**具志 俊希**、東小菌 創真、竹田 幸治、斎藤 祐児、都甲 薫、柳原 英人、角田 匡清、小口 多美夫、木村 昭夫、喜多 英治、末益 崇, " Fe_4N エピタキシャル薄膜の窒素原子占有度の評価," 第 39 回日本磁気学会学術講演会 11aA-10, 名古屋, September 11 (2015).
 - 高田 郁弥、伊藤 啓太、**具志 俊希**、東小菌 創真、都甲 薫、末益 崇, " MBE 法による強磁性窒化物 $\text{Ni}_x\text{Fe}_{4-x}\text{N}$ 薄膜のエピタキシャル成長," 第 63 回応用物理学会春季学術講演会 21a-W241-6, 東京, March 21 (2016).
 - 東小菌 創真、伊藤 啓太、**具志 俊希**、都甲 薫、末益 崇, " MgAl_2O_4 基板上への高配向 ($\alpha'+\alpha'$)- Fe_{16}N_2 薄膜のエピタキシャル成長," 第 63 回応用物理学会春季学術講演会 21a-W241-7, 東京, March 21 (2016).
 - 伊藤 啓太、鹿原 和樹、高田 郁弥、東小菌 創真、**具志 俊希**、都甲 薫、角田 匡清、末益 崇, " エピタキシャル $\text{Ni}_x\text{Fe}_{4-x}\text{N}$ ($x = 0, 1, 3, 4$) 薄膜の磁気物性の評価," 第 40 回日本磁気学会学術講演会 6pA-6, 石川, September 6 (2016).
 - T. Gushi**, L. Vila, J. P. Attane, O. Fruchart, A. Marty, S. Pizzini, F. Takata, A. Anzai and T. Suemasu, " *Magnetic properties of perpendicularly magnetized Mn_4N thin films deposited on MgO and STO substrates, for current-induced domain-wall motion devices,* " 第 78 回応用物理学会秋季学術講演会 5a-C18-6, 福岡, September 5 (2017).
 - 安西 聡仁、花島 隆泰、**具志 俊希**、高田 郁弥、都甲 薫、末益 崇, " Mn_4N 上 Fe_4N 垂直磁化積層膜の作製 " 第 78 回応用物理学会秋季学術講演会 5a-C18-8, 福岡, September 5 (2017).
 - 安西 聡仁、**具志 俊希**、小森 太郎、都甲 薫、末益 崇, " 酸化物基板上への Mn_4N 薄膜の成長と磁気特性の膜厚依存性評価 " 第 79 回応用物理学会秋季学術講演会 18p-131-2, 名古屋, Sept. 18 (2018).
 - T. Gushi**, L. Vila, J.-P. Attané, O. Fruchart, A. Marty, S. Pizzini, J. Vogel, F. Takata, A. Anzai, and T. Suemasu, " *Investigation of spin-transfer properties in ferrimagnetic Mn_4N nanowires,* " 第 65 回応用物理学会春季学術講演会 19p-D104-17, 東京, March 19 (2018).
 - T. Komori, **T. Gushi**, F. Takata, A. Anzai, K. Toko, and T. Suemasu, " *Epitaxial growth of $\text{Mn}_{4-x}\text{Ni}_x\text{N}$ thin films by MBE and their characterizations,* " 第 65 回応用物理学会春季学術講演会 19p-D104-18, 東京, March 19 (2018).
 - T. Gushi**, L. Vila, J. P. Attané, O. Fruchart, A. Marty, S. Pizzini, J. Vogel, M. Klug, J. Pena-Garcia, A. Anzai, T. Komori, and T. Suemasu, " *Ultrafast STT-driven domainwall motion in Mn_4N microstrips,* " 第 79 回応用物理学会秋季学術講演会 18a-131-6, 名古屋, Sept. 18 (2018).
 - T. Komori, **T. Gushi**, A. Anzai, K. Toko, S. Isogami and T. Suemasu, " *Significant modification of magneto-transport properties of Mn_4N thin films by Ni substitution,* " 第 79 回応用物理学会秋季学術講演会 18a-131-7, 名古屋, Sept. 18 (2018).

Domestic conferences (Poster presentations)

- T. Gushi**, K. Ito, T. Sanai, Y. Yasutomi, K. Toko, H. Osato, Y. Sugimoto, K. Asakawa, N. Ota, S. Honda, and T. Suemasu, 第 33 回電子材料シンポジウム, 19p-P8-3, 静岡, July 10, 2014.

2. 東小菌創真, 伊藤啓太, 具志俊希, 都甲薫, 末益崇, " α -Fe 下地を用いた MgAl_2O_4 基板上への α' -Fe-N のエピタキシャル成長, " 第 76 回応用物理学会秋季学術講演会 13p-PA1-24, 名古屋, September 13 (2015).
3. 伊藤 啓太, 具志 俊希, 東小菌 創真, 都甲 薫, 白井 正文, 角田 匡清, 末益 崇, " 垂直磁気異方性をもつ正方晶フェリ磁性 Mn_4N 薄膜の磁気構造, " 第 63 回応用物理学会春季学術講演会 19p-P1-17, 東京, March 19 (2016).
4. 具志 俊希, 伊藤 啓太, 東小菌 創真, 都甲 薫, 大里 啓孝, 杉本 喜正, 本多 周太, 末益 崇, " 異方性磁気抵抗効果を利用した Fe_4N 細線における磁壁の電流検出, " 第 63 回応用物理学会春季学術講演会 19p-P1-18, 東京, March 19 (2016).
5. 具志 俊希 " Fe_4N 強磁性細線中の磁壁における抵抗変化の検出, " 第 39 回光通信研究会 P2-32, 山梨, August 9 (2016).
6. 東小菌 創真, 伊藤 啓太, 具志 俊希, 高田 郁弥, 都甲 薫, 末益 崇, " MBE 法で作製した α' - $\text{Fe}_{16-x}\text{Mn}_x\text{N}_2$ ($x=0,1,2$)薄膜の磁気特性, " 第 77 回応用物理学会秋季学術講演会 13p-P8-26, 新潟, September 13 (2016).
7. 高田 郁弥, 伊藤 啓太, 鹿原和樹, 東小菌創真, 具志俊希, 都甲薫, 角田匡清, 末益崇, " $\text{Ni}_x\text{Fe}_{4-x}\text{N}$ ($x=1, 3$)薄膜の負の異方向性磁気抵抗効果, " 第 77 回応用物理学会秋季学術講演会 13p-P8-22, 新潟, September 13 (2016).
8. 高田 郁弥, 具志 俊希, 東小菌 創真, 都甲 薫, 末益 崇, " N 添加が L10-MnAl の磁気異方性に与える影響, " 第 64 回応用物理学会春季学術講演会 14p-P10-49, 横浜, March 14 (2017).
9. 安西 聡仁, 具志 俊希, 東小菌 創真, 高田 郁弥, 都甲 薫, 末益 崇, " 逆ペロブスカイト型強磁性窒化物 $\text{Mn}_x\text{Fe}_{4-x}\text{N}$ 薄膜の磁気特性 " 第 64 回応用物理学会春季学術講演会 14p-P10-67, 横浜, March 14 (2017).
10. 安西 聡仁, 花島 隆泰, 具志 俊希, 高田 郁弥, 都甲 薫, 末益 崇, " Mn_4N 上 Fe_4N 垂直磁化積層膜の作製, " 第 6 回結晶工学未来塾, 東京大学, November 2 (2017).
11. 高田 郁弥, 具志俊希, 安西聡仁, 都甲薫, 末益崇, " 格子不整合率が τ -MnAl 薄膜の歪みと磁気特性に与える影響, " 第 36 回電子材料シンポジウム, Th4-2, 長浜, November 9 (2017).
12. 安西聡仁, 花島隆泰, 具志俊希, 高田郁弥, 都甲薫, 末益崇, " $\text{Mn}_x\text{Fe}_{4-x}\text{N}$ 薄膜のエピタキシャル成長と磁気特性, " 第 36 回電子材料シンポジウム, Th4-3, 長浜, November 9 (2017).
13. 安西 聡仁, 具志 俊希, 高田 郁弥, 都甲 薫, 花島 隆泰, 末益 崇, " Mn_4N 垂直磁化膜上の Fe_4N 膜の深さ方向磁化分布評価 " 第 65 回応用物理学会春季学術講演会 17p-P10-47, 東京, March 17 (2018).
14. F. Takata, T. Gushi, A. Anzai, K. Toko, and Takashi Suemasu, " Crystal growth of L10-MnAl film on Mn_4N underlayer and effect of crystallinity on magnetic properties " 第 65 回応用物理学会春季学術講演会 17p-P10-44, 東京, March 17 (2018).

Awards

1. Young Scientist Award, 3rd Asian School-Conference on Physics and Technology of Nanostructured Materials, Vladivostok, Russia, T. Gushi, K. Ito, S. Honda, Y. Yasutomi, S. Higashikozono, K. Toko, H. Oosato, Y. Sugimoto, K. Asakawa, N. Ota, and T. Suemasu, " *Observation and control of magnetic domain structure in Fe_4N ferromagnetic nanowire*, " August 25, 2015.
2. 2015 年度数理物質科学研究科長表彰, (受賞対象論文) 具志俊希, 修士論文, 「磁気力顕微鏡を用いた Fe_4N 強磁性細線の磁区観察と磁壁の電流検出」, March 23 (2016).
3. 2018 年春季応用物理学会英語講演奨励賞, (受賞対象論文) T. Gushi, L. Vila, J.-P. Attané, O. Fruchart, A. Marty, S. Pizzini, J. Vogel, F. Takata, A. Anzai, and T. Suemasu, " *Investigation of spin-transfer properties in ferrimagnetic Mn_4N nanowires*, " March 19 (2018).

Reference

- ¹ J. Bardeen, and W. Brattain, *Phys. Rev.* **74**, 230 (1948).
- ² W. Shockley, *Bell System Technical Journal*, **28**, 435 (1949).
- ³ S. Kilby, US Patent 3,138,743, (1959).
- ⁴ K. Lehovec, U.S. Patent 3,029,366, (1959).
- ⁵ G. E. Moore, *Electronics* **38**, 8 (1965).
- ⁶ R. H. Dennard, F. H. Gaensslen, L. Kuhn, and H. N. Yu, *IEEE Int. Electron Devices Meeting*, Washington, D.C., (1972).
- ⁷ International Technology Roadmap for Semiconductors 2005.
- ⁸ L. J. Edgar, U.S. Patent 1 1,745,175A (1926).
- ⁹ D. Kahng, U. S. Patent 3,102,230 (1960).
- ¹⁰ Y. Nakagome, M. Horiguchi, T. Kawahara, K. Itoh, *IBM Journal of Research and Development* **47**, 525 (2003).
- ¹¹ D. E. Nikonov, and I. A. Young, *Proceedings of the IEEE* **101**, 2498 (2013).
- ¹² M. N. Baibich, J. M. Broto, A. Fert, F. Nguyen van Dau, F. Petroff, P. Eitenne, G. Creuzet, A. Friederich, and J. Chazelas, *Phys. Rev. Lett.* **61**, 2472 (1988).
- ¹³ G. Binasch, P. Gruñberg, F. Saurenbach, and W. Zinn, *Phys. Rev. B* **39**, 4828 (1989).
- ¹⁴ T. Miyazaki and N. Tezuka, *J. Magn. Magn. Mater.* **139**, L231 (1995).
- ¹⁵ J. S. Moodera, L. R. Kinder, T. M. Wong, and R. Meservey, *Phys. Rev.Lett.* **74**, 3273 (1995).
- ¹⁶ J. C. Slonczewski, *J. Magn. Magn. Mater.* **159**, L1 (1996).
- ¹⁷ L. Berger, *Phys. Rev. B* **54**, 9353 (1996).
- ¹⁸ S. S. P. Parkin, M. Hayashi, and L. Thomas, *Science* **320**, 190 (2008).
- ¹⁹ S. Fukami, T. Suzuki, K. Nagahara, N. Ohshima, Y. Ozaki, S. Saito, R. Nebashi, N. Sakimura, H. Honjo, K. Mori, C. Igarashi, S. Miura, N. Ishiwata and T. Sugibayashi, 2009 Symposium on VLSI Technology. Digest Tech. Pap. 230 (2009).
- ²⁰ A. Yamaguchi, T. Ono, S. Nasu, K. Miyake, K. Mibu, and T. Shinjo, *Phys. Rev. Lett.* **92**, 077205 (2004)
- ²¹ M. Kläui, C. A. F. Vaz, J. A. C. Bland, W. Wernsdorfer, G. Faini, E. Cambril, L. J. Heyderman, F. Nolting, and U. Rüdiger, *Phys. Rev. Lett.* **94**, 106601 (2005).
- ²² M. Hayashi, L. Thomas, Ya. B. Bazaliy, C. Rettner, R. Moriya, X. Jiang, and S. S. P. Parkin, *Phys. Rev. Lett.* **96**, 197207 (2006).
- ²³ G. S. D. Beach, C. Knutson, C. Nistor, M. Tsoi, and J. L. Erskine, *Phys. Rev. Lett.* **97**, 057203 (2006).
- ²⁴ M. Hayashi, L. Thomas, C. Rettner, R. Moriya, Y. B. Bazaliy, and S. S. P. Parkin, *Phys. Rev. Lett.* **98**, 037204 (2007).
- ²⁵ I. M. Miron, G. Gaudin, S. Auffret, B. Rodmacq, A. Schuhl, S. Pizzini, J. Vogel, and P. Gambardella, *nature mater.* **9**, 230 (2010).

-
- ²⁶ L. Liu, T. Moriyama, D. C. Ralph, and R. A. Buhrman, *Phys. Rev. Lett.* **106**, 036601 (2011).
- ²⁷ I. M. Miron, T. Moore, H. Szabolcs, L. D. Buda-Prejbeanu, S. Auffret, B. Rodmacq, S. Pizzini, J. Vogel, M. Bonfim, A. Schuhl and G. Gaudin, *Nat. Mater.* **10**, 419 (2011).
- ²⁸ L. Caretta, M. Mann, F. Büttner, K. Ueda, B. Pfau, C. M. Günther, P. Hession, A. Churikova, C. Klose, M. Schneider, D. Engel, C. Marcus, D. Bono, K. Bagnschik, S. Eisebitt, and G. S. D. Beach, *Nature Nanotech.* **13**, 1154 (2018).
- ²⁹ S.-G. Je, J.-C. Rojas-Sánchez, T. H. Pham, P. Vallobra, G. Malinowski, D. Lacour, T. Fache, M.-C. Cyrille, D.-Y. Kim, S.-B. Choe, M. Belmeguenai, M. Hehn, S. Mangin, G. Gaudin, and O. Boulle, *Appl. Phys. Lett.* **112**, 062401 (2018).
- ³⁰ S. Glöser, L. T. Espinoza, C. Gandenberger, and M. Faulstich, *Resources Policy* **44**, 35 (2015).
- ³¹ Y. Yasutomi, K. Ito, T. Sanai, K. Toko, and T. Suemasu, *J. Appl. Phys.* **115**, 17A935 (2014).
- ³² K. Takanashi, *Jpn. J. Appl. Phys.* **49**, 110001 (2010).
- ³³ S. Datta and B. Das, *Appl. Phys. Lett.* **56**, 665 (1990).
- ³⁴ H. Ohno, H. Munekata, T. Penney, S. von Molnár, and L. L. Chang, *Phys. Rev. Lett.* **68**, 2664 (1992).
- ³⁵ Y. Ohno, D. K. Young, B. Beschoten, F. Matsukura, H. Ohno, and D. D. Awschalom, *Nature* **402**, 790 (1999).
- ³⁶ R. Fiederling, M. Keim, G. Reuscher, W. Ossau, G. Schmidt, A. Waag, and L. W. Molenkamp, *Nature* **402**, 787 (1999).
- ³⁷ T. Hayashi, H. Shimada, H. Shimizu, and M. Tanaka, *J. Cryst. Growth* **201–202**, 689 (1999).
- ³⁸ F. J. Jedema, A. T. Filip, and B. J. van Wees, *Nature* **410**, 345 (2001).
- ³⁹ H. Ohno, D. Chiba, F. Matsukura, T. Omiya, E. Abe, T. Dietl, Y. Ohno, and K. Ohtani, *Nature* **408**, 944 (2000).
- ⁴⁰ S. I. Kiselev, J. C. Sankey, I. N. Krivorotov, N. C. Emley, R. J. Schoelkopf, R. A. Buhrman, and D. C. Ralph, *Nature* **425**, 380 (2003).
- ⁴¹ A. Oiwa, Y. Mitsumori, R. Moriya, T. Slupinski, and H. Munekata, *Phys. Rev. Lett.* **88**, 137202 (2002).
- ⁴² D. Chiba, Y. Sato, T. Kita, F. Matsukura, and H. Ohno, *Phys. Rev. Lett.* **93**, 216602 (2004).
- ⁴³ M. Yamanouchi, D. Chiba, F. Matsukura, and H. Ohno, *Nature* **428**, 539 (2004).
- ⁴⁴ S. Yuasa, A. Fukushima, T. Nagahama, K. Ando, and Y. Suzuki, *Jpn. J. Appl. Phys.* **43**, L588 (2004).
- ⁴⁵ S. Yuasa, T. Nagahama, A. Fukushima, Y. Suzuki, and K. Ando, *Nat. Mater.* **3**, 868 (2004).
- ⁴⁶ S. S. P. Parkin, C. Kaiser, A. Panchula, P. M. Rice, B. Hughes, M. Samant, and S.-H. Yang, *Nat. Mater.* **3**, 862 (2004).
- ⁴⁷ Y. K. Kato, R. C. Myers, A. C. Gossard, and D. D. Awschalom, *Science* **306**, 1910 (2004).
- ⁴⁸ J. Wunderlich, B. Kaestner, J. Sinova, and T. Jungwirth, *Phys. Rev. Lett.* **94**, 047204 (2005).
- ⁴⁹ T. Bergsten, T. Kobayashi, Y. Sekine, and J. Nitta, *Phys. Rev. Lett.* **97**, 196803 (2006).
- ⁵⁰ S. O. Valenzuela and M. Tinkham, *Nature* **442**, 176 (2006).
- ⁵¹ E. Saitoh, M. Ueda, H. Miyajima, and G. Tatara, *Appl. Phys. Lett.* **88**, 182509 (2006).
- ⁵² T. Kimura, Y. Otani, T. Sato, S. Takahashi, and S. Maekawa, *Phys. Rev. Lett.* **98**, 156601 (2007).
- ⁵³ X. Lou, C. Adelman, S. A. Crooker, E. S. Garlid, J. Zhang, K. S. M. Reddy, S. D. Flexner, J. Palmström, and

-
- P. A. Crowell, *Nat. Phys.* **3**, 197 (2007).
- ⁵⁴ I. Appelbaum, B. Huang, and D. J. Monsma, *Nature* **447**, 295 (2007).
- ⁵⁵ B. T. Jonker, G. Kioseoglou, A. T. Hanbicki, C. H. Li, and P. E. Thompson, *Nat. Phys.* **3**, 542 (2007).
- ⁵⁶ K. Takanashi, *Materia Japan* **56**, 190 (2016).
- ⁵⁷ A. Qaiumzadeh, R. A. Duine, and M. Titov, *Phys. Rev. B* **92**, 014402 (2015).
- ⁵⁸ M. Weisheit, S. Fähler, A. Marty, Y. Souche, C. Poinignon and D. Givord, *Science* **315**, 349 (2007).
- ⁵⁹ T. Seki, Y. Hasegawa, S. Mitani, S. Takahashi, H. Imamura, S. Maekawa, J. Nitta and K. Takanashi, *Nat. Mater.* **7**, 125 (2008).
- ⁶⁰ T. Yang, T. Kimura and Y. Otani, *Nat. Phys.* **4**, 851 (2008).
- ⁶¹ K. Uchida, S. Takahashi, K. Harii, J. Ieda, W. Koshibae, K. Ando, S. Maekawa and E. Saitoh, *Nature* **455**, 778 (2008).
- ⁶² T. Maruyama, Y. Shiota, T. Nozaki, K. Ohta, N. Toda, M. Mizuguchi, A. A. Tulapurkar, T. Shinjo, M. Shiraishi, S. Mizukami, Y. Ando and Y. Suzuki, *Nat. Nanotech.* **4**, 158 (2009).
- ⁶³ S. Ikeda, K. Miura, H. Yamamoto, K. Mizunuma, H. D. Gan, M. Endo, S. Kanai, J. Hayakawa, F. Matsukura and H. Ohno, *Nat. Mater.* **9**, 721 (2010).
- ⁶⁴ Y. Kajiwara, K. Harii, S. Takahashi, J. Ohe, K. Uchida, M. Mizuguchi, H. Umezawa, H. Kawai, K. Ando, K. Takanashi, S. Maekawa and E. Saitoh, *Nature* **464**, 262 (2010).
- ⁶⁵ A. Thiaville, S. Rohart, É. Jué, V. Cros, and A. Fert, *Europhys. Lett.* **100**, 57002 (2012).
- ⁶⁶ A. Fert, V. Cros, and J. Sampaio, *Nat. Nanotech.* **8**, 152 (2013).
- ⁶⁷ T. An, V. I. Vasyuchka, K. Uchida, A. V. Chumak, K. Yamaguchi, K. Harii, J. Ohe, M. B. Jungfleisch, Y. Kajiwara, H. Adachi, B. Hillebrands, S. Maekawa and E. Saitoh, *Nat. Mater.* **12**, 549 (2013).
- ⁶⁸ R. Takahashi, M. Matsuo, M. Ono, K. Harii, H. Chudo, S. Okayasu, J. Ieda, S. Takahashi, S. Maekawa and E. Saitoh, *Nat. Phys.* **12**, 52 (2016).
- ⁶⁹ W. B. Zeper, F. J. A. M. Greidanus, P. F. Carcia, and C. R. Fincher, *J. Appl. Phys.* **65**, 4971 (1989).
- ⁷⁰ S. Ikeda, K. Miura, H. Yamamoto, K. Mizunuma, H. D. Gan, M. Endo, S. Kanai, J. Hayakawa, F. Matsukura, and H. Ohno, *Nature Mater.* **9**, 721 (2010).
- ⁷¹ V. Gehanno, Y. Samson, A. Marty, B. Gilles, and A. Chamberod, *J. Magn. Magn. Mater.* **172**, 26 (1997).
- ⁷² L. Landau and E. Lifshits, *Physik. Zeits. Sowjetunion* **8**, 153 (1935).
- ⁷³ T. L. Gilbert, *IEEE Trans. Magn.* **40**, 3443 (2004).
- ⁷⁴ S. Zhang, and Z. Li, *Phys. Rev. Lett.* **93**, 127204 (2004).
- ⁷⁵ A. Thiaville, Y. Nakatani, J. Miltat, and Y. Suzuki, *Europhys. Lett.* **69**, 990 (2005).
- ⁷⁶ A. Brataas, A. D. Kent, and H. Ohno, *nature mater.* **11**, 372 (2012).
- ⁷⁷ E. B. Myers, D. C. Ralph, J. A. Katine, R. N. Louie, and R. A. Buhrman, *Science* **285**, 867 (1999).
- ⁷⁸ J. A. Katine, F. J. Albert, R. A. Buhrman, E. B. Myers, and D. C. Ralph, *Phys. Rev. Lett.* **84**, 3149 (2000).
- ⁷⁹ M. Tsoi, A. G. M. Jansen, J. Bass, W.-C. Chiang, M. Seck, V. Tsoi, and P. Wyder, *Phys. Rev. Lett.* **80**, 4281 (1998).
- ⁸⁰ L. Berger, *J. Appl. Phys.* **55**, 1954 (1984).

-
- ⁸¹ T. Koyama, D. Chiba, K. Ueda, K. Kondou, H. Tanigawa, S. Fukami, T. Suzuki, N. Ohshima, N. Ishiwata, Y. Nakatani, K. Kobayashi, and T. Ono, *nature mater.* **10**, 194 (2011).
- ⁸² A. P. Malozemoff, and J. C. Slonczewski, *Phys. Rev. Lett.* **29**, 952 (1972)
- ⁸³ Nasser, S. A., Sarma, B., Durin, G., & Serpico, C. Analytical Modelling of Magnetic DW Motion. *Physics Procedia*, **75**, 974 (2015).
- ⁸⁴ A. Mougin, M. Cormier, J. P. Adam, P. J. Metaxas, and J. Ferré. *Europhys. Lett.* **78**, 57007 (2007).
- ⁸⁵ S. Emori, and G. S. D. Beach, *Appl. Phys. Lett.* **98**, 132508 (2011).
- ⁸⁶ R. K. Wangsness, *Physical Review*, **91**, 1085 (1953).
- ⁸⁷ R. Giles, and M. Mansuripur, *J. Magn. Soc. Jpn.* **15**, 299 (1991) Suppl. S1.
- ⁸⁸ C. D. Stanciu, A. V. Kimel, F. Hansteen, A. Tsukamoto, A. Itoh, A. Kirilyuk, and Th. Rasing, *Phys. Rev. B* **73**, 220402(R) (2006).
- ⁸⁹ A. Canizo-Cabrera, V. Garcia-Vazquez, and Te-ho Wu, *J. Appl. Phys.* **99**, 08G512 (2006).
- ⁹⁰ N. Vernier, D. A. Allwood, D. Atkinson, M. D. Cooke, and R. P. Cowburn, *Europhys. Lett.* **65**, 526 (2004).
- ⁹¹ M. Kläui, P.-O. Jubert, R. Allenspach, A. Bischof, J. A. C. Bland, G. Faini, U. Rüdiger, C. A. F. Vaz, L. Vila, and C. Vouille, *Phys. Rev. Lett.* **95**, 026601 (2005).
- ⁹² K.-S. Ryu, L. Thomas, S.-H. Yang, and S. S. P. Parkin, *Appl. Phys. Express* **5**, 093006 (2012).
- ⁹³ D.-T. Ngo, N. Watanabe, and H. Awano, *Jpn. J. Appl. Phys.* **51**, 093002 (2012).
- ⁹⁴ H. Awano, *J. Magn. Magn. Mater.* **383**, 50 (2015).
- ⁹⁵ I. M. Miron, T. Moore, H. Szabolcs, L. D. Buda-Prejbeanu, S. Auffret, B. Rodmacq, S. Pizzini, J. Vogel, M. Bonfim, A. Schuhl, and G. Gaudin, *nature mater.* **10**, 419 (2011).
- ⁹⁶ S.-H. Yang, K.-S. Ryu, and S. Parkin, *nature nanotechnol.* **10**, 221 (2015).
- ⁹⁷ L. Caretta, M. Mann, F. Büttner, K. Ueda, B. Pfau, C. M. Günther, P. Hession, A. Churikova, C. Klose, M. Schneider, D. Engel, C. Marcus, D. Bono, K. Bagnschik, S. Eisebitt, and G. S. D. Beach, *Nature Nanotech.* **13**, 1154 (2018).
- ⁹⁸ A. Narahara, K. Ito, and T. Suemasu, *J. Cryst. Growth* **311**, 1616 (2009).
- ⁹⁹ K. Ito, G. H. Lee, M. Suzuno, H. Akinaga, and T. Suemasu, *J. Cryst. Growth* **322**, 63 (2011).
- ¹⁰⁰ K. Ito, K. Harada, K. Toko, H. Akinaga, and T. Suemasu, *J. Cryst. Growth* **336**, 40 (2011).
- ¹⁰¹ K. Ito, K. Harada, K. Toko, M. Ye, A. Kimura, Y. Takeda, Y. Saitoh, H. Akinaga, and T. Suemasu, *Appl. Phys. Lett.* **99**, 252501 (2011).
- ¹⁰² F. Takata, K. Ito, T. Gushi, S. Higashikozono, K. Toko, and T. Suemasu, *J. Appl. Phys.* **120**, 083907 (2016).
- ¹⁰³ T. Sanai, K. Ito, K. Toko, and T. Suemasu, *J. Cryst. Growth* **378**, 342 (2013).
- ¹⁰⁴ K. Ito, Y. Yasutomi, K. Kabara, T. Gushi, S. Higashikozono, K. Toko, M. Tsunoda, and T. Suemasu, *AIP Advances* **6**, 056201 (2016).
- ¹⁰⁵ A. Anzai, F. Takata, T. Gushi, K. Toko, and T. Suemasu, *J. Cryst. Growth* **489**, 20 (2018).
- ¹⁰⁶ K. Ito, S. Higashikozono, F. Takata, T. Gushi, K. Toko, and T. Suemasu, *J. Cryst. Growth* **455**, 66 (2016).
- ¹⁰⁷ W. J. Takei, R. R. Heikes, and G. Shirane, *Phys. Rev.* **125**, 1893 (1962).
- ¹⁰⁸ D. Fruchart, D. Givord, P. Convert, P. l'Heritier, and J. P. Senateur, *J. Phys. F: Met. Phys.*, **9**, 2431 (1979).

-
- ¹⁰⁹ M. Uhl, S. F. Mater, and P. Mohn, *Phys. Rev. B* **55**, 2995 (1997).
- ¹¹⁰ C. Li, Y. Yang, L. Lv, H. Huang, Z. Wang, and S. Yang, *J. Alloys and Compounds* **457**, 57 (2008).
- ¹¹¹ K. Takenaka, and H. Takagi, *Appl. Phys. Lett.* **87**, 261902 (2005).
- ¹¹² S. Nakagawa, M. Naoe, *J. Appl. Phys.* **75**, 3568 (1994).
- ¹¹³ S. Dhar, O. Brandt, and K. H. Ploog, *Appl. Phys. Rev.* **86**, 112504 (2005).
- ¹¹⁴ X. Shen, A. Chikamatsu, K. Shigematsu, Y. Hirose, T. Fukumura, and T. Hasegawa, *Appl. Phys. Lett.* **105**, 072410 (2014).
- ¹¹⁵ K. Kabara, and M. Tsunoda, *J. Appl. Phys.* **117**, 17B512 (2015).
- ¹¹⁶ M. Meng, S. X. Wu, L. Z. Ren, W. Q. Zhou, Y. J. Wang, G. L. Wang, and S. W. Li, *Appl. Phys. Lett.* **106**, 032407 (2015).
- ¹¹⁷ K. Kabara, M. Tsunoda, and S. Kokado, *AIP Advances* **7**, 056416 (2017).
- ¹¹⁸ S. Isogami, A. Anzai, T. Gushi, T. Komori, and T. Suemasu, *Jpn. J. Appl. Phys.* **57**, 120305 (2018).
- ¹¹⁹ K. M. Ching, W. D. Chang, T. S. Chin, J. G. Duh, and H. C. Ku, *J. Appl. Phys.* **76**, 6582 (1994).
- ¹²⁰ K.-M. Ching, W.-D. Chang, T.-S. Chin, *J. Alloy and Compounds* **222**, 184 (1995).
- ¹²¹ T. Gushi, L. Vila, O. Fruchart, A. Marty, S. Pizzini, J. Vogel, F. Takata, A. Anzai, K. Toko, T. Suemasu, and J.-P. Attané, *Jpn. J. Appl. Phys.* **57**, 120310 (2018).
- ¹²² S. Hasegawa, *Characterization of Materials*, ed. E. N. Kaufmann, Wiley (2012).
- ¹²³ *Rigaku journal* **38**, 11, (2007).
- ¹²⁴ *Rigaku journal* **39**, 26 (2008).
- ¹²⁵ Lake Shore Cryotronics, Inc. User's Manual 7300 Series VSM System.
http://www.lakeshore.com/ObsoleteAndResearchDocs/7300_Manual.pdf, 2001.
- ¹²⁶ R. L. Fagaly, *Review of scientific instruments* **77**, 101101 (2006).
- ¹²⁷ B. D. Josephson, *Phys. Lett.* **1**, 251 (1962).
- ¹²⁸ Quantum Design web page: <https://www.qdusa.com/products/mpms3.html>
- ¹²⁹ K. Kabara, and M. Tsunoda, *J. Appl. Phys.* **117**, 17B512 (2015).
- ¹³⁰ Quantum Design web page: <https://www.qdusa.com/products/ppms.html>
- ¹³¹ L. J. van der Pauw, *Philips Res. Repts* **13**, 1, (1958).
- ¹³² L. J. van der Pauw, *Philips Technical Review* **20**, 220 (1958).
- ¹³³ Newton's method (Wolfram Math World): <http://mathworld.wolfram.com/NewtonsMethod.html>
- ¹³⁴ K. Okamoto, *J. Magn. Magn. Mater.* **35**, 353 (1983).
- ¹³⁵ S. Haan, C. Lodder, T. J. A. Popma, *J. Magn. Soc. Jpn.* **15**, S2, 349 (1991).
- ¹³⁶ L. Ejsing, M. F. Hansen, A. K. Menon, H. A. Ferreira, D. L. Graham, and P. P. Freitas, *Appl. Phys. Lett.*, **84**, 4729 (2004).
- ¹³⁷ J. Smit, *Physica* **21**, 877 (1955).
- ¹³⁸ J. Smit, *Physica* **24**, 39 (1958).
- ¹³⁹ L. Berger, *Phys. Rev. B* **2**, 4559 (1970).
- ¹⁴⁰ M.-C. Chang and Q. Niu, *Phys. Rev. B* **53**, 7010 (1996).

-
- ¹⁴¹ G. Sundaram and Q. Niu, *Phys. Rev. B* **59**, 14915 (1999).
- ¹⁴² E. Saitoh, M. Ueda, and H. Miyajima, and G. Tatara, *Appl. Phys. Lett.* **88**, 182509 (2006).
- ¹⁴³ N. Nagaosam, J. Sinova, S. Onoto, A. H. MacDonald, and N. P. Ong, *Rev. of Modern Phys.* **82**, 1539 (2010).
- ¹⁴⁴ D. Chiba, M. Kawaguchi, S. Fukami, N. Ishiwata, K. Shimamura, K. Kobayashi, and T. Ono, *Nature Commun.* **3**, 888 (2012).
- ¹⁴⁵ K. Yamada, H. Kakizakai, K. Shimamura, M. Kawaguchi, S. Fukami, N. Ishiwata, D. Chiba, and T. Ono, *Appl. Phys. Express* **6**, 073004 (2013).
- ¹⁴⁶ T. Hirai, T. Koyama, A. Obinata, Y. Hibino, K. Miwa, S. Ono, M. Kohda, and D. Chiba, *Appl. Phys. Express* **9**, 063007 (2016).
- ¹⁴⁷ J. Kerr, *Phyl. Mag.* **3**, 321 (1877).
- ¹⁴⁸ P. Q. J. Nederpel, and J. W. D. Martens, *Rev. Sci. Instrum.*, **56**, 687 (1985).
- ¹⁴⁹ D. Passeri, C. Dong, M. Reggente, L. Angeloni, M. Barteri, F. A Scaramuzzo, F. D. Angelis, F. Marinelli, F. Antonelli, F. Rinaldi, C. Marianecchi, M. Carafa, A. Sorbo, D. Sordi, I. WCE Arends, and M. Rossi, *Biomatter*, **4**, e29507 (2014).
- ¹⁵⁰ K. Ito, N. Rougemaille, S. Pizzini, S. Honda, N. Ota, T. Suemasu, and O. Fruchart, *J. Appl. Phys.*, **121**, 243904 (2017).
- ¹⁵¹ J. P. Attané, Y. Samson, A. Marty, J. C. Toussaint, G. Dubois, A. Mougin, and J. P. Jamet, *Phys. Rev. Lett.* **93**, 257203 (2004).
- ¹⁵² M. Yamanouchi, A. Jander, P. Dhagat, S. Ikeda, F. Matsukura, and H. Ohno, *IEEE Magn. Lett.* **2**, 3000304 (2011).
- ¹⁵³ F. Ando, H. Kakizakai, T. Koyama, K. Yamada, M. Kawaguchi, S. Kim, K-J. Kim, T. Moriyama, D. Chiba, and T. Ono, *Appl. Phys. Lett.* **109**, 022401 (2016).
- ¹⁵⁴ M. Meng, S. X. Wu, L. Z. Ren, W. Q. Zhou, Y. J. Wang, G. L. Wang, and S.W. Li, *Appl. Phys. Lett.* **106**, 032407 (2015).
- ¹⁵⁵ C. Burrowes, A. P. Mihai, D. Ravelosona, J.-V. Kim, C. Chappert, L. Vila, A. Marty, Y. Samson, F. Garcia-Sanchez, L. D. Buda-Prejbeanu, I. Tudosa, E. E. Fullerton & J.-P. Attané, *Nature Physics* **6**, 17 (2010).
- ¹⁵⁶ T. Koyama, D. Chiba, K. Ueda, K. Kondou, H. Tanigawa, S. Fukami, T. Suzuki, N. Ohshima, N. Ishiwata, Y. Nakatani, K. Kobayashi, T. Ono, *Nat. Mater.* **10**, 194 (2011).
- ¹⁵⁷ S. Fukami, T. Suzuki, Y. Nakatani, N. Ishiwata, M. Yamanouchi, S. Ikeda, N. Kasai, H. Ohno, *Appl. Phys. Lett.* **98**, 082504 (2011).
- ¹⁵⁸ M. Feigenson, J.W. Reiner, L. Klein, *Phys. Rev. Lett.* **98**, 247204 (2007).
- ¹⁵⁹ C. Burrowes, A.P. Mihai, D. Ravelosona, J. Kim, C. Chappert, L. Vila, A. Marty, Y. Samson, F. Garcia-Sanchez, L.D. Buda-Prejbeanu, I. Tudosa, E.E. Fullerton, J. Attane, *Nat. Phys.* **6**, 17 (2010).
- ¹⁶⁰ S. Li, H. Nakamura, T. Kanazawa, X. Liu, A. Morisako, *IEEE transmag* **46**, 1695 (2010).
- ¹⁶¹ V. D. Nguyen, L. Vila, A. Marty, P. Warin, C. Vergnaud, M. Jamet, L. Notin, C. Beigné, and J. P. Attané, *J. Appl. Phys.* **113**, 183906 (2013).
- ¹⁶² A. P. Mihai, J. P. Attané, A. Marty, P. Warin and Y. Samson, *Phys. Rev. B* **77**, 060401(R) (2008).

-
- ¹⁶³ V. D. Nguyen, L. Vila, P. Laczkowski, A. Marty, T. Faivre and J. P. Attané, *Phys. Rev. Lett.* **107**, 136605 (2011).
- ¹⁶⁴ R. Danneau, P. Warin, J. P. Attané, I. Petej, C. Beigné, C. Fermon, O. Klein, A. Marty, F. Ott, Y. Samson, and M. Viret, *Phys. Rev. Lett.* **88**, 157201 (2002).
- ¹⁶⁵ V. D. Nguyen, L. Vila, A. Marty, J. C. Pillet, L. Notin, C. Beigné, S. Pizzini, and J. P. Attané, *Appl. Phys. Lett.* **100**, 252403 (2012).
- ¹⁶⁶ M. Cormier, A. Mougou, J. Ferré, A. Thiaville, N. Charpentier, F. Piéchon, R. Weil, V. Baltz, and B. Rodmacq, *Phys. Rev. B* **81**, 024407 (2010).
- ¹⁶⁷ J. Curiale, A. Lemaître, C. Ulysse, G. Faini, and V. Jeudy, *Phys. Rev. Lett.* **108**, 076604 (2012).
- ¹⁶⁸ J.-P. Adam, N. Vernier, J. Ferré, A. Thiaville, V. Jeudy, A. Lemaître, L. Thevenard, and G. Faini *Phys. Rev. B* **80**, 193204 (2009).
- ¹⁶⁹ S. Emori, U. Bauer, S.-M. Ahn, E. Martinez, and G. S. D. Beach, *Nature Mater.* **12**, 611 (2013).
- ¹⁷⁰ K.-S. Ryu, L. Thomas, S.-H. Yang, and S. Parkin, *Nature nanotech.*, **8**, 527 (2013).
- ¹⁷¹ A. V. Khvalkovskiy, K. A. Zvezdin, Ya.V. Gorbunov, V. Cros, J. Grollier, A. Fert, and A. K. Zvezdin, *Phys. Rev. Lett.* **102**, 067206 (2009).
- ¹⁷² S.-G. Je, D.-H. Kim, S.-C. Yoo, B.-C. Min, K.-J. Lee and S.-B. Choe, *Phys. Rev. B* **88**, 1440 (2012).
- ¹⁷³ A. Hrabec, N. A. Porter, A. Wells, M. J. Benitez, G. Burnell, S. McVitie, D. McGrouther, T. A. Moore and C. H. Marrows, *Phys. Rev. B* **90**, 020402 (2014).
- ¹⁷⁴ A. Vansteenkiste, J. Leliaert, M. Dvornik, M. Helsen, F. Garcia-Sanchez, and B. V. Waeyenberge, *AIP Advances* **4**, 107133 (2014).
- ¹⁷⁵ M. S. Miao, A. Herwadkar, and W. R. L. Lambrecht, *Phys. Rev. B* **72**, 033204 (2005).
- ¹⁷⁶ S. Kokado, N. Fujima, K. Harigaya, H. Shimizu, and A. Sakuma, *Phys. Rev. B* **73**, 172410 (2006).
- ¹⁷⁷ J. Curiale, A. Lemaître, C. Ulysse, G. Faini, and V. Jeudy, *Phys. Rev. Lett.* **108**, 076604 (2012).
- ¹⁷⁸ Y.-C. Lau, and M. Hayashi, *Jpn. J. Appl. Phys.* **56**, 0802B5 (2017).
- ¹⁷⁹ K.-J. Kim, S. K. Kim, Y. Hirata, S.-H. Oh, T. Tono, D.-H. Kim, T. Okuno, W. S. Ham, S. Kim, G. Go, Y. Tserkovnyak, A. Tsukamoto, T. Moriyama, K.-J. Lee, and T. Ono, *Nature Mater.* **16**, 1187 (2017).
- ¹⁸⁰ A. Anzai, T. Gushi, T. Komori, S. Honda, S. Isogami, and T. Suemasu, *J. Appl. Phys.* **124**, 123905 (2018).
- ¹⁸¹ T. Komori, A. Anzai, T. Gushi, K. Toko, and T. Suemasu, *J. Cryst. Growth* **507**, 163 (2019).
- ¹⁸² Y. Hirata, D.-H. Kim, T. Okuno, T. Nishimura, D.-Y. Kim, Y. Futakawa, H. Yoshikawa, A. Tsukamoto, K.-J. Kim, S.-B. Choe, and T. Ono, *Phys. Rev. B* **97**, 220403(R) (2018).
- ¹⁸³ L. Chen, *J. Appl. Phys.* **100**, 113717 (2006).
- ¹⁸⁴ M. Meng, S. X. Wu, W. Q. Zhou, L. Z. Ren, Y. J. Wang, G. L. Wang, and S. W. Li, *J. Appl. Phys.* **118**, 053911 (2015).
- ¹⁸⁵ M. Mekata, *J. Phys. Sci. Jpn.* **17**, 796 (1962).
- ¹⁸⁶ J. C. Slater, *Phys. Rev.* **49**, 931 (1936).
- ¹⁸⁷ L. Pauling, *Phys. Rev.* **54**, 899 (1938).
- ¹⁸⁸ F. Takata, K. Ito, Y. Takeda, Y. Saitoh, K. Takashi, A. Kimura, and T. Suemasu, *Physical Review Materials*

2, 024407 (2018).

- ¹⁸⁹ K. Ito, Y. Yasutomi, S. Zhu, M. Nurmatamat, M. Tahara, Y. Takeda, Y. Saitoh, K. Toko, R. Akiyama, T. Oguchi, A. Kimura, and T. Suemasu, in preparation.
- ¹⁹⁰ Y.-C. Lau and M. Hayashi, *Jpn. J. Appl. Phys.* **56**, 0802B5 (2017).
- ¹⁹¹ G. Zahnd, L. Vila, T. V. Pham, A. Marty, P. Laczkowski, W. Savero Torres, C. Beigné, C. Vergnaud, M. Jamet, and J.-P. Attané, *Nanotechnology* **27**, 035201 (2015).
- ¹⁹² M. Hayashi, J. Ieda, Y. Yamane, J. Ohe, Y. K. Takahashi, S. Mitani and S. Maekawa, *Phys. Rev. Lett.* **108**, 147202 (2012).
- ¹⁹³ T. Nozaki, Y. Shiota, M. Shiraishi, T. Shinjo, and Y. Suzuki, *Appl. Phys. Lett.* **96**, 022506 (2010).
- ¹⁹⁴ Y. Shiota, T. Maruyama, T. Nozaki, T. Shinjo, M. Shiraishi, and Y. Suzuki, *Appl. Phys. Express* **2**, 063001 (2009).
- ¹⁹⁵ M. Endo, S. Kanai, S. Ikeda, F. Matsukura, and H. Ohno, *Appl. Phys. Lett.* **96**, 212503 (2010).
- ¹⁹⁶ Y. Shiota, F. Bonell, S. Miwa, N. Mizuochi, T. Shinjo, and Y. Suzuki, *Appl. Phys. Lett.* **103**, 082410 (2013).
- ¹⁹⁷ A. Okada, S. Kanai, M. Yamanouchi, S. Ikeda, F. Matsukura, and H. Ohno, *Appl. Phys. Lett.* **105**, 052415 (2014).
- ¹⁹⁸ K. Yamada, H. Kakizakai, K. Shimamura, M. Kawaguchi, S. Fukami, N. Ishiwata, D. Chiba, and T. Ono, *Appl. Phys. Express* **6**, 073004 (2013).
- ¹⁹⁹ U. Bauer, L. Yao, A. J. Tan, P. Agrawal, S. Emori, H. L. Tuller, S. van Dijken, and G. S. D. Beach, *Nat. Mater.* **14**, 174 (2015).
- ²⁰⁰ S. Nakazawa, A. Obinata, D. Chiba, and K. Ueno, *Appl. Phys. Lett.* **110**, 062406 (2017).